CZECH TECHNICAL UNIVERSITY IN PRAGUE

Faculty of Nuclear Sciences and Physical Engineering

Department of Physics

Bachelor thesis

Heavy quarkonia production at the STAR experiment

Jana Fodorová

Supervisor: RNDr. Petr Chaloupka, Ph.D.

Prague, 2014

ČESKÉ VYSOKÉ UČENÍ TECHNICKÉ
V PRAZE
Fakulta jaderná fyzikálně inženýrská
Katedra fyziky

Bakalářská práce

Produkce těžkých kvarkonií na experimentu STAR

Jana Fodorová

Supervisor: RNDr. Petr Chaloupka, Ph.D.

Praha, 2014

Prohlášení:

Prohlašuji, že jsem svou bakalářskou práci vypracovala samostatně a použila jsem pouze podklady (literaturu, projekty, software, atd.) uvedené v přiloženém seznamu.

Nemám závažný důvod proti užití tohoto školního díla ve smyslu 60 Zákona č.121/2000 Sb., o právu autorském, o právech souvisejících s právem autorským a o změně některých zákonů (autorský zákon).

V Praze dne

Title:
Heavy quarkonia production at the STAR experiment

Author: Jana Fodorová

Specialization: Experimental nuclear physics

Sort of project: Bachelor thesis

Supervisor: RNDr. Petr Chaloupka, Ph.D.

Abstract: Under normal conditions, basic building blocks of matter, quarks and gluons, are bound within hadrons. The theory of strong interaction predicts that under conditions of high energy density and high temperature the nuclear matter may undergo a phase transition into a novel state of matter called quark-gluon plasma. We expect that this state of matter was present in the earliest stages of the universe shortly after the Big Bang and that can be experimentally recreated in high energy heavy ion collisions. The STAR experiment at RHIC in BNL is one of the foremost experiments in the study of quark-gluon plasma. An important probe in the study of the medium created in collisions of heavy ions are heavy quarks (c and b). This thesis discusses physics of heavy quarks and deals in more detail with quarkonia − bound states of quarks and antiquarks. The models of heavy quarkonia production together with modifications of the production due to the presence of surrounding nuclear matter are discussed. The suppression of heavy quarkonia production in heavy ion collisions has been considered a prominent signature of a presence of the quark-gluon plasma. Part of this work is dedicated to other effects which can also influence the heavy quarkonia production, but do not come from quark-gluon plasma. These are called cold nuclear matter effects. In the last part of this thesis measurements of the STAR experiment on the heavy quarkonia production are discussed and compared with selected results from experiments at SPS and LHC colliders.

Key words: heavy flavor, quarkonia, quark-gluon plasma, STAR, RHIC, heavy ion collisions

Název práce:
Produkce těžkých kvarkonií na experimentu STAR

Autor: Jana Fodorová

Abstrakt: Za normálních okolností jsou základní stavební kameny hmoty, kvarky a gluony, vázané v hadronech. Teorie silné interakce však předpovídá, že za podmínek vysoké hustoty energie a teploty přechází jaderná hmota do stavu tzv. kvark-gluonového plazmatu. Domníváme se, že tento stav hmoty byl přítomen u zrodu vesmíru krátce po velkém třesku a že se může formovat také ve vysokoenergetických srážkách těžkých jader. Jeden z nejvýznamnějších experimentů pro studium kvark-gluonového plazmatu je experiment STAR na urychlovači RHIC v BNL. Významnou sondou při zkoumání média vznikajícího ve srážkách ultrarelativistických těžkých jader jsou těžké kvarky (c a b). Tato práce se zabývá fyzikou těžkých kvarků a podrobněji se věnuje jejich vázaným stavům − kvarkoniím. Práce popisuje modely jejich vzniku a také efekty, které má na jejich produkci přítomnost jaderné hmoty. Předpovězené potlačení produkce těžkých kvarkonií v jádro-jaderných srážkách je považováno za jeden z hlavních znaků přítomnosti kvark-gluonového plazmatu. Existují však i jiné efekty, které mohou modifikovat produkci těžkých kvarkonií. Ty jsou však spůsobeny přítomností pouze studené jaderné hmoty, nikoliv kvark-gluonového plazmatu. Část práce je věnována právě těmto efektům. V závěru práce jsou diskutovány výsledky měření experimentu STAR a porovnány s vybranými výsledky z experimentů na urychlovačích SPS a LHC.

Klíčová slova: těžké vůně, kvarkonia, kvark-gluonové plazma, STAR, RHIC, srážky těžkých jader

Acknowledgement

First, I would like to thank RNDr. Petr Chaloupka, Ph.D. for his support, patience, help and friendliness. I also want to thank my family, friends and loved ones, who were there when I needed them.

Contents

1 Introduction to Particle Physics **1**
- 1.1 Particles . . . 1
  - 1.1.1 Elementary Particles . . . 1
  - 1.1.2 Composite Particles . . . 3
- 1.2 Fundamental Interactions . . . 3
  - 1.2.1 Gravitational interaction . . . 3
  - 1.2.2 Electromagnetic interaction . . . 4
  - 1.2.3 Weak interaction . . . 4
  - 1.2.4 Strong interaction . . . 4
- 1.3 Quantum Chromodynamics . . . 4
  - 1.3.1 Color confinement . . . 5
  - 1.3.2 Asymptotic freedom . . . 5
- 1.4 Quark-gluon Plasma . . . 6

2 Nucleus-Nucleus Collisions **9**
- 2.1 Kinematic and dynamic variables of collision . . . 9
- 2.2 Collision Geometry . . . 11
- 2.3 Space-time Evolution of the Collision . . . 13
- 2.4 Probes of Quark-Gluon Plasma . . . 14
  - 2.4.1 High p_T and Nuclear Modification Factor . . . 14
  - 2.4.2 Elliptic Flow . . . 15
  - 2.4.3 Direct Photons . . . 15
  - 2.4.4 Dilepton Production . . . 16
  - 2.4.5 Strangeness Enhancement . . . 16
  - 2.4.6 Quarkonium Suppression . . . 16

3 The STAR Experiment **17**
- 3.1 The Relativistic Heavy Ion Collider . . . 17
- 3.2 The PHENIX experiment . . . 18
- 3.3 The STAR Detector . . . 18
  - 3.3.1 Time Projection Chamber . . . 19
  - 3.3.2 Time of Flight Detector . . . 22
  - 3.3.3 Barrel Electromagnetic Calorimeter . . . 23
  - 3.3.4 Inner tracking system . . . 25
  - 3.3.5 Silicon Strip Detector . . . 25

3.3.6 Muon Telescope Detector . . . 27
3.3.7 Triggering System . . . 29

4 Heavy Flavor Physics **33**
4.1 Motivation for heavy quarks . . . 33
4.1.1 Heavy Quark Energy Loss . . . 33
4.2 Heavy Flavor Production . . . 35
4.2.1 Total heavy quark cross section . . . 36
4.2.2 Heavy flavor measurements . . . 36

5 Heavy Quarkonia **41**
5.1 Quarkonia Families . . . 41
5.2 Models of Heavy Quarkonia (J/ψ) Production . . . 43
5.2.1 Color Singlet Model . . . 43
5.2.2 Color Octet Model and NRQCD . . . 43
5.2.3 Color Evaporation Model . . . 44
5.2.4 J/ψ polarization . . . 45
5.3 Quarkonia in Heavy Ion Collisions . . . 46
5.3.1 Quarkonia as a signal of QGP . . . 47
5.3.2 Other effects on quarkonia production . . . 49
5.4 Selected results of quarkonia measurements . . . 53
5.4.1 Production modification of J/ψ . . . 53
5.4.2 Quarkonia suppression in d+Au collisions . . . 59
5.4.3 J/ψ elliptic flow . . . 60
5.4.4 Υ suppression . . . 62
5.4.5 Quarkonia suppression as a function of binding energy . . . 64

List of Figures

1.1 Elementary particles. 2
1.2 The Q^2-dependence of the coupling constant of the strong and electromagnetic force. 5
1.3 The QGP phase diagram. 6

2.1 The dependence of the pseudorapidity η on the polar angle θ. 10
2.2 The schematic view of geometry of the collision. 11
2.3 Central and peripheral collision. 12
2.4 Participants and spectators. 12
2.5 Space-time evolution of the collision (with presence of QGP). 13
2.6 Schematic view of the overlapped region in non-central collision, reaction plane and coordinate system. 15

3.1 The Relativistic Heavy Ion Collider. 18
3.2 The PHENIX Experiment. 19
3.3 The STAR Experiment. 20
3.4 The Time Projection Chamber. 21
3.5 The anode pad plane of the read out system of the TPC. 22
3.6 The energy loss of charged particles measured with TPC and $1/\beta$ of charged particles measured with TPC and TOF. 23
3.7 Side view of a STAR BEMC module. 24
3.8 Schematic illustration of the STAR BEMC BSMD module. 25
3.9 The Silicon Strip Detector. 26
3.10 The Heavy Flavor Tracker. 26
3.11 MTD trays. 27
3.12 Multi-gap Resistive Plate Chamber of the MTD. 28
3.13 Multi-gap Resistive Plate Chamber − principle of operation. 29
3.14 Projection of the R_{AA} of different Υ states with the MTD and J/ψ signal from p+p collisions at 500 GeV. 29
3.15 Vertex Position Detector. 30
3.16 The Beam Beam Counter. 31

4.1 The energy loss of c and b quarks as a function of quark energy. 34
4.2 The lowest order diagram for $c\bar{c}$ production through gluon fusion and quark-antiquark annihilation. 35
4.3 Heavy flavor production cross sections. 37

4.4 D meson spectra and differential $c\bar{c}$ cross section. 38
4.5 D^0 R_{AA} as a function of p_T at STAR and at ALICE. 38
4.6 NPE R_{AA} and v_2 in Au+Au collisions at $\sqrt{s_{NN}} = 200$ GeV. 39

5.1 The charmonium family. 42
5.2 The bottomonium family. 42
5.3 The lowest order diagram for the J/ψ production through gluon fusion in CSM. 43
5.4 The lowest order diagram for the J/ψ production through gluon fusion in COM. 44
5.5 The lowest order diagram for the J/ψ production through gluon fusion in CEM. 44
5.6 J/ψ and Υ cross sections. 45
5.7 The polarization parameter λ_θ as a function of J/ψ p_T. 46
5.8 The dissociation temperature range for different quarkonium states. 48
5.9 J/ψ enhancement through statistical regeneration: J/ψ production probability as the function of energy density. 49
5.10 J/ψ R_{AA} as a function of p_T − comparison of different models assuming additional effects on production with data. 50
5.11 Different parametrizations of gluon nPDF modifications. 51
5.12 J/ψ yield in Au+Au collisions at $\sqrt{s_{NN}}$ = 200 GeV at STAR for different centralities. 54
5.13 J/ψ R_{AA} as a function of p_T in Au+Au collisions at $\sqrt{s_{NN}} = 200$ GeV at STAR for different centralities. 55
5.14 J/ψ R_{AA} as a function of N_{part} at STAR for different p_T regions and compared to CMS data. 56
5.15 J/ψ R_{AA} as a function of N_{part} for different energies at RHIC and compared to SPS data. 56
5.16 J/ψ R_{AA} as a function of $dN_{ch}/d\eta$ in Pb+Pb (ALICE) and Au+Au (STAR) collisions. 57
5.17 J/ψ R_{AA} as a function of rapidity y in Au+Au collisions at $\sqrt{s_{NN}} = 200$ GeV at PHENIX for two different centralities. 58
5.18 J/ψ R_{AA} as a function of p_T in Pb+Pb (ALICE) collisions compared to Au+Au (STAR) and Au+Au (PHENIX) collisions. 59
5.19 J/ψ and Υ R_{dAu} at STAR and at PHENIX. 60
5.20 J/ψ v_2 as a function of p_T in 0-80% central events in Au+Au collisions at STAR. 61
5.21 J/ψ v_2 as a function of p_T in Pb+Pb collisions at ALICE. 61
5.22 R_{AA} (R_{dAu}) as a function of N_{part} for Υ(1S+2S+3S) in d+Au and Au+Au collisions at STAR. 62
5.23 R_{AA} for Υ(1S+2S+3S) in U+U collisions as a function of N_{part} at STAR. . . . 63
5.24 R_{AA} for Υ(1S) and Υ(2S) in Pb+Pb collisions at CMS. 64
5.25 R_{AA} for for different quarkonium states as a function of binding energy at STAR and at CMS. 65

List of Tables

1.1 Fundamental interactions. Relative strength is given with respect to the strong interaction. 3

5.1 Basic properties of quarkonia. 41

Chapter 1

Introduction to Particle Physics

Technical developments in the 1950s enabled high-energy beams of particles to be produced in laboratories. Consequently, a wide range of controlled scattering experiments was performed. The greater use of computers and sophisticated methods of analysis led to the opportunity to handle huge quantities of data that were produced. Since then, various measurements resulted in the discovery of a large number of particles.

This chapter provides basic information on the current knowledge of particle physics. All the known particles can be divided into different groups according to several criteria. In this chapter, particles are divided into elementary and composite and some of their properties are mentioned. Emphasis is placed on elementary particles. The theory concerning all the known elementary particles is called The Standard Model of particle physics. Moreover, the Standard Model includes a theory of three of the fundamental interactions of nature - the strong, weak, and electromagnetic interaction. Gravitational interaction is not incorporated in the Standard model, however, in this chapter all the fundamental forces of nature as the forces acting among the particles are briefly presented.

1.1 Particles

Elementary particle is a particle with no evidence of its substructure. A composite particle is a name for a particle which consists of two or more elementary particles.

1.1.1 Elementary Particles

Elementary particles can be divided into two classes - according to the fact if they are fermions, i.e. particles characterized by Fermi-Dirac statistics and following the Pauli exclusion principle, or not. The first class includes fermionic particles - particles with half-integral spin, namely quarks and leptons, and the second one contains non-fermionic bosons with integer spin. A brief overview of elementary particles can be seen in the Figure 1.1.

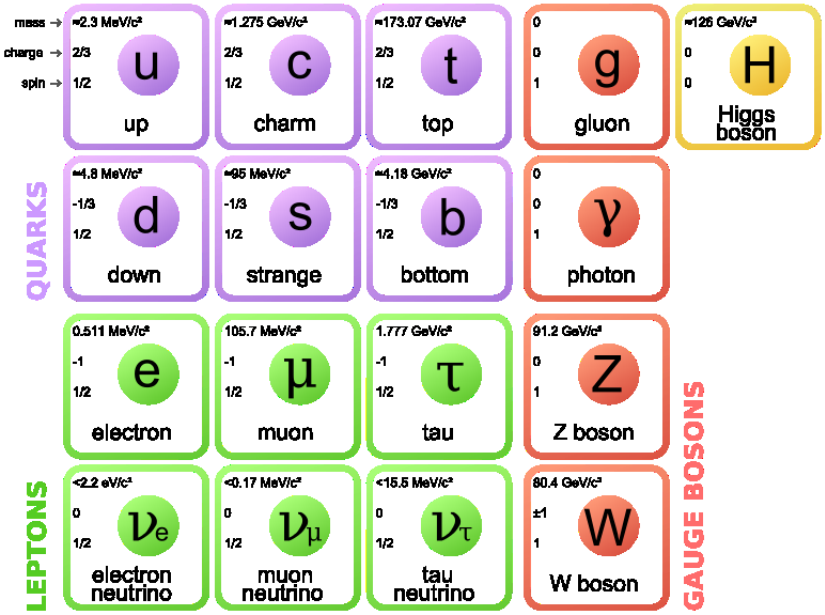

Figure 1.1: Elementary particles. Taken from [1].

Quarks and Leptons

Quarks and leptons are fermions with spin 1/2. They are characterized by a quantum number called flavor. Quarks and leptons with 6 different flavors are known to exist. They are divided into doublets and form three generations of elementary particles. The first generation is formed by the doublet of up (u) and down (d) quark and the lepton doublet of electron (e) and electron neutrino (ν_e). The doublet of charm(c) and strange (s) quark with the lepton doublet of muon (μ) and muon neutrino (ν_μ) form the second generation, the third generation of elementary particles is formed with the top (t) and bottom (b) quark doublet and the tau (τ) and tau neutrino (ν_τ) lepton doublet.

Each quark carries one of the three different colors – red, green, blue – in analogy to the three primary colors. Similarly to the interaction between electric charges, the colors of the interacting quarks influence the interaction between quarks.

The electron, the muon and the tau carry an electric charge of -1, while the three neutrinos do not carry any electric charge.

In addition to this classification, each of the mentioned particles has its antiparticle with the same mass and opposite charge.

Gauge Bosons

All the gauge bosons have spin 1. Accordingly, they do not obey the Pauli exclusion principle. They are mediators of the interactions and they can be massless like photons and gluons or massive like W^+, W^-, Z^0 bosons. Photons are associated with the electromagnetic interaction,they are electrically neutral. Electrically charged W^+ and W^- together with electrically

neutral Z^0 boson are associated with the weak interaction. The term gluons denotes eight gauge bosons which are electrically neutral. As the mediators of the strong interaction they carry the color quantum number.

Higgs Boson

In the Standard Model, the Higgs boson is a particle with spin 0, no electric charge or color charge. It is postulated to explain the origin of mass within the theory, since without it all the particles in the model are predicted to have zero mass. In 2012 the experiments ATLAS and CMS at LHC in CERN observed a new "Higgs-like" particle with mass around 126 GeV [2]. To determine whether or not it is the Higgs boson further measurements are needed. Recent results [3, 4] indicate that the new particle is indeed the Higgs boson.

1.1.2 Composite Particles

A composite particle is a particle which consists of two or more elementary particles. The composite particle which is made of quarks held together by the strong force is called a hadron. Hadrons can be divided into two groups - mesons and baryons. Mesons are bound states of quark, while baryons are three-quark bound states. Familiar examples of the baryons are nucleons −the neutron (udd) and proton (uud), and of the mesons are pions − $\pi^+(u\bar{d}), \pi^-(d\bar{u}), \pi^0(u\bar{u} + d\bar{d} + s\bar{s})$.

1.2 Fundamental Interactions

There are four basic forces of nature - gravitational, electromagnetic, weak and strong. Some of the most important characteristics of the fundamental forces can be viewed in the Table 1.1.

Interaction	Mediator	Relative strength	Range [m]
Gravitational	graviton	10^{-39}	∞
Electromagnetic	photon	10^{-7}	∞
Weak	W and Z bosons	10^{-12}	10^{-18}
Strong	gluon	1	10^{-15}

Table 1.1: Fundamental interactions. Relative strength is given with respect to the strong interaction.

1.2.1 Gravitational interaction

Unlike the others, the weakest of the interactions, gravitation is not incorporated in the Standard Model. Gravitation is the only interaction that acts on all particles having mass. It is generally assumed that gravitation is mediated by a massless spin-2 particle called a graviton which has not been discovered yet.

1.2.2 Electromagnetic interaction

The electromagnetic interaction affects all charged particles It binds electrons into orbitals around nuclei to form atoms. In classical physics, the electromagnetic interaction is mediated by the electromagnetic waves, which are continuously emitted and absorbed. This effective idea is applicable at long distances, at short distances ($\sim 10^{-14}$ m) the quantum nature of the interaction must be taken into account and the interaction is mediated by the exchange of photons. Since photons have zero mass, the range of this force is infinite.

1.2.3 Weak interaction

The weak interaction is associated with the exchange of W^+, W^- and Z bosons. It affects quarks and leptons and can change the flavor of quarks. The weak interaction is the only interaction in which neutrions participate. Since the intermediators of this interaction are very massive, the range of this force is very short. The weak interaction is responsible for the β decay of nuclei.

1.2.4 Strong interaction

The strong interaction binds quarks into hadrons but it is observable also on a larger scale − it binds protons and neutrons to form nucleus. The range of this force corresponds with the size of the nucleus. Although the mediators of the strong interaction are 8 gluons which are massless − so as photons are, the character of the strong interaction is different from the electromagnetic interaction. The difference between these two interactions and the most important features of the strong interaction are briefly explained in the following section, which focuses on the theory describing strong interaction called Quantum Chromodynamics.

1.3 Quantum Chromodynamics

A theory describing strong interaction is called Quantum Chromodynamics (QCD). By analogy with Quantum Electrodynamics (QED) which describes the electromagnetic interaction and in which the electric charge plays a key role, for QCD the color charge is important. All the fundametal particles of strong interaction, i.e. quarks and gluons, carry the color charge. Quarks carry one of three color charges − red, green or blue (or one of their anticolors) while gluons can exist in eight colour states. The crucial difference between QCD and QED is as follows − photon, the mediator of electromagnetic interaction does not carry any electric charge thus photons do not interact with each other. On the other hand, gluons as the mediators of strong interaction carry the color charge and so they can interact with other gluons. The coupling constant of the strong interaction α_s which determines the strength of the interaction shows the different dependence on the transferred energy (and thus on the distance) compared to the coupling constant of the electromagnetic force α. This is illustrated in the left panel of Figure 1.2.The properties mentioned above lead to characteristics of the QCD − color confinement and asymptotic freedom.

1.3.1 Color confinement

The QCD potential V between a quark and an antiquark as a function of the distance r can be expressed by the effective formula (called Cornell potential)[5]

$$V(r) = -\frac{a}{r} + kr, \tag{1.1}$$

where constant k determines long distance properties of the potential. Hence, the QCD potential consists of two terms − Coulomb term and "elastic" term. With increasing the distance r the Coulomb term vanishes but the attractive force (given by the elastic term) between quark and antiquark increases. Intuitively, the connection between quark and antiquark can be described by an elastic string or color flux tube. Moreover, when the QCD potential exceeds two quark masses it is expected that the string breaks and a new quark-antiquark pair is created from vacuum. Accordingly, (at longer distances or lower energies) it is not possible to observe a free quark − all quarks are bound within hadrons. This characteristic feature of the QCD is called color confinement.

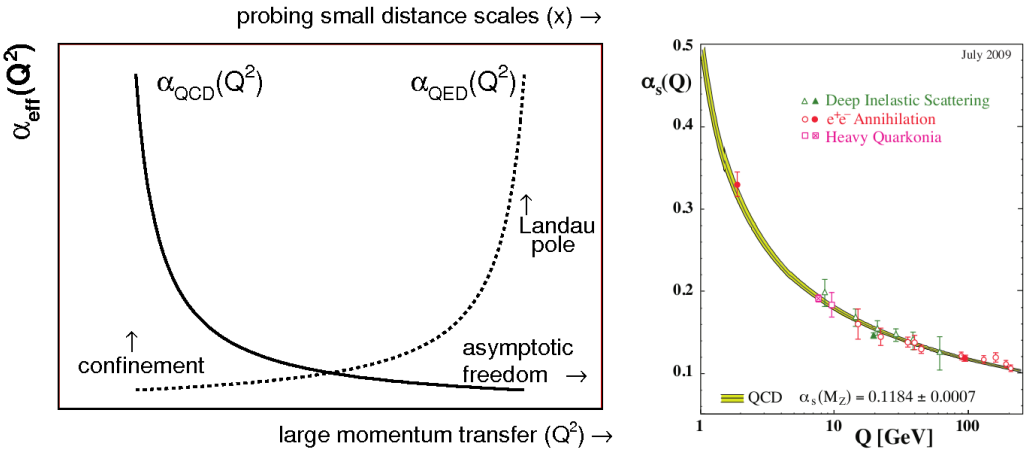

Figure 1.2: Left: The different Q^2-dependence of the coupling constant of the strong and electromagnetic force [6]. Right: The Q-dependence of α_s from experiments and theoretical predictions [7].

1.3.2 Asymptotic freedom

The QCD coupling constant α_s , which describes the strength of the strong interaction, depends on the momentum Q^2 transferred in the interaction. Since [8]

$$\alpha_s \sim \frac{1}{ln\left(\frac{Q^2}{\Lambda^2}\right)}, \tag{1.2}$$

where Λ is a constant defining the scale, α_s decreases logarithmically with increasing Q^2. The exact Q dependence of α_S, supported by experiments, can be seen in the right panel of the Figure 1.2. Since the distance is the variable inverse to Q^2 the QCD coupling constant α_s increases with the distance. At very short distances, respectively at high Q^2 α_s tends to zero. This feature of QCD is called "asymptotic freedom" [9]. In principle the asymptotic freedom means that under the above conditions quarks and gluons behave as almost free particles. The phase of matter consisting of asymptotically free quarks and gluons, where quarks and gluons are deconfined from bound states of hadrons, is called quark-gluon plasma.

1.4 Quark-gluon Plasma

The QCD assumes that under the conditions of high temperature and/or high energy density a phase transition of hadronic matter into quark-gluon plasma occurs [10].

Figure 1.3 shows the QGP phase diagram for nuclear matter. The vertical axis represents temperature and the horizontal axis represents baryon chemical potential. The baryon chemical potential has similar meaning to net baryon density.

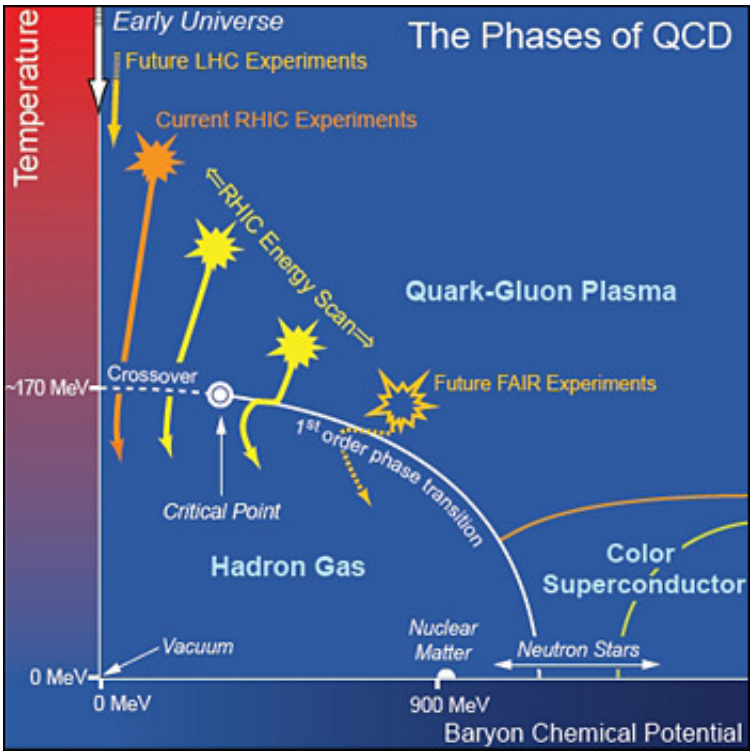

Figure 1.3: The QGP phase diagram [11].

At lower temperatures and lower baryochemical potentials the matter is in the form of a hadron gas. The transition to the QGP phase is reached by increasing the temperature or the

baryon chemical potential. Current knowledge suggests that the type of trasition depends on how new phase is reached. In the Figure 1.4 one point, called critical point, is of particular importance. The white solid curve starting from this point represents the first order phase transition of the hadronic matter to QGP. On the left from the critical point the crossover region starts. It is expected that in this region the hadronic matter transforms into QGP continuously without the phase transition (respectively with the phase transition of the second order).

At zero temperature and high baryon densities the medium is in high-energy deconfined phase predicted to exist in neutron stars. On the other hand, the system at zero baryon chemical potential and high temperatures is expected to exist at the birth of universe a few milliseconds after big bang (approximately 13.8 billion years ago).

The character of the phase transition, especially in the region close to the critical point is still not explored in detail. Therefore, there are several experiments dedicated for this study. The most relevant for this work is the STAR Beam Energy Scan I. and the planned Beam Energy Scan II.[12].

Chapter 2

Nucleus-Nucleus Collisions

Since it is expected that the transition to the quark-gluon plasma can be reached in high energy heavy ion collisions, these are engaged for testing the predicted signatures of the QGP and for understanding the QCD in the fields where it is not calculable.

In this chapter basic information about the nucleus-nucleus collisions are presented. First of all, the kinematic and dynamic variables of collision are defined. Geometry of the collision and space-time evolution of the collision are described. The last section of this chapter is dedicated to the observables and probes of the quark-gluon plasma as a phase of nuclear matter in the evolution of the collision.

2.1 Kinematic and dynamic variables of collision

It is useful to define basic observables which describe collision. Since high velocities, i.e. velocities close to the speed of light, are typical for colliding and newly created particles it is most preferred to use such variables which have simple properties under a Lorentz transformation. In following text the notation of natural units is used where the speed of light is set to 1, i.e. $c = 1$.

Let $P = (E, p_x, p_y, p_z)$ be the four-momentum of the particle, where E is its energy, and $\vec{p} = (p_x, p_y, p_z)$ is its momentum (p_z is the z-component of the momentum, i.e. the component parallel to the beam pipe, p_x and p_y denote the momentum component perpendicular to the beam axis). Than, the longitudinal momentum $p_{||}$ can be defined as

$$p_{||} = p_z \tag{2.1}$$

and the transverse momentum is defined as

$$p_T = \sqrt{{p_x}^2 + {p_y}^2}. \tag{2.2}$$

In accordance with the previous definition, the transverse mass of the particle can be written as

$$m_T = \sqrt{m^2 + {p_T}^2}, \tag{2.3}$$

where m is the mass of the particle. The transverse mass is invariant under Lorentz transformation along the beam axis.

Another useful variable which describes kinematic properties of the particle is rapidity. It is defined as

$$y = \frac{1}{2} ln \left(\frac{E + p_{||}}{E - p_{||}} \right). \tag{2.4}$$

The rapidity is not Lorentz invariant, however, it is an additive variable (the transformed rapidity differs from the rapidity in the original frame only by a constant rapidity of the moving frame). It can carry value from $-\infty$ to ∞. In non-relativistic limit the rapidity corresponds to the velocity of the particle.

To determine the rapidity, it is necessary to know two quantities of the particle − its energy and its longitudinal momentum. To know the energy, the mass of the particle is needed, and hence, we need to identify the particle. In practice, to remove the mass-dependence of the rapidity, a variable pseudorapidity η is used. In terms of momentum, it can be written as [13]

$$\eta = \frac{1}{2} ln \left(\frac{p + p_{||}}{p - p_{||}} \right), \tag{2.5}$$

where $p = |\vec{p}|$. In the limit $m/p \to 0$ pseudorapidity tends to rapidity. The pseudorapidity can be also expressed through the angle θ between the momentum vector of the particle and the beam axis. Than

$$\eta = -ln \left[tan \left(\frac{\theta}{2} \right) \right], \tag{2.6}$$

where θ is also called the polar angle. The Figure 2.1 shows the η-dependence on the polar angle.

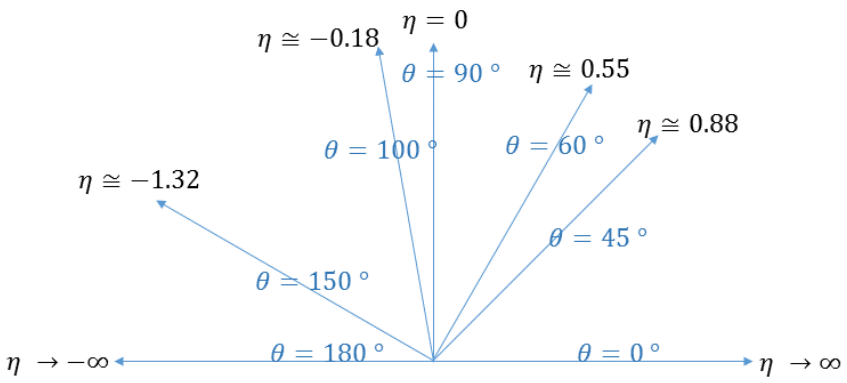

Figure 2.1: The dependence of the pseudorapidity η on the polar angle θ.

In summary, collider experiments measure momenta of particles in terms of transverse momentum p_T, pseudorapidy η and azimuthal angle Φ, which is defined as the angle between

the x-axis and the projection of the momentum in the xy-plane. The following conversion relations are often used [13]:

$$\begin{aligned} p_x &= p_T cos\Phi, \\ p_y &= p_T sin\Phi, \\ p_z &= p_T sinh\eta. \end{aligned} \tag{2.7}$$

Some of the above mentioned variables are illustrated in the Figure 2.2.

Another important variables in the high energy heavy ion collisions are the center of mass energy $\sqrt{s}$ and center of mass energy per nucleon-nucleon pair $\sqrt{s_{NN}}$. In case of two colliding nuclei with energies E_1, E_2 and momenta p_1, p_2, the center of mass energy is

$$\sqrt{s} = \sqrt{(E_1 + E_2)^2 - (p_1 + p_2)^2}. \tag{2.8}$$

For symmetric collision the relation between $\sqrt{s}$ and $\sqrt{s_{NN}}$ can be written as

$$\sqrt{s_{NN}} = \frac{\sqrt{s}}{A}, \tag{2.9}$$

where A is the number of nucleons in each colliding nuclei.

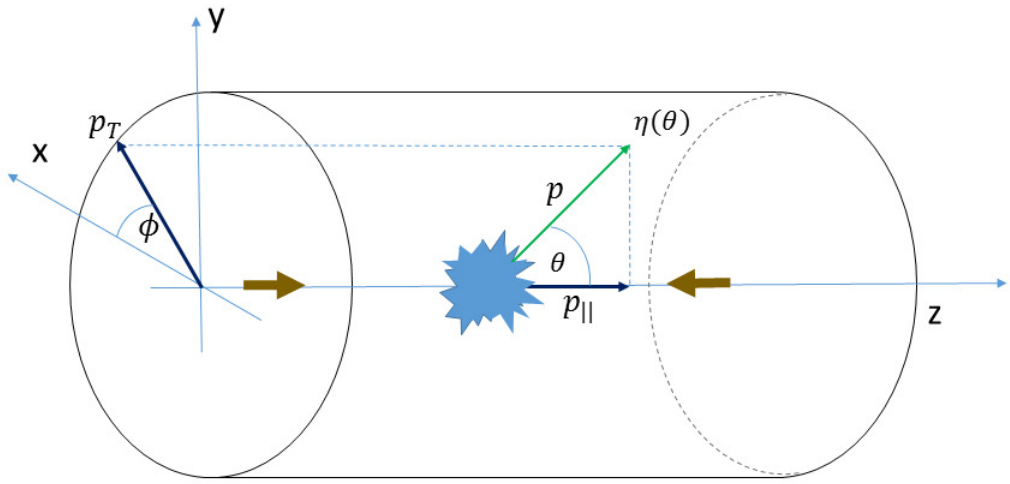

Figure 2.2: The schematic view of geometry of the collision. Brown arrows denote colliding particle, green arrow refers to the particle emerging from the collision.

2.2 Collision Geometry

In high energy collisions, colliding nuclei are Lorentz-contracted parallel to the direction of their motion by the factor $\gamma \geq 1$. Therefore, the shape of the nuclei in the laboratory frame is

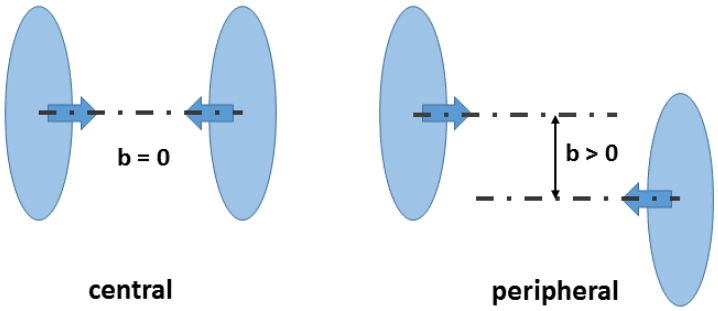

Figure 2.3: The central and peripheral collision.

not spherical but rather flattened. For example, at RHIC for $\sqrt{s_{NN}} = 200$ GeV $\gamma \simeq 100$ which is significant contraction. In collision of two nuclei, the impact parameter b which is defined as the perpendicular distance between the centers of the nuclei, can carry values in the range from 0 to $R_1 + R_2$ where R_1 and R_2 are the radii of the nuclei [14]. According to the values of b, the collisions can be divided into central ($b \simeq 0$), peripheral ($0 < b < R_1 + R_2$), respectively ultra-peripheral (in this case $b \geq R_1 + R_2$). The schematic drawing of central and peripheral collision for $R_1 = R_2$ can be seen in the Figure 2.3. Nucleons located in the overlap region participate in the interaction, so they are called participants. The non-interacting nucleons are called spectators. Participants and spectators are illustrated in the Figure 2.4.

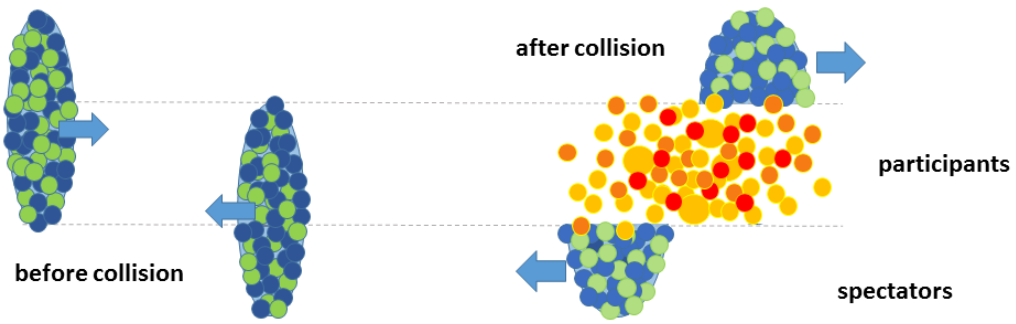

Figure 2.4: Participant and spectators of the collision of two nuclei.

2.3 Space-time Evolution of the Collision

The collision of high energy heavy ion nuclei is accompanied by different stages of evolution. Even in the present selected phases are not completely understood. One of the possible phases which could be a part of the collisional evolution of the system and is of the main interest to us, is the quark-gluon plasma.

Figure 2.5 shows the space-time evolution of the colliding nuclei in the case when the quark-gluon plasma phase occurs. The vertical axis represents the time direction and the horizontal axis shows the spatial direction. Two Lorentz-contracted heavy nuclei move along the light-cone until they collide in the point $(z,t) = (0,0)$. Than, the system goes through various states. These are described depending on the proper time of the system $\tau = \sqrt{t^2 - z^2}$.

Immediately after the collision the system is in the pre-equilibrium phase. This phase is still under theoretical investigation and is difficult to understand. As the nuclei traverse each other they create a fireball. In pre-equilibrium phase partons (quarks and gluons) are created in inelastic collisions and interact with each other. It is expected that hard interactions (i.e.interactions with high transferred momentum) present in this stage are responsible for the production of heavy quarks.

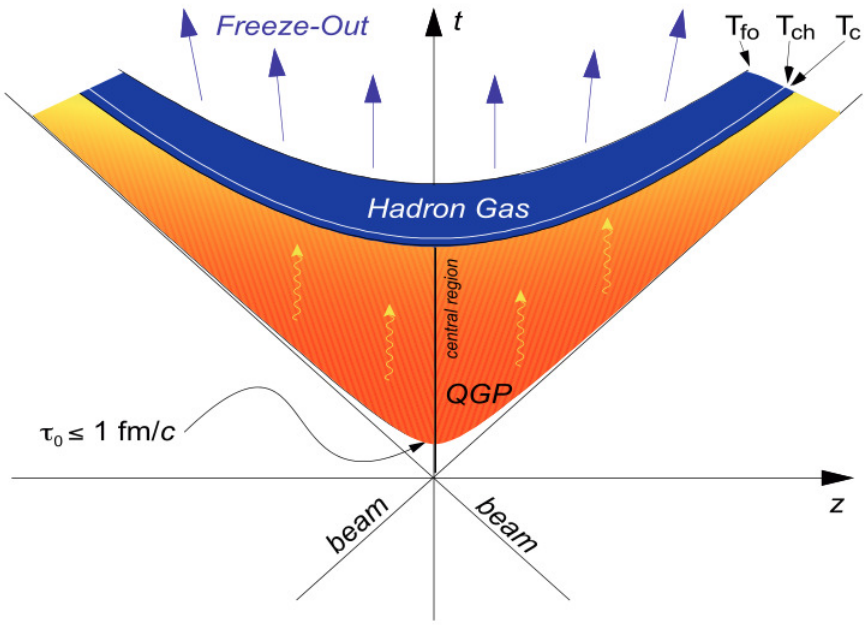

Figure 2.5: Space-time evolution of the collision (with presence of QGP) [14].

At $\tau_0 \simeq 0.1 - 1$ fm/c [15] the system reaches the thermal equilibrium. It is expected that from this moment suitable conditions for the quark-gluon plasma exist. Such system can be described by the laws of hydrodynamics, it expands (due to the high pressure) and cools down until the critical temperature T_c is reached. This happens at time $\tau_c \simeq 5$ fm/c [16]. The system is no longer in the quark-gluon plasma phase but it enters to the mixed phase. Partons start

to create hadrons, the system still expands and cools down. It stays in the mixed phase until it has totally changed to a hadron gas. It is not clear for how long the system is in the mixed phase (or if any mixed phase in the evolution occurs) [15].

Than, the system is in a hadron gas until it reaches chemical freeze-out T_{ch}. The system expands, the inelastic interactions disappear and at $\tau_{ch} \simeq 10$ fm/c [16] at which inelastic scattering stops and the particle identities are set until they decay [15]. After the chemical freeze-out particles can still interact elastically. With further expansion hadrons stop interact elastically. The time, when elastic scattering stops, $\tau_{fo} \simeq 20$ fm/c[16], is called thermal freeze-out T_{fo}. After that particles just move away from each other and leave the region of collision.

Since the state of quark-gluon plasma is very short-lived it can not be observed directly. To understand the QGP phase, it is necessary to understand all phases of the collisional evolution. Following section focuses on the observables and probes which could confirm the existence of the quark-gluon plasma and determine its properties.

2.4 Probes of Quark-Gluon Plasma

As argued before, in the evolution of the high energy heavy ion collision the matter may get into the quark-gluon plasma phase. Particles arising from the interaction carry information about the properties of quark-gluon plasma. Because there is no unique signal that enables to identify the quark-gluon plasma phase positively, the presence of the deconfined phase may be indicated indirectly. In this section, several observables and probes used to search for the quark-gluon plasma are mentioned.

2.4.1 High p_T and Nuclear Modification Factor

It is expected that high transverse momenta ($p_T > 2 - 3$GeV) particles come from hard processes occurring in the initial stage of the collision. For these processes large momentum transfers are typical and, therefore, they are associated with a small coupling constant QCD. For them, techniques of perturbative QCD are applicable. There are also soft processes associated with low p_T particles. Such processes occur during all stages of collision and belong to domain of nonperturbative QCD [13].

With no medium effects (p+p collisions), the yield of high p_T particles produced in heavy ion collisions should scale with the number of elementary binary collisions. However, medium produced in collisions can modify this scaling. Nuclear modification factor R_{AB} is considered to be a useful observable which can measure this scaling. It can be defined as [14]

$$R_{AB}\left(y, p_T\right) = \frac{1}{< T_{AB}(b) >} \frac{d^2 N_{AB}/dp_T dy}{d^2 N_{pp}/dp_T dy}. \tag{2.10}$$

It is the ratio of number of particles produced in A+B collisions to number of particles produced in p+p collisions scaled to the nuclear overlapping function $< T_{AB} >$, which is proportional to the average number of binary nucleon-nucleon collisions. For collisions of identical nuclei, $A = B$. If there are no effects of the medium, $R_{AB} = 1$, if $R_{AB} < 1$ it denotes the suppression effect and if $R_{AB} > 1$ it is enhancement of the particle production.

2.4.2 Elliptic Flow

Elliptic flow is a specific probe of the matter produced in early stages of heavy ion collisions. Unlike the central collisions, in which the colliding nuclei completely overlap, in non-central collisions the overlapped region has an almond shape,see left panel of Figure 2.6. The initial geometric anisotropy of strongly interacting results via multiple collisions in anisotropic pressure gradients and thus in anisotropic momentum distribution [17].

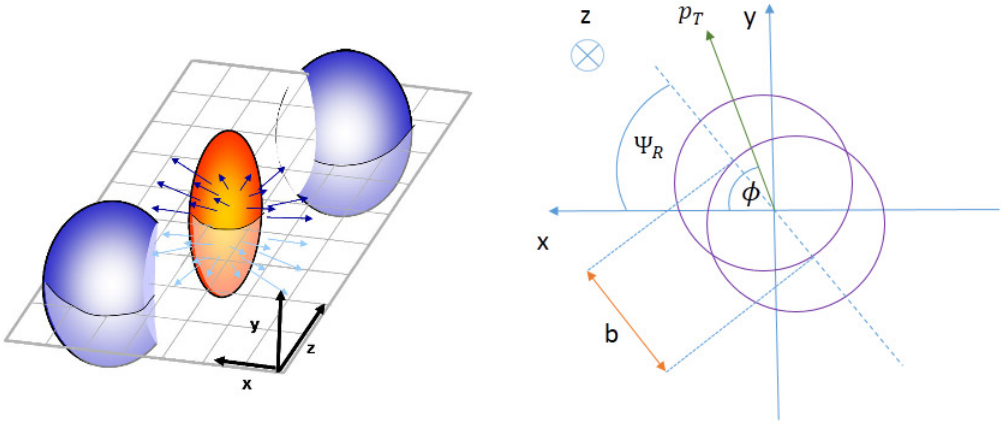

Figure 2.6: Left: The schematic view of the overlapped region in non-central collision [18]. Right: Reaction plane and coordinate system.

Elliptic flow is given by the second coefficient v_2 of the Fourier expansion describing the final state particle azimuthal distribution with respect to the reaction plane [8]

$$E\frac{d^3N}{d^3p} = \frac{d^2N}{2\pi p_T dp_T dy}\left(1 + \sum_{n=1}^{\infty} 2v_n\left(p_T, y\right) cos\left[n\left(\phi - \psi_r\right)\right]\right), \tag{2.11}$$

where ϕ is the azimuthal angle and ψ_r is the reaction plane angle. For better illustration, right panel of Figure 2.6 shows the coordinate system and reaction plane. In general, coefficients v_n can be calculated as average values [8]

$$v_n\left(p_T, y\right) = \langle cos\left[n\left(\phi - \psi_r\right)\right]\rangle. \tag{2.12}$$

2.4.3 Direct Photons

Direct photons are photons which do not come from decays of final state hadrons but from interactions of various charged particles in different stages of collision. They are considered to be excellent probes of the quark-gluon plasma phase − they interact only through electromagnetic interaction and therefore, their mean free path is much longer than the size of strongly interacting region.They are not affected by the thermalization. Thus, on their path, they do not lose the information about the medium [13, 8].

Direct photons can be divided into two groups: thermal and prompt. Thermal photons can come from quark-gluon plasma or from hadronic gas. They dominate in the low p_T region. Prompt photons are believed to come from hard processes in the initial state and dominate in the high p_T region. Direct photons are extremely difficult to observe. Their contribution to the total yield is only a few per cent. Direct photon measurements are complicated by a fact that a large background of photons comes from final state hadron decays [8].

2.4.4 Dilepton Production

In the quark-gluon plasma, a quark can interact with an antiquark to form the virtual photon which decays into lepton and its antiparticle. The name dilepton denotes the system of the produced lepton-antilepton pair. In order to be observed, the lepton and the antilepton must pass through the collision region and reach the detectors. The leptons interact with other particles only through the electromagnetic force. The free path of leptons is expected to be quite large (they do not interact strongly) and the leptons are not likely to suffer further collisions after they are produced. By extracting the dilepton spectrum coming from the quark-gluon plasma, it may be possible to determine the plasma initial temperature [13]. To do this, it is necessary to separate out other sources of dileptons. Such sources could be dileptons coming from decays of heavy flavor hadrons.

2.4.5 Strangeness Enhancement

The production of the strange quarks in the collisions without quark-gluon plasma phase transition is suppressed due to the large mass of s quark compared with u and d quark. In heavy ion collisions (with the QGP) there are more available channels for $s\bar{s}$ pairs production in the QGP, due to high gluon density, gluon fusion, annihilation of light quarks. Therefore, the strangeness production could be enhanced compared with p+p collisions.

2.4.6 Quarkonium Suppression

In the phase of quark-gluon plasma, heavy quarkonia (bound $c\bar{c}$ or $b\bar{b}$ pairs) may become unbound due to Debye screening. This should lead to a suppression of measured charmonium yields compared to the case when there is no quark-gluon plasma. Since the topic of this thesis is dedicated also to study of quarkonia, quarkonium suppression is described in more detail in Chapter 5.

Chapter 3

The STAR Experiment

In this chapter, the Relativistic Heavy Ion Collider and especially one of its experiments, the STAR experiment, are presented.

3.1 The Relativistic Heavy Ion Collider

In 2000, the Relativistic Heavy Ion Collider (RHIC) began its operation at the Brookhaven National Laboratory (BNL) in New York, USA. Until 2010, when the Large Hadron Collider (LHC) at the European Organization for Nuclear Research (known as CERN) started its program, it was the highest energy accelerator of heavy nuclei in the world.

The research at RHIC focuses on the study of QCD under extreme conditions and, especially, on the properties of QGP. It is worth mentioning that RHIC is the world's only device which is capable to collide high-energy beams of polarized protons.

RHIC consists of two independent, concentric storage acceleration rings of superconducting magnets with a circumference of ca. 3.8 km. Due to the independence of the rings RHIC has great flexibility to accelerate and collide beams of unequal masses, such as d+Au, Au+Au, Cu+Cu, Cu+Au and U+U at energies from $\sqrt{s_{NN}} = 7.7$ to 200 GeV for heavy ions and p+p at $\sqrt{s_{NN}} = 62.4$ to 510 GeV [20].

The complete layout of RHIC is illustrated in the Figure 3.1. Before reaching the storage rings particles pass through several devices. The travel of heavy ions begins in the Electron Ion Beam Source (EBIS). The heavy ion beams created and accelerated in EBIS go to the Booster Synchrotron, a circular accelerator, where, with each pass, they gain higher speeds. When heavy ion beams leave the Booster, they are traveling at about 37% the speed of light. Subsequently, the ions are carried to the Alternating Gradient Synchrotron (AGS) where they (are fully stripped of electrons and) get even more energy - until they reach 99.7% the speed of light. Then, at the end of the AGS-to-RHIC transfer line (AtR) bunches of ions are directed by a switching magnet either left to the clockwise RHIC ring or right to the counter-clockwise RHIC ring [21].

The experiments at RHIC which use colliding beams of polarized protons instead of heavy ions use a slightly different process of particle accelerating. For those experiments protons are first accelerated in the Linear Accelerator (Linac) and transferred to the Booster. From the Booster they travel to AGS and then to RHIC [21].

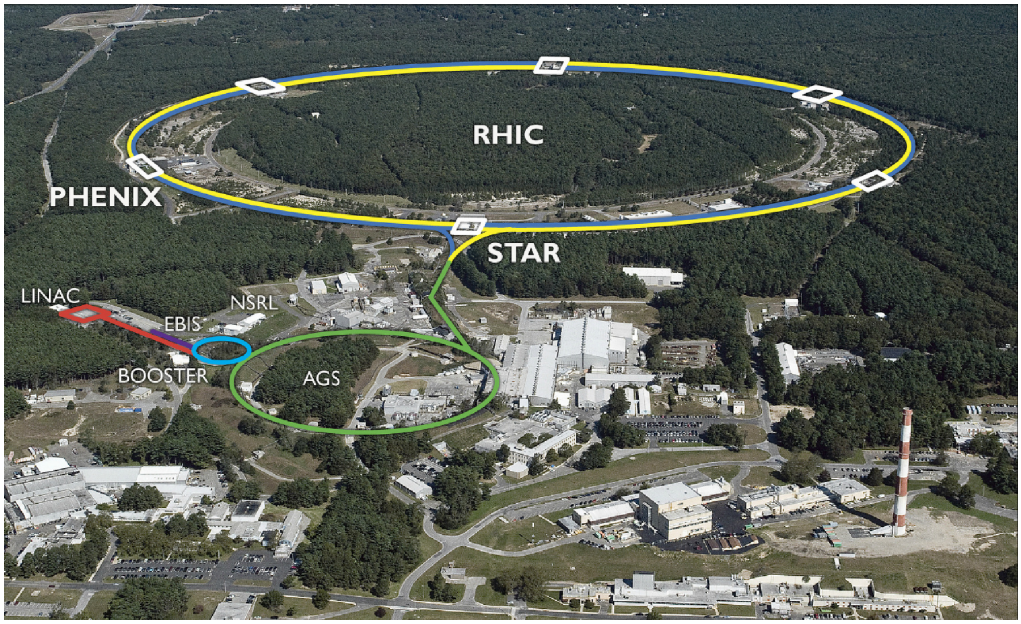

Figure 3.1: The Relativistic Heavy Ion Collider [19].

There are six intersection points at RHIC, where the two rings cross and particles can collide. Four of them are instrumented with experiments − BRAHMS, STAR, PHENIX and PHOBOS. At present, only two of them, STAR and PHENIX, are in operation.

3.2 The PHENIX experiment

The PHENIX detector (the Pioneering High Energy Nuclear Interaction eXperiment) focuses on the study of photons, leptons and muons, i.e. on the study of particles which are not affected by the strong interaction and, therefore, are direct probes of the collision, respectively of the QGP. The PHENIX experiment consists of various subdetectors which are divided into two central arms and two muon arms. The central arms focus on the measurement of pions, protons, kaons, deuterons, electrons, the muon arms focus on the measurement of muons. There are also event characterization detectors providing information about collision and a set of three huge magnets that curve trajectories of the charged particles[22]. The PHENIX experiment is schematically shown in the Figure 3.2.

3.3 The STAR Detector

The STAR (Solenoidal Tracker at RHIC) detector is used to investigate the behavior of strongly interacting matter at a high energy density and high temperature − to search for signatures of the QGP. It was designed mainly to reconstruct hadronic observables from the whole event. It excels in detection and identification of charged particles at mid-rapidity.

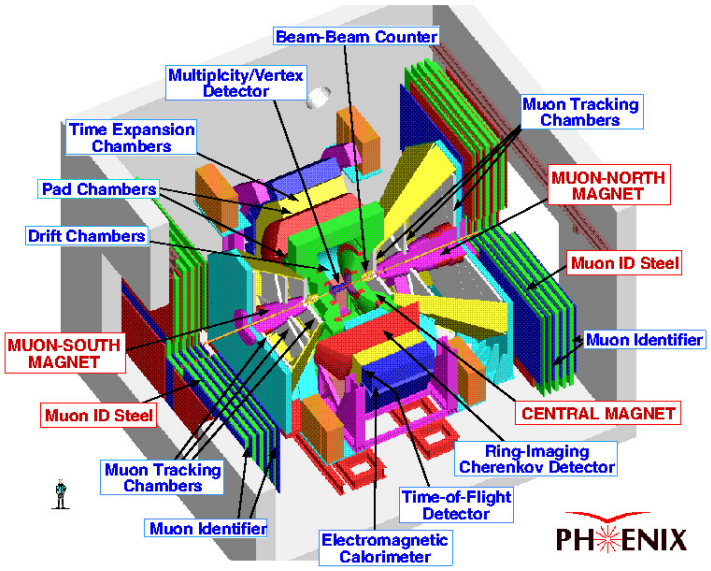

Figure 3.2: The PHENIX Experiment [23].

The STAR is cylindrical in shape and shares its central axis with the beam-line. It consists of various subsystems, illustrated in the Figure 3.3. The subsystems of the STAR detector can be divided into two groups − systems for tracking and particle identification, and event triggering detectors.

The most important detectors for tracking and particle identification described in this thesis are the Time Projection Chamber (TPC), the Time of Flight (TOF) detector and the Barrel Electromagnetic Calorimeter (BEMC). They sit in a solenoidal magnet which creates homogeneous magnetic field 0.5 T. The STAR detector is also equipped with the Inner Tracking System located inside the TPC. Special attention is paid to the Muon Telescope Detector (MTD) located behind the STAR magnet. Excluding the systems for tracking and particle identification, the Triggering System of the STAR Detector is presented.

3.3.1 Time Projection Chamber

The Time Projection Chamber is the main tracking device of the STAR detector and provides the particle identification. The acceptance of TPC covers pseudorapidity $|\eta| < 1.8$ and full azimuthal angle. The TPC is schematically shown in the Figure 3.4 [25].

The TPC is cylindrical in shape and has a length of 4.2 m. Its inner radius is 0.5 m and its outer radius is 2 m. A conductive cathode membrane (Cetral Membrane) held at the voltage -28 kV and grounded anode end caps generate, with combination of inner and outer field cage cylinders, a uniform electric field of ca. 135 V/cm in the gas volume of the TPC. The electric field is parallel to the beam line and also to the magnetic field 0.5 T generated by the solenoidal magnet, in which the TPC sits [25].

The anode end caps are equipped with the read-out system based on Multi-Wire Propor-

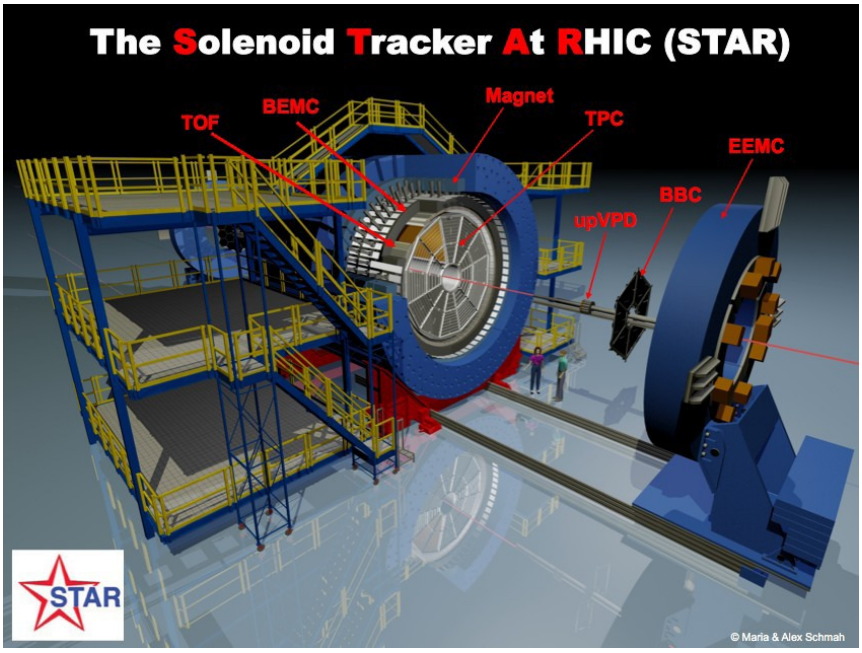

Figure 3.3: The STAR Experiment [24].

tional Chambers (MWPC). The end caps are divided into 12 sectors, each sector contains 13 inner and 32 outer pad rows. The inner pad rows are in the region of highest track density, therefore, for better resolution the pads are smaller. The outer pad rows have continuous pad coverage for optimal dE/dx measurements [16]. The schematic drawing of one pad plane can be seen in the Figure 3.5.

The P10 gas, which is the volume of the TPC filled with, is a mixture of Argon 90% and Methane 10%. When a charged particle traverses the gas volume of the TPC, it not only ionizes the molecules of the gas but also excites the atoms of Argon. Since the excitation energy of Argon is greater than the ionizing energy of Methane, in the collision of excited Ar atom with the CH_4 molecule the ionization of the CH_4 molecule can be caused. The probability of this process is very high because the time of life of the excited Ar is very long. Therefore, there is only a small fraction of the excited Ar atoms which return to the ground state by photon radiation. The energy which would be lost by radiation allows to create new free ions and electrons. Hence, the resolution of the detector is better [26]. The gas operates at 2 mbar above atmospheric pressure to prevent contamination by electronegative gas (O_2 , H_2O) which captures electrons [25].

The ions produced by traversing particles travel to the Central Membrane, while the ionization electrons drift to the anode end caps with a constant drift velocity. The (x,y) coordinates of the ionization clusters are determined by the charge measured by neighboring pads in the pad rows. Since the drift velocity is held constant, the z position of the clusters is determined by measuring the drift time of ionization electrons. Than, the 3D information about the track can be achieved [27].

The magnetic field curves the trajectory of the charged particles according to their momentum. This can be expressed as [27]

$$p_T = 0.3BR, \tag{3.1}$$

where p_T is the transverse momentum of the particle in GeV/c, B is the magnetic field in T and R is the radius of the curvature in m. Since particles lose their energy and momenta as they traverse the volume of the TPC, the measured momenta are corrected using expected energy loss values which are a function of velocity. A good approximation of energy loss for high momentum particles is obtained when the velocity is estimated using the muon mass. At low momentum, the muon mass assumption has to be corrected using simulation [27].

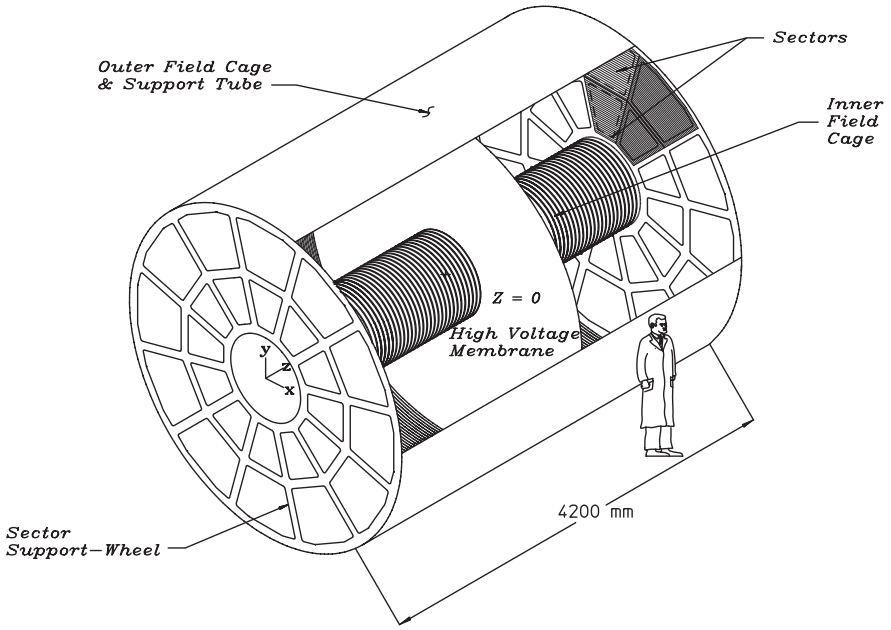

Figure 3.4: The Time Projection Chamber [25].

The ionization energy loss of particle per unit of length dE/dx is proportional to the measured charge, respectively amount of electrons, collected by the TPC pads rows. In principle, the ionization energy loss per unit of length can be expressed using the Bethe-Bloch formula [28]

$$-\frac{dE}{dx} = 4\pi N_A {r_e}^2 m_e c^2 z^2 \frac{Z}{A}\frac{1}{\beta^2}\left[\frac{1}{2} ln \frac{2m_e c^2 \beta^2 \gamma^2 T_{max}}{I^2} - \beta^2 - \frac{\delta}{2}\right], \tag{3.2}$$

where $\beta = v/c$ represents the velocity of the particle (v is the velocity, c is the speed of light), γ is the Lorentz factor, N_a is Avogadro's number, z is the charge of incident particle, Z

and A are atomic number and mass of absorber, r_e is classical electron radius, m_e is electron mass,I mean excitation energy, δ is density correction and T_{max} is the maximum kinetic energy which can be imparted to a free electron in a single collision. In practice, Bichsel functions, an extension of Bethe-Bloch formula, are used to determine dE/dx.

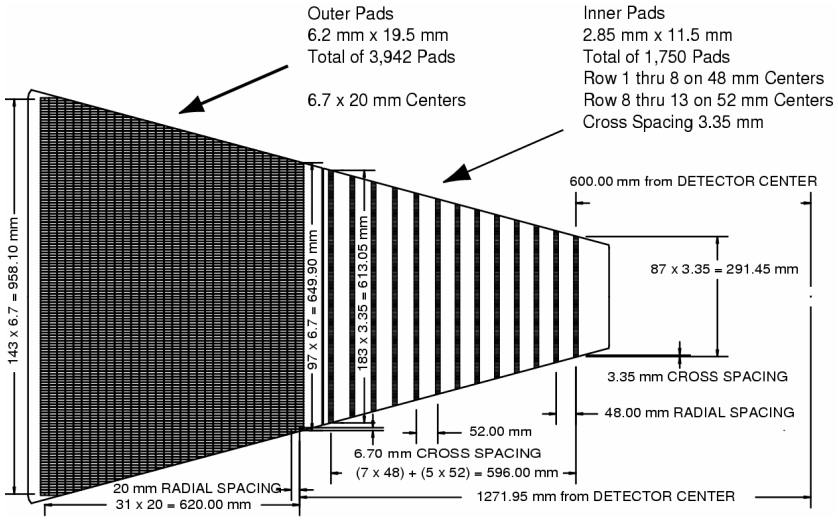

Figure 3.5: The anode pad plane of the read out system of the TPC [25].

Left panel of the Figure 3.6 shows the energy loss for charged particles in the TPC as a function of the particle momentum.

By the TPC alone, pions can be identified in the range of transverse momentum to 0.8 GeV/c and then in the range 3 GeV/$c \lesssim p_T \lesssim$10 GeV/c where the difference between energy loss of pions and kaons is ca. 15% and between pions and (anti)protons is even larger.

The particle identification capabilities of the TPC are less effective in the regions where the dE/dx of different particles overlaps. To improve this capability of the TPC at low and high momenta the detectors TOF and BEMC are used.

3.3.2 Time of Flight Detector

The Time of Flight (TOF) detector was installed to improve the particle identification capability of the STAR detector. It covers the pseudorapidity $|\eta| < 1$ and full azimuthal angle.

The TOF forms outer cylindrical shell of the TPC, as can be seen in the Figure 3.2, and consists of 120 trays. Each of the trays contains 32 Multi-gap Resistive Plate Chamber (MRPC) modules and each of the modules has 6 pads [31]. The MRPC design and technology of the similar modules is described in more detail in the section Muon Telescope Detector.

The TOF measures the time interval that particle spends traveling from one point to another. The "start time" t_0 is given by the two STAR Vertex Position Detectors (VPDs), described in more detail in section 3.3.7, which detect forward moving charged fragments from the collision. The "stop time" t_1 is determined as the time when the signal of a charged particle that passes through any of the pads of the TOF is detected. Then, the time-of-flight interval

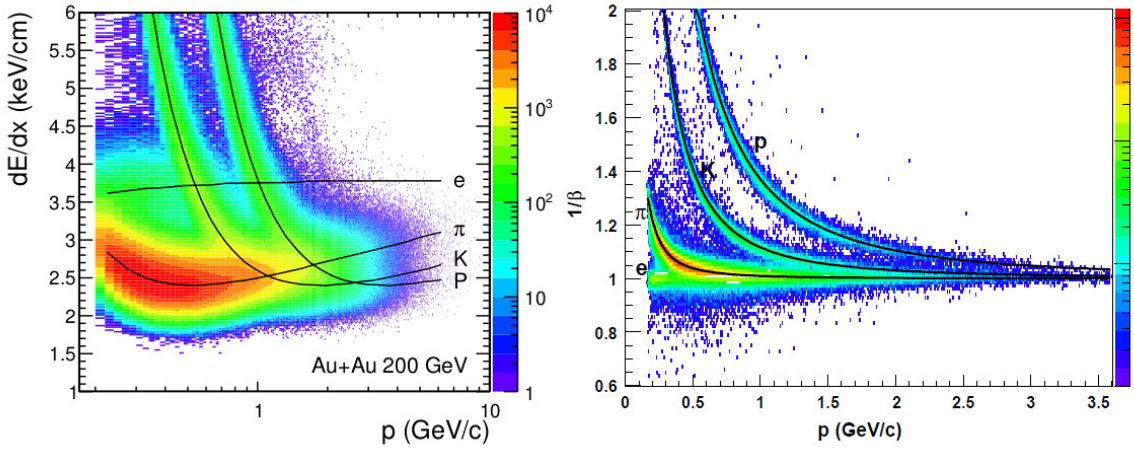

Figure 3.6: Left: The energy loss of the charged particles as a function of their momentum in Au+Au collisions. The expected values for electrons e, pions π, kaons K and protons P obtained from the Bichsel functions are depicted with the black curve [29]. Right: $1/\beta$ of electrons, pions, kaons and protons as a function of their momentum [30].

is given as $\Delta t = t_1 - t_0$. Using the momentum, p, and length s of associated track from the TPC, the average value of the inverse velocity can be determined according to the formula [31]

$$\frac{1}{\beta} = \frac{c\Delta t}{s}. \tag{3.3}$$

Then, the mass m of the particle can be calculated as [31]

$$m = \frac{p}{c}\sqrt{\left(\frac{1}{\beta}\right)^2 - 1}. \tag{3.4}$$

The TOF improves the particle identification capabilities of the TPC. The TOF detector is effective to separate electrons from heavier hadrons at low momentum. Right panel of the Figure 3.6 shows $1/\beta$ as a function of particle momentum for electrons, pions, kaons and protons. The expected values are obtained using the particle masses from the Particle Data Group (PDG)[32]. Together, the TOF and TPC can provide high quality identification of low and intermediate momentum particles − pions and (anti)protons for momenta to ∼7-8 GeV/c, kaons to ∼ 3 GeV/c and electrons from 0.15 GeV/c to 4 GeV/c [33]. To identify high momentum particles other detectors, e.g. the BEMC are used.

3.3.3 Barrel Electromagnetic Calorimeter

The Barrel Electromagnetic Calorimeter (BEMC) allows energy measurements of high transverse momentum particles such as electrons, photons or leptonic decaying hadrons. It covers pseudorapidity $|\eta| < 1$ and full azimuthal angle.

The BEMC has cylindrical shape with radius of ca. 2.2 m. It is situated parallel to the beam axis between the TOF detector and the solenoidal magnet, as can be seen in the Figure 3.3. The BEMC contains 120 calorimeter modules, each of which is divided into 40 towers. The core of each module consists of a lead-scintillator stack and Barrel Shower Maximum Detectors (BSMD)[34]. The schematic drawing of the BEMC module can be seen in the Figure 3.7.

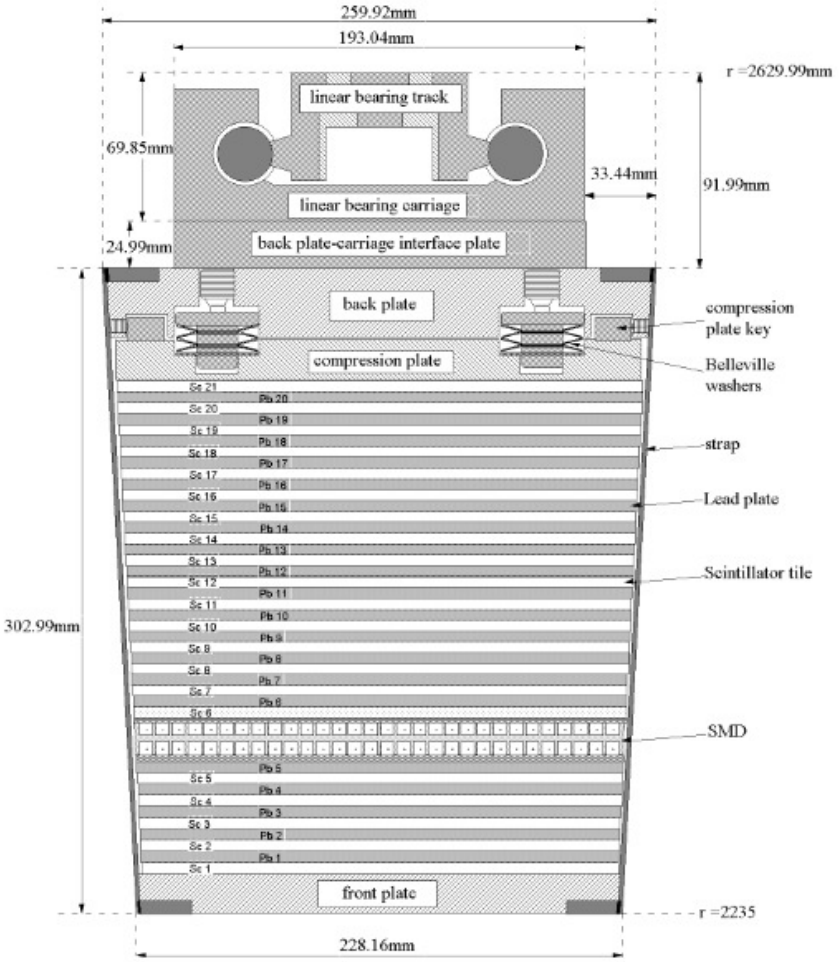

Figure 3.7: Side view of a STAR BEMC module [34].

As charged particles pass through the lead plates, they produce an electromagnetic shower. The scintillator plates convert the electrons from the shower into the light to determine the energy of the shower. Since the BEMC has a total radiation length $20X_0$, it is expected that electrons deposit their whole energy in the calorimeter. The radiation length X_0 is a distance over which a high energy electron loses $1/e$ of its energy by radiation (Bremsstrahlung). For high momentum electrons energy-to-momentum ratio is $E/p \sim 1$ (energy measured by the BEMC, momentum measured by the TPC). Hadrons do not leave their whole energy in the

BEMC, therefore the energy-to-momentum ratio for them is less than 1. Accordingly, high momentum electrons can be distinguished from hadrons [29, 35].

While the BEMC towers provide energy measurements, the high spatial resolution of the position and the shape of the shower is provided by the BSMD. Its schematic view is shown in the Figure 3.8. It is located at the depth of $5X_0$ at which electrons should have produced fully developed shower shape while hadrons not [29].

By measuring the energy loss of high momentum electrons and by detecting their showers the BEMC enables to study rare high p_T processes (jets, leading hadrons, direct photons, heavy quarks) and therefore with its large acceptance it is an important tool in the study of the vector meson production and suppression in heavy ion collisions at RHIC [34].

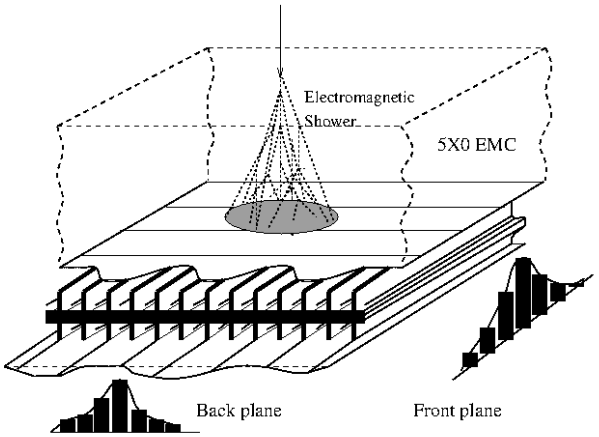

Figure 3.8: Schematic illustration of the STAR BEMC BSMD module [34].

3.3.4 Inner tracking system

The inner tracking system of the STAR detector consists of the newly installed Heavy Flavor Tracker (HFT) and Silicon Strip Detector (SSD) which is often considered to be an outer layer of the HFT. With HFT, open heavy flavor hadrons are reconstructed via displaced decay vertices. Therefore, the main capabilities of the inner tracking system are the improvement of open heavy flavor yields, v_2 and R_{AA} measurements and the ability to distinguish between charm and bottom contributions.

3.3.5 Silicon Strip Detector

The Silicon Strip Detector (SSD) was developed to measure the 2D position of hits and energy loss of charged particles to improve the tracking capabilities of the STAR detector. It is located between the HFT and the TPC at a distance of 23 cm from the beam axis. It covers the pseudorapidity $|\eta| < 1.2$ [36]. The position of the SSD can be seen in the Figure 3.10. The design of the SSD ladders is shown in the Figure 3.9. It consists of two shells, each of which supports 10 carbon fiber ladders. Each ladder supports 16 wafers which are equipped with 768

strips per side [37]. For better $r-\theta$ resolution strips of the SSD are crossed at an angle of 35 mrad [36].

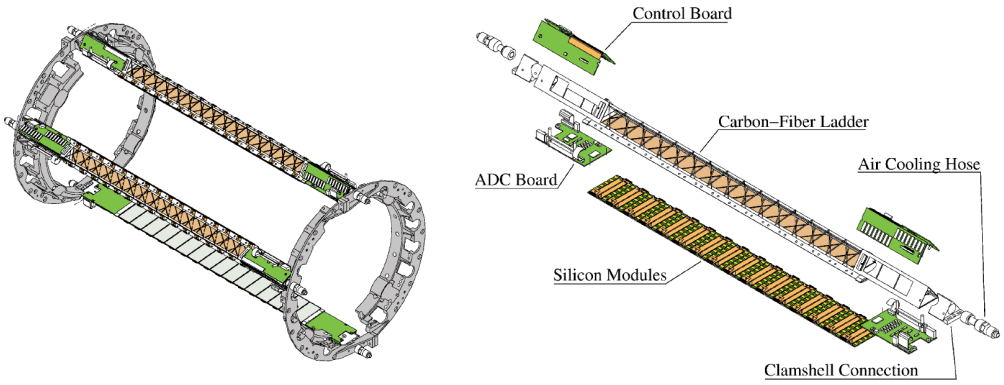

Figure 3.9: The Silicon Strip Detector. Left: Two supporting half-barrels equipped with 3 ladders [37]. Right: A detailed sketch of the SSD ladder [37].

Heavy Flavor Tracker

The HFT is located around the collision point of the STAR detector, in the TPC. Its position is schematically drown in the Figure 3.10. The HFT consists of two subsystems – the silicon pixel detector (PIXEL, 2 layers) and Intermediate Silicon Tracker (IST, 1 layer).

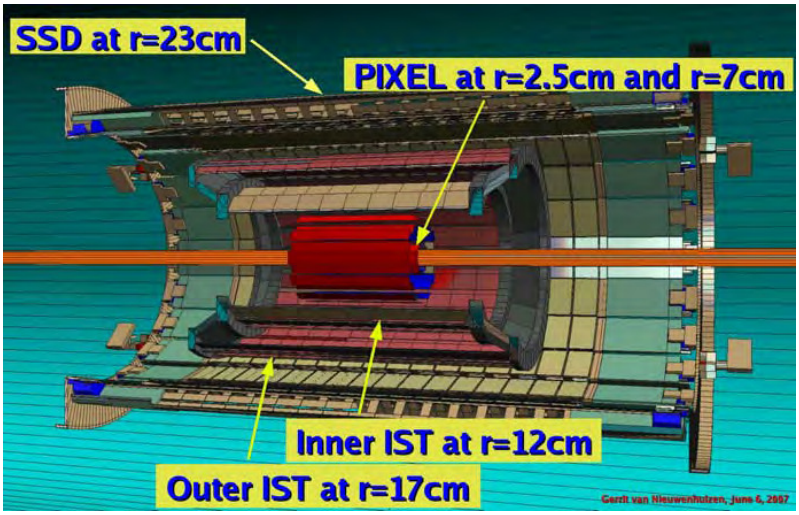

Figure 3.10: The Heavy Flavor Tracker [36].

The PIXEL detector is located very close to the beam pipe inside the IST. It consists of 2 barrel layers of silicon pixel detectors with radii of 2.5 cm and 7 cm. In order to position the

detector in the distance of 2.5 cm from the beam pipe, new, thinner beam pipe was installed [36].

The IST sits between the PIXEL and the SSD. It is a strip detector consisting of two silicon barrel layers with radii of 12 cm (IST1) and 17 cm (IST2). These layers provide space-points in z and $r - \theta$ directions and reduce the number of candidate tracks connected with hits on the outer layer of the PIXEL detector. The IST provides, together with the SSD, connection of track between the TPC and the PIXEL detector [36].

3.3.6 Muon Telescope Detector

The importance of the Muon Telescope Detector (MTD) is in its capability to identify muons − they do not participate in strong interactions and therefore are interesting probes of the strongly-interacting quark-gluon plasma. The MTD enables detection of di-muon pairs from QGP thermal radiation, quarkonia decays or light vector meson decays. It also allows open heavy flavor measurements using semileptonic decays and electron-muon correlations. Although some of these topics can be studied through electrons or photons, they have larger backgrounds than muons. Another advantage of muons is that unlike the electrons, they are not so affected by Bremsstrahlung radiation, i.e. they do not loose so much energy, and thus can provide better mass resolution of vector mesons and quarkonia [38].

In terms of the topic of this thesis, the improvement of quarkonia measurements using MTD is crucial. The fact that quarkonia signals in the di-muon decay channel are cleaner than those in the di-electron decay channel plays an important role especially for different Υ states measurements. Since quarkonia are important in the study of the quark-gluon plasma, measurements provided by MTD in different collisional systems and energies allow to gain better knowledge of nuclear matter effects and thus also of quark-gluon plasma.

The MTD is located behind the iron return bars of the STAR magnet in the distance of ca. 400 cm from the beam pipe. The STAR magnet, used as an hadron absorber, provides background shielding. The MTD covers 45% of the azimuth angle and the pseudorapidity of $|\eta| < 0.5$.

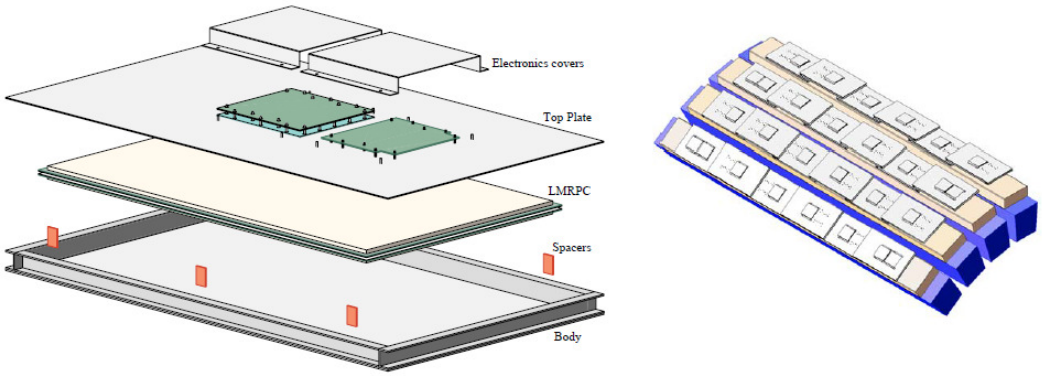

Figure 3.11: Left:The schematic figure of the MTD tray [38]. Right: 6 MTD trays mounted on each of 4 BEMC PMT boxes [38].

The MTD system consists of 122 boxes called trays [39]. An exploded view of an MTD tray and its setting on the STAR can be seen in the Figure 3.11. Each MTD tray consists of aluminium body which is mounted on the support structure of the BEMC, own detecting module, top aluminium plate with a hole in the center to allow the connection of detecting technology with electronics, own electronics and thin aluminium covers which protect the electronics mounted on the top plate [38].

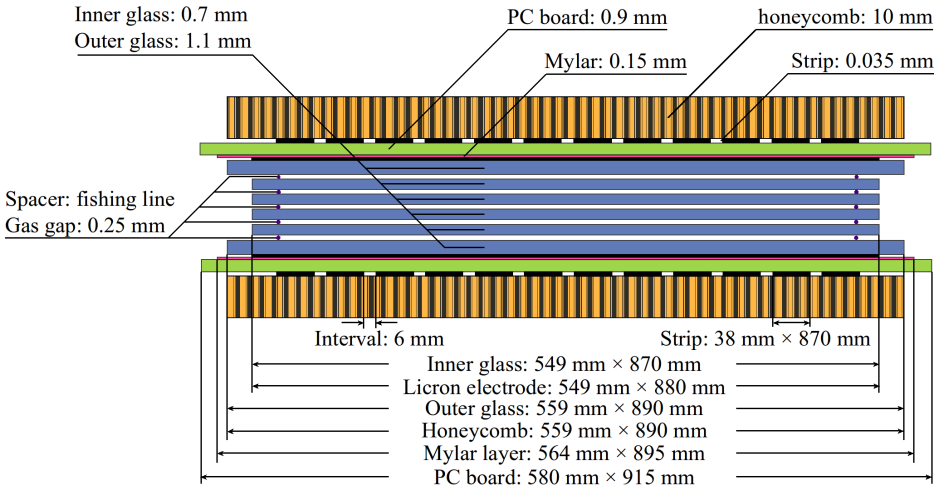

Figure 3.12: Multi-gap Resistive Plate Chamber of the MTD [40].

The MTD technology is based on the Multi-gap Resistive Plate Chambers (MRPC) technology which is similar to the MRPC technology used for the TOF detector. Unlike the TOF MRPCs, the MTD MRPCs are larger and have double-ended read-out strips. The design of MTD MRPCs is schematically shown in the Figure 3.12. "Body" of the MRPC module consists of 6 resistive glass plates resulting in a total of 5 gas gaps. High voltage is applied to electrodes on the outer surfaces of the outer glass plates. A gas-tight aluminium box in which is the MPRC module enclosed is filled with a mixture of 95% Freon and 5% Isobutane [41].

The MRPC technology was developed by the CERN ALICE group [42]. Later it was used and adjusted for the TOF systems of STAR and PHENIX. The principle of the technology is as follows (and is schematically shown in the Figure 3.13): when a charged particle traverses the gas of the conventional wide gap resistive plate chamber,it ionizes the particles of the gas. These can produce avalanches. Than, the avalanche electrons are detected. When there is only one gas gap the avalanche is larger and the local resolution of the particle position is worse. On the contrary, when the wide gap is divided into subgaps, the formed avalanches are smaller and the final resolution is better [42].

Left panel of Figure 3.14 shows projected R_{AA} for simulations of different Υ states as a function of number of participants using the MTD and compared with the values obtained by di-electron channel. Right panel shows first data obtained this year from collisions p+p at energy 500 GeV − signal of J/ψ obtained from di-muon channel using MTD.

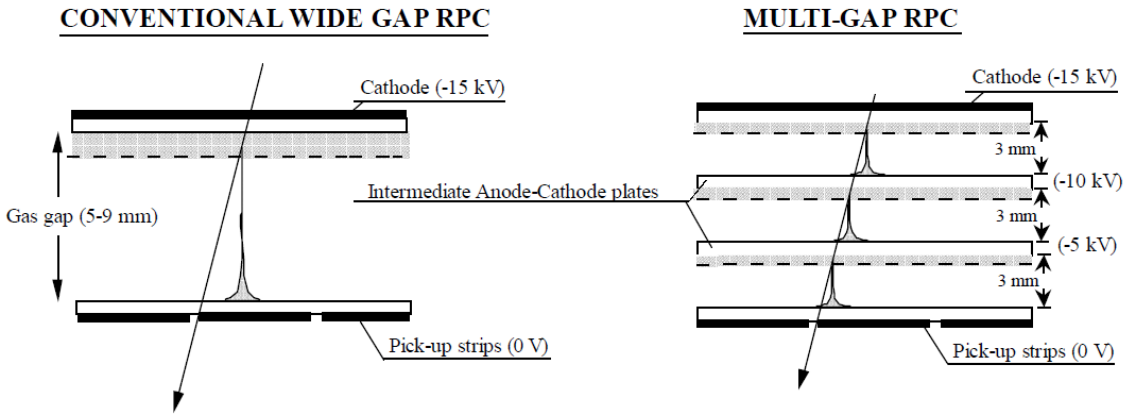

Figure 3.13: Multi-gap Resistive Plate Chamber – principle of operation [42].

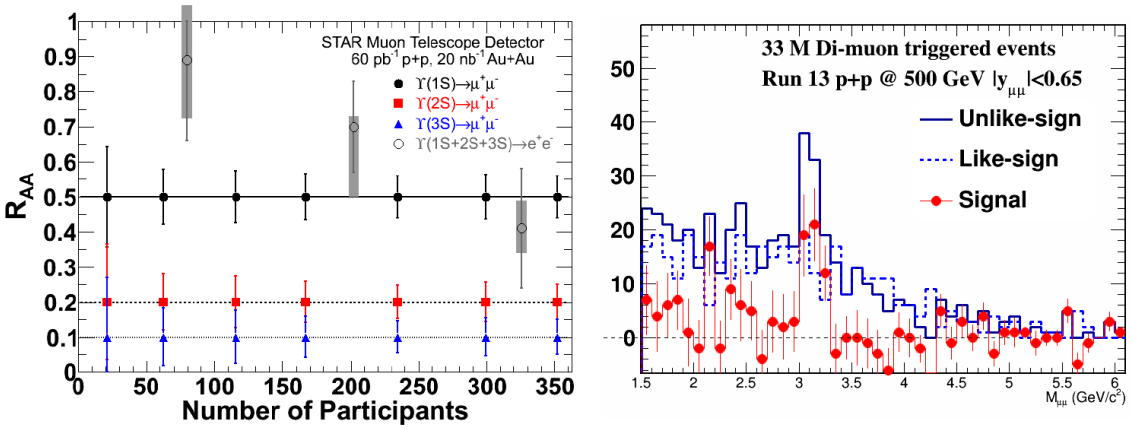

Figure 3.14: Left: Projection of the R_{AA} of different Υ states as a function of number of participants and J/ψ signal obtained with the MTD [43]. Right: J/ψ signal from p+p collisions at 500 GeV [39].

3.3.7 Triggering System

The importance of triggering systems is in the fact that they enable to find small cross section signals from a huge number of events, respectively to decide which collisions are suitable to trigger on and record. Information about the cross sections from the fast detectors is used to determine whether to begin amplification digitization acquisition for slower detectors.

The main detectors used for triggering at STAR are the BBC, VPD and ZDC. Excluding them, the BEMC is used to trigger on events with large energy deposit in a single tower or

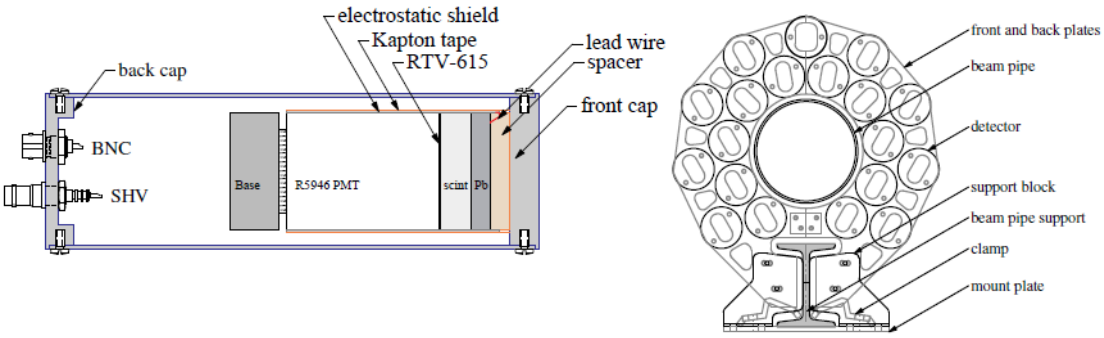

Figure 3.15: Vertex Position Detector. Left: Schematic view of one VPD subdetector [44]. Right: Schematic front view of one VPD [44].

tower cluster (production of high-p_T particles or jets) and the TOF is used to trigger on central heavy ion collisions (by requiring a high occupancy of hits).

Vertex Position Detector

The two Vertex Position Detectors (VPDs) are located very close to the beam pipe ca. 5.6 m from the intersection point. Each VPD consist of 19 subdetectors. Schematic view of VPD and its detector is shown in the Figure 3.15. VPDs detect fragments from the collisions which do not participate in interaction. The time difference between the signals t_{east} of the East and t_{west} of the West VPD determines the primary vertex position of the collision z_{vtx} [44]

$$z_{vtx} = \frac{c(t_{east} - t_{west})}{2}, \tag{3.5}$$

where c is the speed of light. VPD can measure the primary vertex position with resolution $\sim$ 2.5 cm in p+p collisions, $\sim$ 1 cm in Au+Au collisions, respectively. VPDs are important parts of the TOF system. The event "start time" needed for TOF (and also for MTD) is given as [44]

$$t_{start} = \frac{t_{east} + t_{west}}{2} - \frac{L}{c}, \tag{3.6}$$

where L is the distance from East/West VPD to the center of STAR. VPD can measure the "start time" with resolution in the range from $\sim$ 20-30 ps in full-energy Au+Au collisions (for comparison, TOF/MTD measures the "stop time" with resolution $\sim$ 80/100 ps) to $\sim$ 80 ps in p+p collisions [44].

Beam Beam Counter

The two Beam Beam Counters (BBCs) are located ca. 3.5 m from the intersection point of the STAR detector around the beam pipe. The schematic drawing of the BBC is shown in the Figure 3.16. The BBCs consist of two layers of hexagonal blocks. The inner layer contains

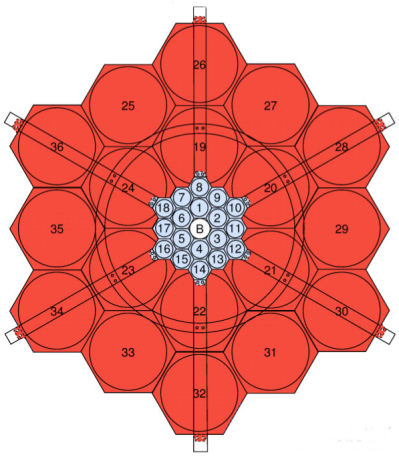

Figure 3.16: The Beam Beam Counter [45].

smaller blocks, the larger blocks form the outer layer. The main capability of the BBCs is to determine the collisional vertex position and collision centrality [29].

Zero Degree Calorimeter

The two ZDCs are located at $|z|$ =18.25 m from the intersection point along the beam axis and outside of the RHIC dipole magnets. Right before each ZDC there are dipole magnets which bend incoming and outgoing beams for collision [27]. Each ZDC is split into 3 modules, each of which consists of tungsten layers and scintillator wavelength shifting fibers which direct Čerenkov radiation to photo-multiplier tube. The ZDCs measure the number of spectator neutrons from collisions, they are used for triggering and beam monitoring [46].

Chapter 4

Heavy Flavor Physics

This chapter provides basic information about physics of heavy quarks in heavy ion collisions. First of all, it explains the importance of heavy quarks in terms of the study of the quark-gluon plasma. Than, general information about heavy flavor production is presented. Several results of measurements of open flavor are shown. In terms of topic of this thesis heavy quarkonia are dedicated separate chapter in which they are discussed in more detail.

4.1 Motivation for heavy quarks

The term heavy quarks, as it is understood in heavy ion collisions, refers to c and b quark (or antiquarks $\bar{c}$, $\bar{b}$). Since the mass of the heavy quarks is significantly larger than the critical temperature T_C, they cannot be produced in the collisions of thermalized partons. Hence, they are produced almost exclusively in the initial parton-parton interactions in high energy collisions. Therefore, their production can be calculated using tools of perturbative QCD. Moreover, the thermalization time of heavy quarks is delayed in comparison with light quarks and comparable with the lifetime of the QGP. Accordingly, in the heavy-ion collisions, created pairs of heavy quarks $Q\bar{Q}$ could "fly through the quark-gluon plasma" in which they are expected to thermalize not or only to some extent [47]. The different character of interaction of heavy quarks with the medium in comparison with light quarks makes them unique tools of the QCD matter. Among others, they could also help to understand the mechanism of parton energy loss.

4.1.1 Heavy Quark Energy Loss

In general, there are two ways of energy loss of heavy quarks in the medium : collisional and radiative.

Collisional energy loss of heavy quarks Q is caused by elastic collisions of heavy quarks Q with light partons (i.e. light quarks q and gluons g). This process can be schematically written as $Qq \rightarrow Qq$ or $Qg \rightarrow Qg$. The collisional energy loss of heavy quarks depends logarithmically on the extreme values of heavy quark momentum $-dE/dx \propto ln(q_{max}/q_{min})$. It has been proved that the energy loss value depends not only on the energy of the quark but also on the temperature [48]. Braaten and Thoma [49] obtained $-dE/dx \approx 0.3$ GeV/fm for a 20 GeV/c

charm quark and $-dE/dx \approx 0.15$ GeV/fm for a 20 GeV/c bottom quark at the temperature 250 MeV.

The radiative energy loss denotes the energy loss of heavy quark through single scattering or the emission of gluon, e.g. $Qq \to Qqg$ or $Qg \to Qgg$. The first model of radiative loss of heavy quarks [50] showed the dependence $-dE/dx \propto ln^2(q_{max}/q_{min})$, which is greater than the collisional energy loss. According to this model the radiative energy loss was calculated: $-dE/dx \approx 12$ GeV/fm for a 20 GeV/c charm quark and $-dE/dx \approx 10$ GeV/ fm for a 20 GeV/c bottom quark at the temperature 500 MeV. Figure 4.1 compares theoretical calculations of collisional energy loss and radiative energy loss given by models [49] and [50].

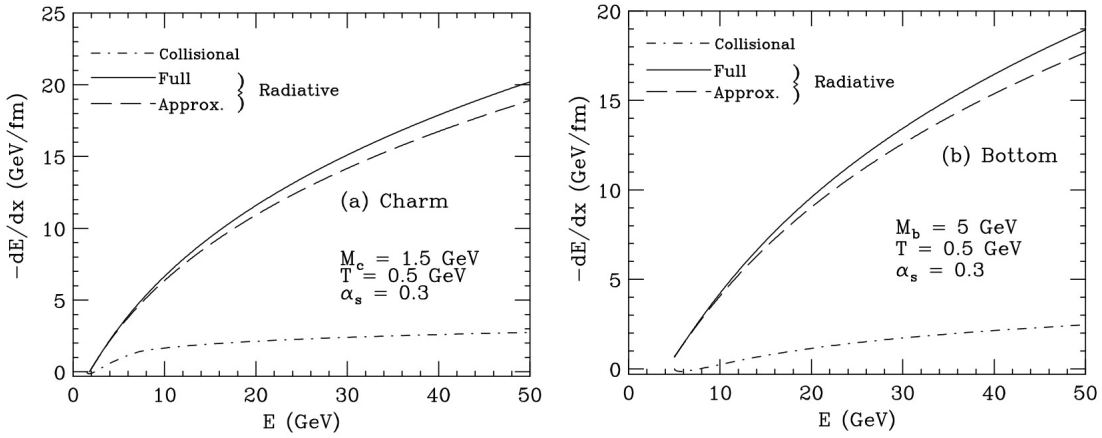

Figure 4.1: The energy loss of c quarks (left) and b quarks (right) as a function of quark energy at the temperature $T = 500$ MeV. [50].

An interesting idea about radiative energy loss of heavy quarks was presented by Dokshitzer and Kharzeev [51]. They showed that the gluon radiation of heavy quarks is suppressed at the angles smaller than $\theta_0 = M/E$ where M is the mass of the heavy quark and E is its energy. Than the distribution of soft gluons radiated by heavy quarks differs from that radiated by light quarks by the factor

$$D = \left(1 + {\theta_0}^2/\theta^2\right)^{-2}. \tag{4.1}$$

This effect is called *dead cone effect*. Accordingly, the heavy quark mass suppresses the gluon radiation and therefore the radiative energy loss of heavy quarks is smaller than for light quarks.

On the other side, later it was shown [52] that the medium induced gluon radiation could fill the dead-cone, so the radiative energy loss of heavy quarks would not be negligible. It was also shown that the radiative energy loss would be smaller for massive quarks than for massless quarks.

Later, the suppression factor of soft gluon emission was modified into [53]

$$D = \left(1 + \frac{M^2}{s\tan\left(\frac{\theta}{2}\right)^2}\right)^{-2}, \tag{4.2}$$

where s is the square power of the center of mass energy. This improved suppression factor is

valid for the whole range of angles $-\pi < \theta < \pi$ and for the full range of masses M. In the case when $M \ll \sqrt{s}$ and $\theta \ll 1$ this improved suppression factor D modifies into expression obtained by Dokshitzer and Kharzeev [51].

Generally, the issue of heavy quark energy loss is not settled yet and it is one of the main current research topics.

4.2 Heavy Flavor Production

As has been already indicated, heavy quarks are produced in the initial parton-parton interactions of the high energy nucleus-nucleus collisions.

Dominant but not the only one process to $c\bar{c}$ or $b\bar{b}$ pair production is a gluon fusion $gg \to Q\bar{Q}$. Another possible process is quark-antiquark annihilation $gg \to Q\bar{Q}$. These processes are processes of the lowest order in perturbative QCD (leading order − LO). Three diagrams of the $Q\bar{Q}$ production through gloun fusion and quark-antiquark annihilation are schematically shown in the Figure 4.2. Moreover, there are also Next-to-leading Order (NLO) corrections on heavy quark production. They include e.g. flavor excitation processes $gg \to Q\bar{Q}$ and gluon splitting, a process which can be factorized into $gg \to gg$ or $gq \to gq$ scattering with one off-shell gluon (i.e. which does not satisfy classical equations of motion) in the final state followed by the evolution of that gluon into a $Q\bar{Q}$ pair [54]. Higher order processes, e.g. Next-to-next leading order (NNLO), are often small and not taken into account.

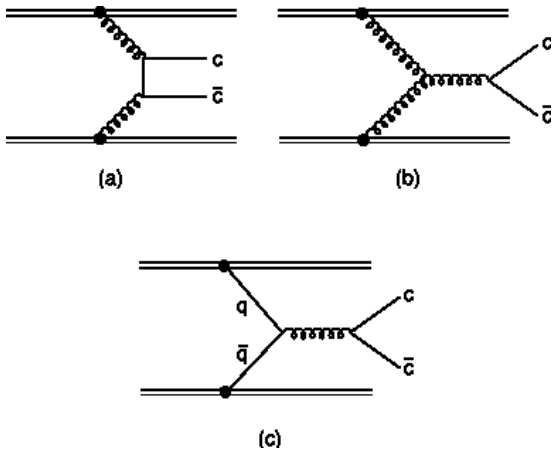

Figure 4.2: The lowest order diagram for $c\bar{c}$ production through gluon fusion (a, b) and quark-antiquark annihilation (c) [55].

The produced $c\bar{c}$ or $b\bar{b}$ pair is expected to form a heavy quarkonium (a bound state of heavy quark and its antiquark, e.g. J/ψ, ψ') or an open heavy flavor hadron (a bound state of heavy quark/antiquark and light antiquark/quark, e.g. B or D meson). Although total heavy quark cross section is calculable using tools of perturbative QCD, heavy quarkonia formation process is still not well understood. Several models of quarkonia production are described in section 5.2. Open heavy flavor mesons are produced from the "not-bound" $Q\bar{Q}$ pairs that combine with light quarks in hadronization phase of the evolution of the high energy collision.

4.2.1 Total heavy quark cross section

In principle, we can calculate the total heavy quark cross section − as mentioned in previous section, it can be obtained theoretically using calculations based on perturbative QCD (at FONNL level, NLO/NNLO calculations). On the other side, experimentally, we measure spectra of produced particles.

"Experimental approach" takes into account the fact that heavy flavor mesons (open heavy flavor specifically) are often observed through their semileptonic decays or hadronic decays. Than, by measuring the decaying products the total heavy quark cross section can be reconstructed. It is a complicated process. In principle, in the case of observed electrons from semileptonic decays of heavy flavor mesons, the electron differential cross section can be expressed as convolution [56]

$$\frac{Ed^3\sigma\left(e\right)}{dp^3} = \frac{E_Q d^3\sigma\left(Q\right)}{dp_Q{}^3} \otimes D\left(Q \to H_Q\right) \otimes f\left(H_Q \to e\right), \tag{4.3}$$

where $E_Q d^3\sigma\left(Q\right)/dp_Q{}^3$ is p_T and y distribution of heavy quarks, $D\left(Q \to H_Q\right)$ describes the fragmentation of heavy quarks into heavy hadrons and $f\left(H_Q \to e\right)$ denotes the fraction of heavy hadrons decaying into electrons. This formula is modified if heavy flavor hadrons (e.g. D mesons) are reconstructed through hadronic decays and does not include the last convolution.

To gain the total $c\bar{c}$ cross section (per nucleon-nucleon pair) by measuring D mesons from their hadronic decays is not a trivial task. First, the number of measured D mesons in a particular decay channel is divided by corresponding branching ratio. Result of this operation gives the total number of produced D mesons. To gain the cross section, the number of D mesons has to be divided by luminosity and extrapolated to the full phase space from the finite detector acceptance. Than, it has to be divided by 2 to get the pair cross section and scaled by number of binary collisions. Finally, the result has to be corrected to account for unmeasured charm hadrons [56].

Figure 4.3 shows the review of measured heavy flavor production cross sections at different experiments in comparison with theoretical predictions. As can be seen from the figures, data are consistent with theoretical predictions within uncertainties.

4.2.2 Heavy flavor measurements

As it was already noted, heavy flavor can be studied through quarkonia or open heavy flavor measurements. Recent heavy quarkonia production measurements are presented in section 5.4. At RHIC, open heavy flavor production can be measured in two ways - by study D meson production or through measuring non-photonic electrons (NPE) from semileptonic decays of heavy flavor hadrons.

D mesons

Direct reconstruction of open charm mesons via hadronic decays (e.g. $D^0 \to K^- + \pi^+$) is a direct access to heavy quark kinematics. Thanks to this method separation of c and b quark contribution is easier. On the other hand, the most significant disadvantages of this method are huge combinatorial background and small branching ratio.

Left panel of Figure 4.4 shows new STAR results of D^0 mesons invariant p_T spectra in U+U collisions at $\sqrt{s_{NN}}$ = 193 GeV (full symbols), Au+Au at $\sqrt{s_{NN}}$ = 200 GeV (open symbols)

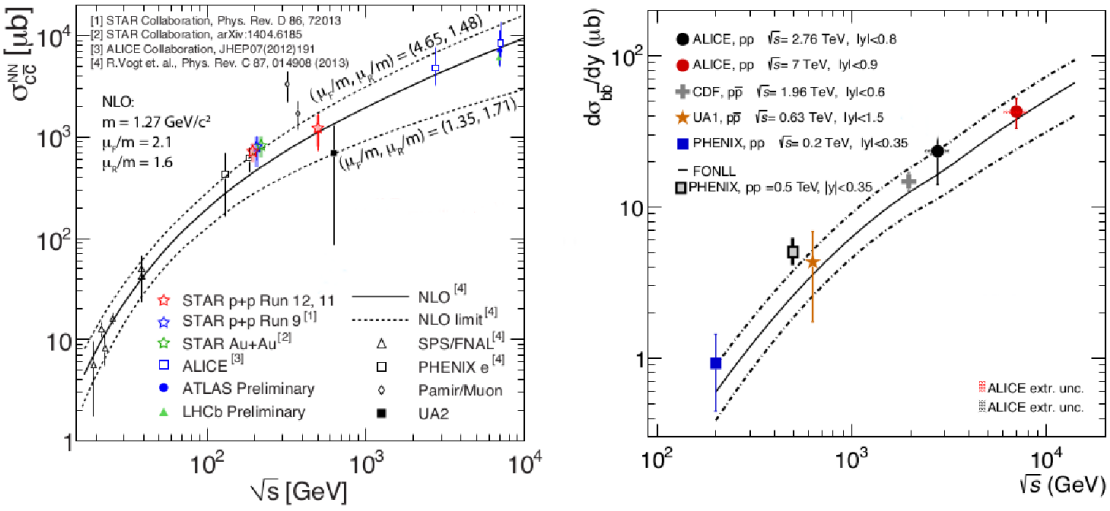

Figure 4.3: Heavy flavor production cross sections. Left: The total $c\bar{c}$ cross section as a function of center of mass energy in collisions p+p (STAR, ALICE,ATLAS) and Au+Au (STAR) compared to NLO predictions [57]. Right: The differential $b\bar{b}$ cross section per rapidity unit as a function of center of mass energy in p+p collisions (PHENIX, ALICE) and p+$\bar{\text{p}}$ collisions (UA1, CDF) compared to FONLL calculations [58].

and $D^0 + D^*$ p_T spectra in p+p, d+Au and Au+Au collisions at 200 GeV. The differential $c\bar{c}$ cross section per unit of rapidity as a function of binary collisions calculated from p+p collisions at 200 GeV can be seen in the right panel of Figure 4.4. Data are compared to FONNL and NLO calculations. In general, we can consider the p+p, d+Au and Au+Au data as consistent and also consistent with given calculations within uncertainties. Since we understand the $c\bar{c}$ production, we can study modification of production.

Left panel of Figure 4.5 shows D^0 R_{AA} as a function of p_T for different centrality ranges in collisions U+U at $\sqrt{s_{NN}}$ = 193 GeV (full symbols) and Au+Au at $\sqrt{s_{NN}}$ = 200 GeV (open symbols) at mid-rapidity. R_{AA} has similar trend in Au+Au and U+U collisions. At mid-p_T an enhancement is observed and towards higher p_T the suppression increases. It also increases towards the most central events. The D^0 suppression for the 0-10% most central collisions at high p_T is similar to that measured for light hadrons − pions. This result is interesting because for light quarks a larger energy loss in the medium is expected and from this point of view, $\pi^{\pm}$ would be suppressed more than D^0. Right panel of Figure 4.5 presents ALICE result of R_{AA} for D (D^0, D^+, D^{*+}) mesons as a function of p_T in Pb+Pb collisions at $\sqrt{s_{NN}}$ = 2.76 TeV. It shows similar suppression of D mesons and charged particles (pions) towards higher p_T. Therefore, challenging results obtained by STAR and ALICE require further study of nuclear matter produced in high energy collisions.

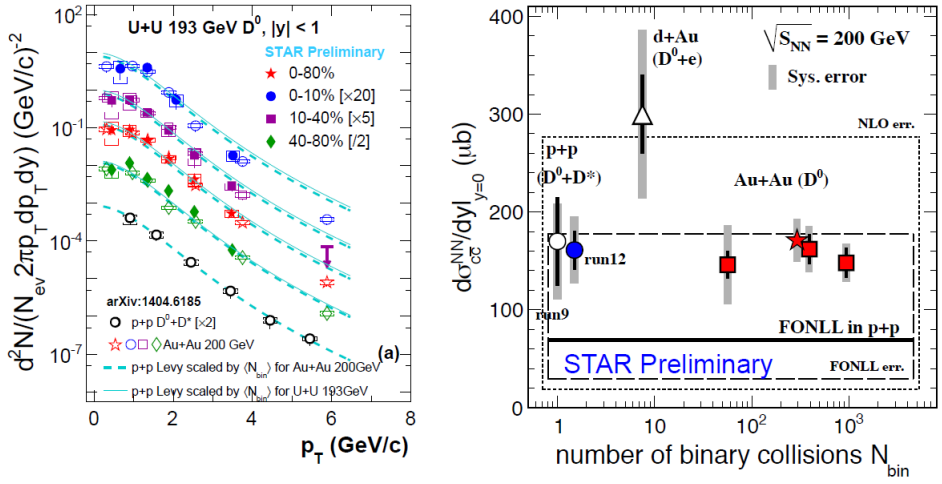

Figure 4.4: Left: D^0 mesons p_T spectra in U+U collisions at $\sqrt{s_{NN}} = 193$ GeV (full symbols), Au+Au at $\sqrt{s_{NN}} = 200$ GeV (open symbols) and $D^0 + D^*$ p_T spectra in p+p collisions at 200 GeV [43]. Right: Differential $c\bar{c}$ cross section per unit of rapidity as a function of number of binary collisions N_{bin} measured in p+p collisions(circles), d+Au collisions (triangle), Au+Au collisions at different centralities (squares) and Au+Au for all centralities combined (star), includes theoretical predictions with errors [59].

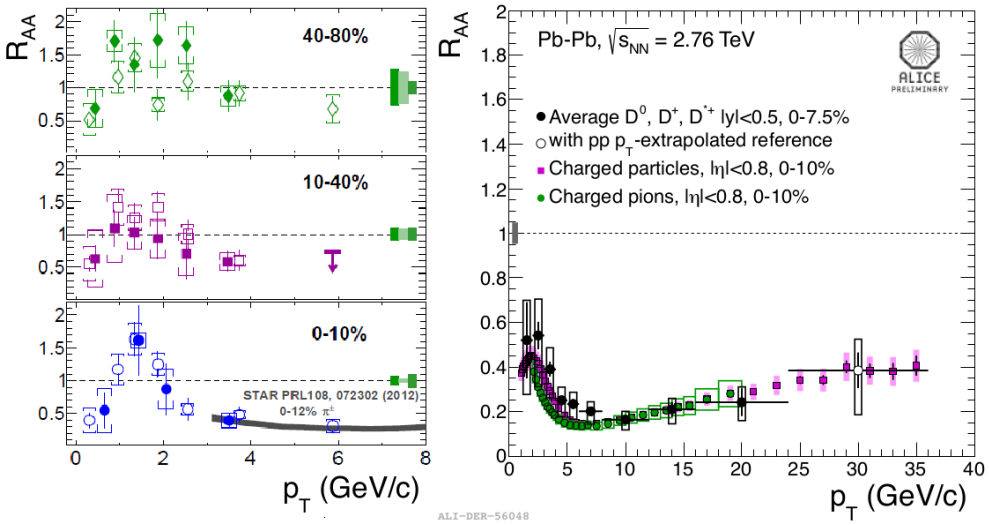

Figure 4.5: Left: D^0 R_{AA} in $\sqrt{s_{NN}} = 200$ GeV Au+Au (open symbols) and $\sqrt{s_{NN}} = 193$ GeV U+U (full symbols) collisions as a function of p_T for different centralities at STAR [43]. Right: R_{AA} for D mesons as a function of p_T compared to charged particles (pions) in Pb+Pb collisions at $\sqrt{s_{NN}} = 2.76$ TeV at ALICE [57].

Non-photonic electrons

The advantage of reconstruction from the semileptonic decays (e.g. $\bar{D^0} \rightarrow K^+ + e^- + \bar{\nu_e}$) is that in comparison with the previous method the branching ratio is higher and also small signal from heavy flavor can be easily separated from the background. The disadvantage is, e.g., that contributions of c and b hadron decays can not be separated.

Measurements of NPE R_{AA} and v_2 are important in the study of different energy loss mechanisms and thermalization of the medium produced in high energy collisions.

Figure 4.6 left shows NPE R_{AA} in Au+Au collisions at $\sqrt{s_{NN}}$ =200 GeV for 0-10% most central collisions. The suppression increases towards higher p_T. Results are compared to several theoretical calculations. Gluon radiative scenario alone (dashed green line) cannot describe large NPE suppression at higher p_T, by adding collisional energy loss to gluon radiative scenario(green line) model describes data better [60].

Figure 4.6 right shows NPE elliptic flow in Au+Au collisions at $\sqrt{s_{NN}}$ = 200 GeV at mid-rapidity and centrality 0-60% and compared to model calculations. For $v_2\{2\}$ an electron is correlated with a single hadron and gives an upper limit on the elliptic flow, while for $v_2\{4\}$ one electron is correlated with 3 hadrons and gives a lower limit [61]. From both methods, data are consistent with each other. At low p_T finite v_2 indicates charm-medium interaction while significant increase of v_2 towards higher p_T could be caused by jet-like correlations or by path length dependence of heavy quark energy loss [60].

Generally, different models describing non-photonic electron suppression and elliptic flow are not always in good agreement with measured NPE R_{AA} and v_2. Therefore, it is a big challenge to describe both NPE R_{AA} and v_2 simultaneously [43].

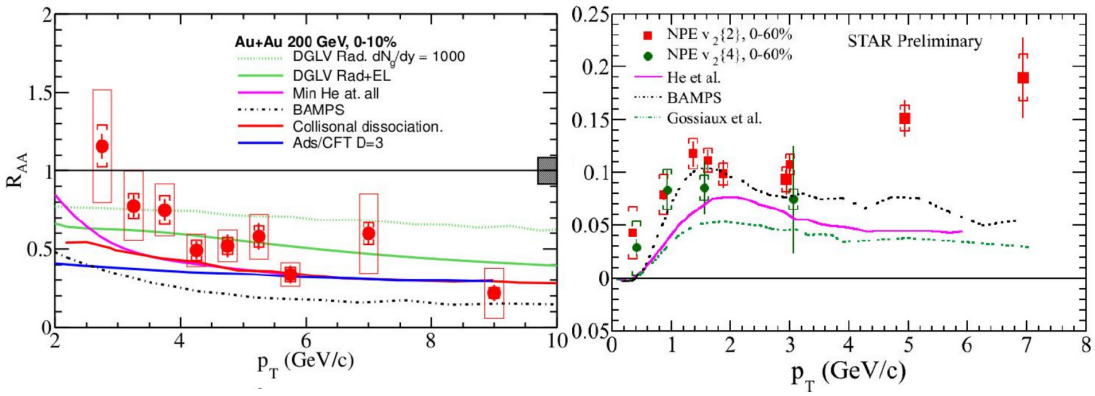

Figure 4.6: Left: NPE R_{AA} in 200 GeV Au+Au collisions at mid-rapidity as a function of p_T for 0-10% most central collisions and compared with different model predictions [60]. Right: NPE v_2 in Au+Au collisions at $\sqrt{s_{NN}}$ = 200 GeV at mid-rapidity and centrality 0-60% and compared to different model calculations [60].

Chapter 5

Heavy Quarkonia

This chapter provides basic information about bound states of heavy quarks called quarkonia. First of all, the overview of different states of quarkonia is given. Than, several quarkonia production models are presented. Particular sections inform about the effect of the quark-gluon plasma on the quarkonia production and about the most significant recent measurements in this field of research.

5.1 Quarkonia Families

The term heavy quarkonia refers to the bound states of heavy quark and its antiquark. In the case of c quark and its antiquark, the corresponding quarkonia are called charmonia, in the case of b quark and its antiquark they are called bottomonia. Figures 5.1 and 5.2 show the so called charmonium family and bottomonium family. In both cases, the "family members" have different properties, such as mass or quantum numbers. For example, the lightest charmonium meson which can be detected via dilepton decay is J/ψ, its excited states include χ_c and ψ'. The lightest bottomonium detectable via dilepton decay is Υ and its excited states are χ_b , Υ', χ_b' and Υ''. Transition lines depicted in the Figures 5.1 and 5.2 represent the decay modes of selected states − the thick transition lines indicate hadronic feed-down decays while the thinner lines indicate radiative decays. Unconfirmed states are shown as dashed lines. The masses, binding energies and radii of selected states of quarkonia are shown in the Table 5.1.

State	J/ψ	χ_c	ψ'	Υ	χ_b	Υ'	χ_b'	Υ'
mass (GeV)	3.10	3.53	3.68	9.46	9.99	10.02	10.36	10.36
Δ E (GeV)	0.64	0.20	0.05	1.10	0.67	0.54	0.31	0.20
radius (fm)	0.25	0.36	0.45	0.14	0.22	0.28	0.34	0.39

Table 5.1: Basic properties of quarkonia − mass, binding energy and radius [55].

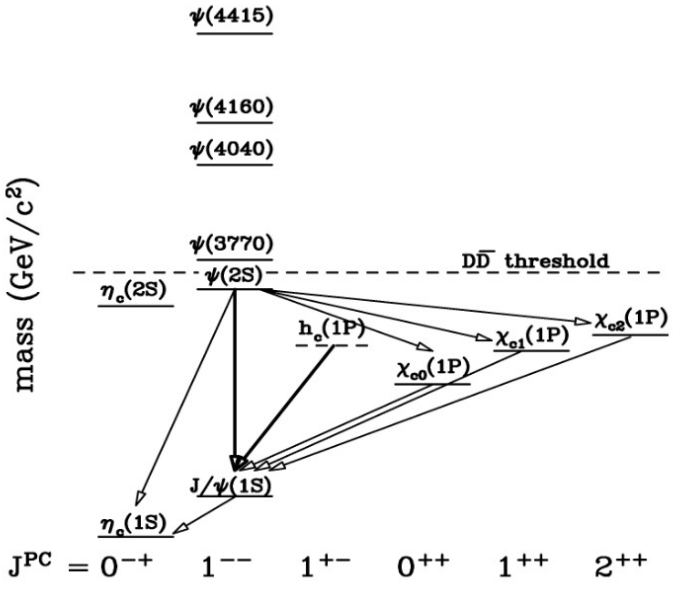

Figure 5.1: The charmonium family [15].

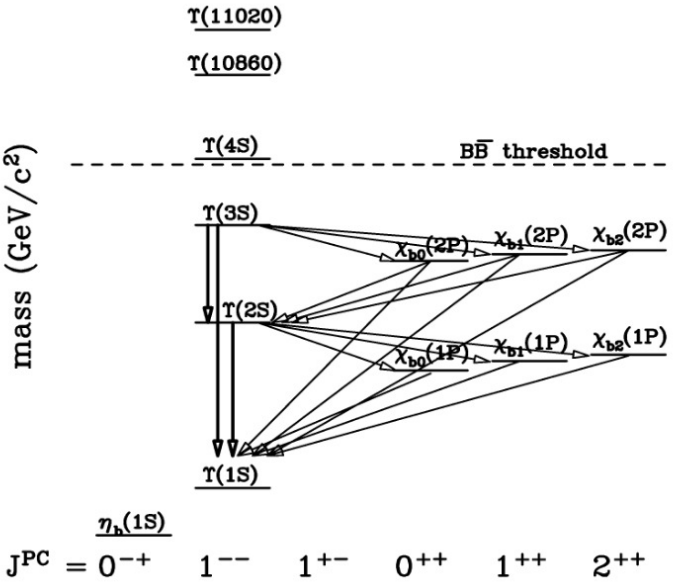

Figure 5.2: The bottomonium family [15].

5.2 Models of Heavy Quarkonia (J/ψ) Production

Although total heavy quark production can be calculated, the production mechanism of heavy quarkonia is, unfortunately, still not well understood. Quarkonia have to be colorless but during their formation they can be in color-singlet or color-octet state. The color neutralization process, when the $Q\bar{Q}$ pair forms a resonance (e.g. J/ψ, Υ) can be described only using models. Several of them, Color Singlet, Color Octet and Color Evaporation Model, are briefly presented in following sections [55].

5.2.1 Color Singlet Model

In the Color Singlet Model (CSM) the produced $Q\bar{Q}$ pair is created only in a color singlet state, it has the same color, spin and angular-momentum quantum numbers as the quarkonium which is to be produced [62]. The lowest order diagram for the J/ψ production from the gluon fusion is schematically shown in the Figure 5.3. The CSM can predict the J/ψ polarization but the value is sensitive to the order of calculation [29]. The leading order(and higher order) CSM calculations were successful in predicting quarkonium production cross section at relatively low energies. Problem of CSM calculation is that they under-estimate quarkonia production at higher energies, e.g. J/ψ in p+p collisions at RHIC [63].

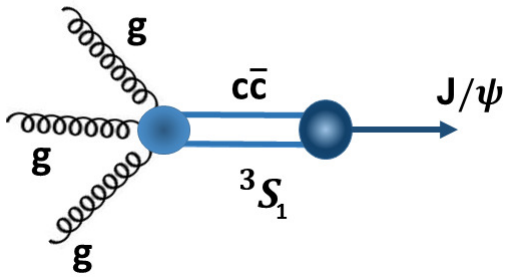

Figure 5.3: The lowest order diagram for the J/ψ production through gluon fusion in CSM.

5.2.2 Color Octet Model and NRQCD

The Color Octet Model (COM) was developed in the non-relativistic QCD (NRQCD) framework [64]. In this approach, the quarkonium can be formed, in addition to a color singlet state in a color octet state which reaches color singlet state through emission of some soft gluons. The COM calculations do not include contributions of feed-down effects and B meson decays on J/ψ production [29]. The lowest order diagram for the J/ψ production in the COM is illustrated in the Figure 5.4.

Generally, NRQCD with color octet contributions successfully describes J/ψ production cross section at experiments at different energies. NRQCD calculations predict transverse polarization of J/ψ and growth of polarization parameter towards higher p_T which does not correspond with experimental data [65].

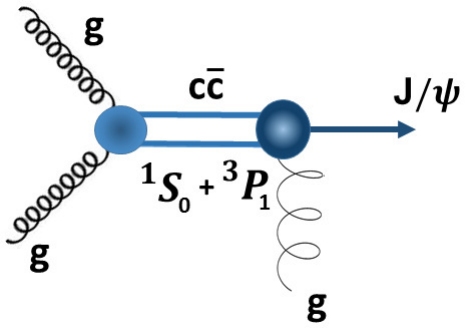

Figure 5.4: The lowest order diagram for the J/ψ production through gluon fusion in COM.

5.2.3 Color Evaporation Model

In Color Evaporation Model(CEM), the total quarkonium cross section is calculated as a fraction of all heavy quark-antiquark ($Q\bar{Q}$) pairs with the mass less than twice the mass of the lightest corresponding open heavy flavor meson [62]. The hadronization process ($Q\bar{Q}$ to quarkonium states) is accompanied by the emission of the soft gluons. The color neutralization process is provided than through the interaction of the $Q\bar{Q}$ pair with the collision-induced color field − therefore "color evaporation" model. Figure 5.5 shows the lowest order diagram for the J/ψ production through the gluon fusion in the Color Evaporation Model [15]. The CEM does not take into account color, angular momentum or spin of the $Q\bar{Q}$ pair. It does not predict J/ψ polarization and does not include feed-down from B meson decays [48]. Among other models, it describes the total quarkonium cross section best.

For example, the CEM model was successful to describe cross section for inclusive J/ψ production in p+p collisions for entire range of transverse momentum and is also able to describe measured Υ cross sections in p+p collisions well across a wide range of collision energy as can be seen in Figure 5.6 [63].

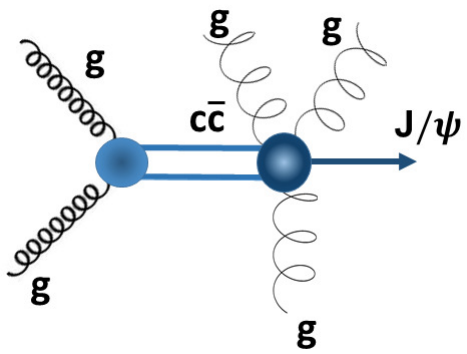

Figure 5.5: The lowest order diagram for the J/ψ production in CEM.

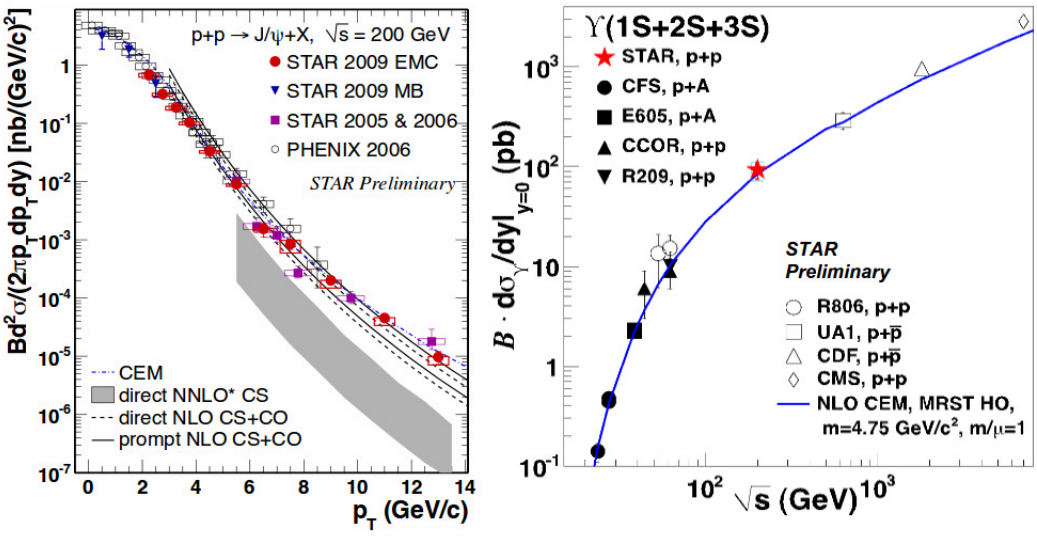

Figure 5.6: Left: The J/ψ invariant cross section as a function of p_T in p+p collisions at STAR compared to other measurements and to theoretical predictions [63]. Right: The Υ cross section as a function of collision energy $\sqrt{s}$ measured at different experiments (symbols) and compared to CEM prediction [63].

5.2.4 J/ψ polarization

Production models (COM, CSM, CEM) can describe the J/ψ production cross sections. To distinguish between production models, other observables are needed. One of them is J/ψ polarization (spin alignment). The models of quarkonia production assume different p_T-dependence of the polarization, especially at high p_T. Therefore, J/ψ polarization measurements can prove the suitability of the models. The polarization of spin-1 quarkonia (like J/ψ) is studied via the angular distribution of their dilepton decay products (e^+e^-). It is often described in the helicity frame, where polar axis (z) corresponds to the flight direction of the J/ψ in the center-of-mass frame of the colliding hadrons [66]. The angular distribution of the decay lepton pair can be expressed as [67]

$$\frac{d^2N}{d(cos\theta)d\phi} \propto 1 + \lambda_\theta cos^2\theta + \lambda_\phi sin^2\theta cos(2\phi) + \lambda_{\theta\phi} sin(2\theta) cos\theta, \tag{5.1}$$

where θ is the polar angle, ϕ is the azimuthal angle and λ_θ, λ_ϕ are the angular decay coefficients. The polar angle θ is the angle between the positive lepton (e^+) momentum vector in the J/ψ rest frame and the J/ψ momentum vector in the laboratory frame [67].

In hadron-hadron collisions, polarization measurements are often constrained to measurements of the distribution as a function of polar angle θ. Integrating over the azimuthal angle, from the above formula the distribution can be written as

$$\frac{dN}{d(cos\theta)} \propto 1 + \lambda_\theta cos^2\theta, \tag{5.2}$$

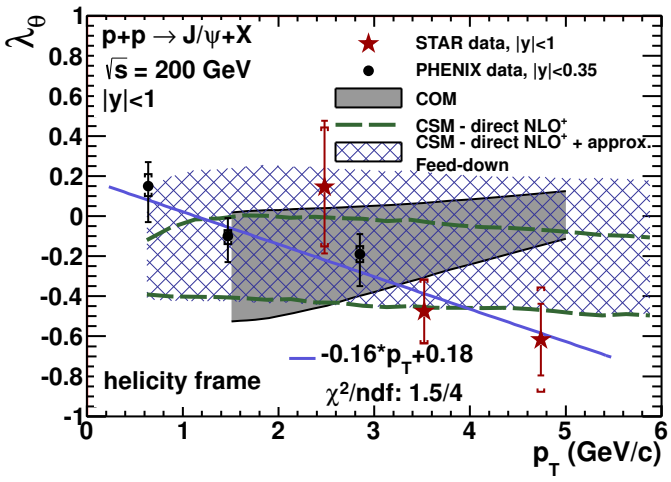

Figure 5.7: The polarization parameter λ_θ as a function of J/ψ p_T [67].

where the parameter λ_θ denotes the polarization $\lambda_\theta = 1$ represents the full transverse polarization and $\lambda_\theta = -1$ the full longitudinal polarization [67].

Figure 5.7 refers to J/ψ polarization measurement at the STAR experiment in p+p collisions at $\sqrt{s}$ =200 GeV. It shows the polarization parameter λ_θ as a function of J/ψ p_T. The result includes direct J/ψ production as well as feed-down from heavier charmonium states (ψ', χ_C) and from B meson decays. Results from the STAR at $|y| < 1$ and 2 GeV/c < p_T <6 GeV/c are compared with the PHENIX data at mid-rapidity $|y| < 0.35$ and with the predictions of the models – LO COM model for direct J/ψ production (gray area) and NLO$^+$ CSM model (green dashed lines show the range of λ_θ for the direct J/ψ, the hatched blue band is the extrapolation of λ_θ for the prompt J/ψ). The data from STAR and PHENIX are consistent with each other. They show λ_θ as the decreasing function of p_T – as the p_T increases the trend towards the longitudinal J/ψ polarization is observed. This result is not consistent with predictions of the COM for direct J/ψ production which expects increase of λ_θ towards higher p_T. On the other hand, data are consistent with the NLO$^+$ CSM model within uncertainties [67].

5.3 Quarkonia in Heavy Ion Collisions

The heavy quarkonia suppression in heavy ion collisions has been predicted as a signature of the quark-gluon plasma [68]. It was expected, that the suppression was caused by the color screening in the quark-gluon plasma.

However, not all the observed suppression of quarkonia production in nucleus-nucleus collisions compared to the scaled proton-proton collisions has to be the signature of the quark-gluon plasma. The heavy quarkonia suppression was observed also in p+A collisions, where the QGP formation is not expected. Moreover, similar quarkonia suppression observed in various experiments operating at different energies and different energy densities lead to the idea that suppression mechanisms could be supplemented by secondary quarkonia production mecha-

nisms. Therefore, it is necessary to take into account various effects of the medium produced in collisions that could modify the quarkonia production.

Following sections provide overview of nuclear matter effects on quarkonia production. It is a difficult task to categorize them, therefore they are divided into effects generally considered as a sign of quark-gluon plasma and other effect which can occur not only in A+A but also those present in p+A or p+p collisions.

5.3.1 Quarkonia as a signal of QGP

This section focuses on the most frequently considered effects on quarkonia production − quarkonia melting and recombination.

Quarkonia melting

At the temperature $T = 0$ as is in p+p or p+A collisions, the potential describing the quarkonium bound state can be written as in the formula (1.1). Than, by using the potential (1.1) in solving the Schroedinger equation [69]

$$\left[2m_Q - \frac{1}{m_Q}\nabla^2 + V(r)\right]\phi_i(r) = M_i\phi_i(r), \tag{5.3}$$

where m_Q is the mass of the charm or bottom quark and M_i is the mass of the particular quarkonium state, the quarkonium state masses or average sizes (radii) can be calculated.

Increasing the temperature T, the potential (1.1) is modified due to color screening and takes the form [15]

$$V(r,T) = \sigma r_D(T)\left(1 - exp\left[-r/r_D(T)\right]\right) - \frac{4\alpha_s}{r}exp\left[-r/r_D(T)\right], \tag{5.4}$$

where r_D is the Debye screening radius. The color screening has the similar meaning as the Debye screening of an electric field − when a charged particle is placed into the plasma or electrolyte it polarizes the surrounding medium and, therefore, the charge of the particle is screened. If the quarkonium is placed in the quark-gluon plasma of sufficient temperature, the deconfined quarks and gluons weaken the interaction between the heavy quarks, the string tension between them vanishes and the $Q\bar{Q}$ can no longer form a bound state.

The color screening is determined by the Debye screening radius or the screening mass $\mu(T) \sim 1/r_D$. The Debye screening radius sets the distance in which the color effect of the heavy quark persist and outside of which the color charge of the heavy quark is screened. It can be calculated according to formula [13]

$$r_D(T) = \frac{1}{\sqrt{\left(\frac{N_c}{3} + \frac{N_f}{6}\right)g^2T}}, \tag{5.5}$$

where N_c is the number of colors, N_f is the number of flavors and $g^2 = 4\pi\alpha_s$. As can be seen from the formula, r_D decreases with increasing the temperature. The temperature at which r_D reaches the radius r of the quarkonium, is the dissociation temperature, T_D. When $r > r_D(T)$ at $T > T_c$ the quarkonium can no longer form a bound state. Since the radii of different quarkonia states vary they break up at different temperatures − the excited states

of J/ψ and Υ have larger radii and smaller binding energy at $T = 0$ than J/ψ and Υ so it is expected that they melt at lower temperature. Therefore, the presence of particular states in the quark-gluon plasma provides a "thermometer" of the medium [15].

The above described model of quarkonia melting is simplified. There are different models which calculate quarkonia dissociaton temperatures. Overview of these models can be seen in the Figure 5.8 which shows temperature T relative to the critical temperature T_c at which different quarkonium states are dissociated in the quark-gluon plasma.

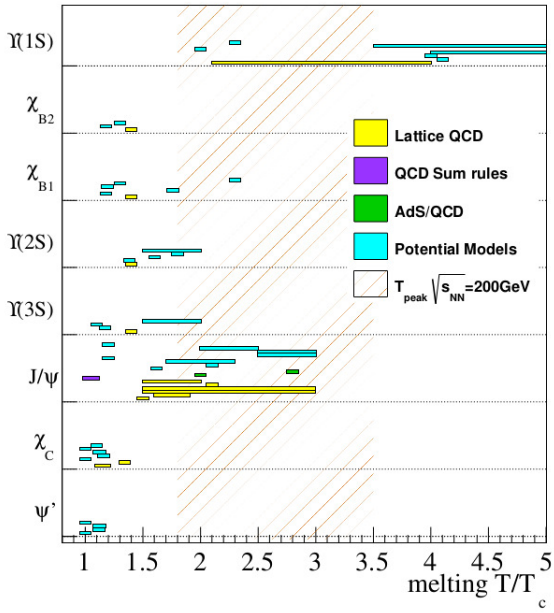

Figure 5.8: The dissociation temperature range for different quarkonium states, calculated using different techniques (Lattice QCD, QCD sum rules, Ads/QCD, potential models). The shaded band represents the hydrodynamic estimation for the peak temperature reached in Au+Au collisions. Estimations were performed using different T_c values. Each horizontal bar represents one estimation, the temperature extension of estimation denotes the range where the quarkonium state undergoes modifications until it completely melts [70].

Recombination

It could be expected that at some sufficiently high temperatures selected quarkonia states in quark-gluon plasma will melt and their production will be suppressed. However, the production of J/ψ in nucleus-nucleus collisions can be enhanced through the recombination (statistical regeneration) of single thermalized c and $\bar{c}$ quarks. These charm and anti-charm quarks flow through the quark-gluon plasma and at $T = T_c$ they undergo the hadronization process.

The number of J/ψ created in the recombination process is approximately proportional to ${N_c}^2/N_h$ where N_c is the number of created c quarks and N_h is the number of produced hadrons. N_c scales with the number of inelastic nucleon-nucleon collisions and increases with

$\sqrt{s}$. On the other side, N_h scales with the number of the participant nucleons. In more central collisions, the number of nucleon-nucleon collisions is larger than the number of the participant nucleons. Accordingly, the recombination of J/ψ is expected to be more significant in more central collisions and at higher energies of collisions [71]. Hence, at sufficiently high energy the recombination mechanism leads to J/ψ production enhancement. This prediction is illustrated in the Figure 5.9 which shows the probability of J/ψ production as the function of energy density. At high energy experiments the enhancement through recombination cannot be negligible. This effect on J/ψ production is expected to be smaller at STAR than at ALICE experiment which operates at higher energies and where the total $c\bar{c}$ production cross section is significantly larger, see Figure 4.3. On the other hand, at STAR and also at ALICE, the total $b\bar{b}$ production cross section is smaller than $c\bar{c}$. Therefore, the effect of recombination on Υ is less significant.

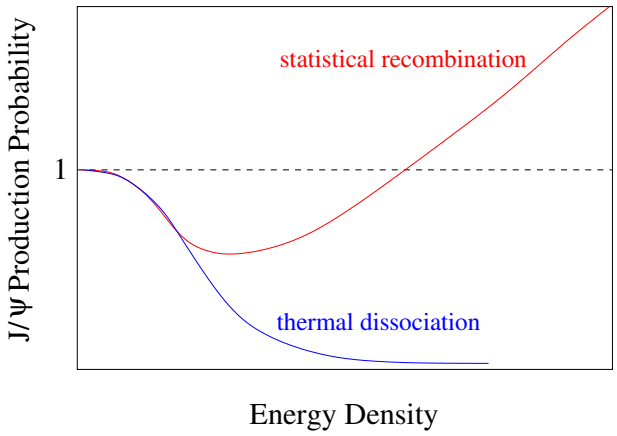

Figure 5.9: J/ψ enhancement through statistical regeneration: J/ψ production probability as the function of energy density [69].

5.3.2 Other effects on quarkonia production

In the process of quarkonia formation during the collision different nuclear matter effects can influence resulting quarkonia yield.

Nuclear shadowing, Cronin effect and nuclear absorption are commonly called "cold nuclear matter effects". Nuclear shadowing and Cronin effect influence the production of $Q\bar{Q}$ pair in the initial state of the collision. Nuclear absorption occurs in the "pre-quarkonium" phase when the $Q\bar{Q}$ pair already exists but before resonance like J/ψ is formed [72].

In A+A collisions, due the presence of QGP in the evolution, the quarkonia are suppressed because of so called "melting" and "leakage" but their production could also be enhanced through recombination. Effect, which can influence quarkonia production in both, A+A and p+A collisions, in the final stage of the collision is co-mover absorption.

Following sections present selected nuclear matter effects in the order they are expected to be present in the evolution of the system. They do not include effects of melting and

recombination described in the previous section. Also, feed-down effects are included, since they have significant influence on quarkonia production.

Different models try to describe quarkonia production suppression and enhancement in different collisional systems considering that above mentioned effects are not negligible. Figure 5.10 shows comparison of two commonly used theoretical models (of Zhao and Rapp [72] and Liu et al. [73]) for J/ψ production that also include additional effects on J/ψ production.

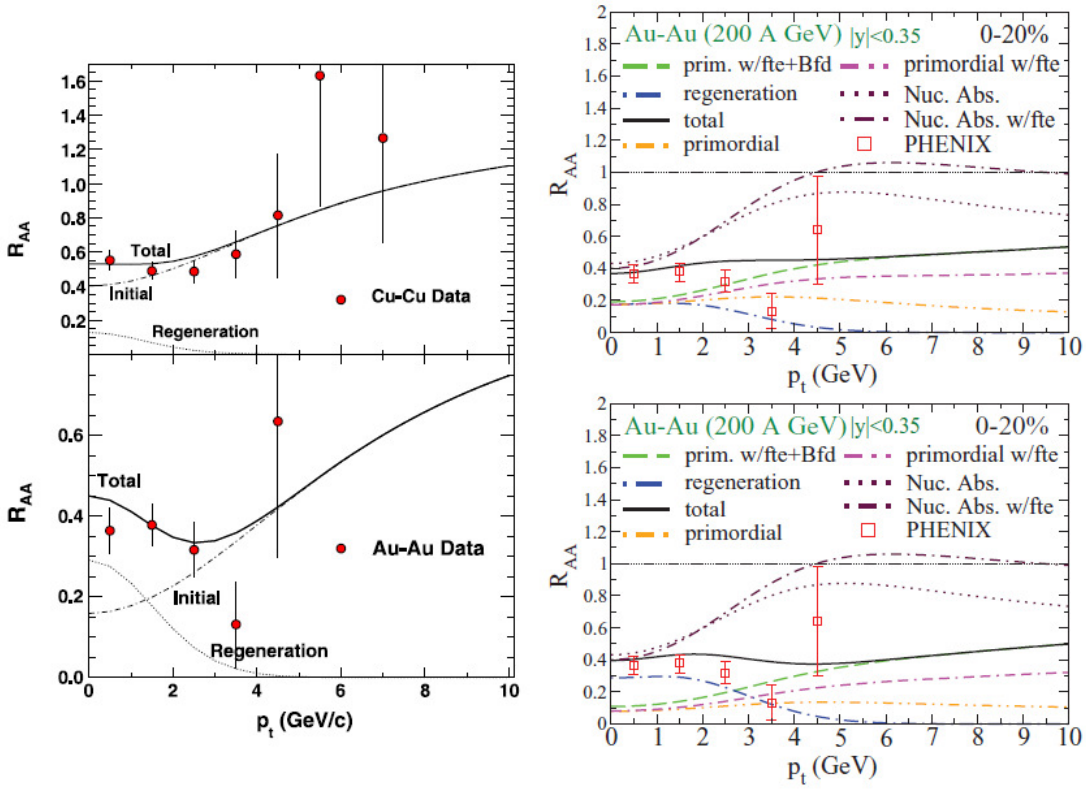

Figure 5.10: J/ψ R_{AA} as a function of p_T. Left: Data measured in Cu+Cu (STAR) and Au+Au (PHENIX) collisions in central rapidity region compared to model of J/ψ production, only initial production(dot-dashed), only regeneration (dotted) and both contributions (solid line) [73]. Right: Model calculations compared with measured data in $\sqrt{s_{NN}} = 200$ GeV central Au+Au collisions at $|y| < 0.35$. Different calculations include just primordial production, B-meson feed down(Bfd) contribution, formation time effects (fte), nuclear absorption effects and all mentioned effects on J/ψ production. Upper panel is for strong- and lower panel is for weak-binding scenario [72].

Here we look at these two models to demonstrate the different behavior of contributions on J/ψ production. R_{AA} for J/ψ is given as a function of p_T. Left panel [73] shows comparison of measured data and models in Cu+Cu (STAR) and Au+Au (PHENIX) collisions in central

rapidity region. Different contributions to calculations take into account only initial production (dot-dashed), only regeneration (dotted) and both contributions (solid line) on J/ψ production. Right panel [72] shows comparison of model with measured data in $\sqrt{s_{NN}} = 200$ GeV central Au+Au collisions at $|y| < 0.35$. Different parts of calculations include just primordial production, B-meson feed down contribution, formation time effects, nuclear absorption effects and all mentioned effects on J/ψ production. Upper panel is for strong-binding (primordial production is dominant and anomalous suppression originates from dissociation of ψ', χ_c) and lower panel is for weak-binding (regeneration yield become comparable to primordial production) scenario. The detailed description of these two models of J/ψ binding is well beyond the scope of this thesis but we can note that general behavior of the different contributions to J/ψ contribution is very similar.

Nuclear shadowing

Partonic content of hadrons can be described by parton distribution functions (PDF) − the momentum fraction distribution functions of the partons within a hadron. As experimental results suggest that nucleus cannot be treated as a superposition of nucleons, its nuclear parton distribution functions (nPDF) have to be modified relative to PDFs in a proton [72]. The effect of this modification is called nuclear shadowing. The first parametrization of the parton distribution functions modification was done by EKS98 group [74] and is also commonly used in the present.

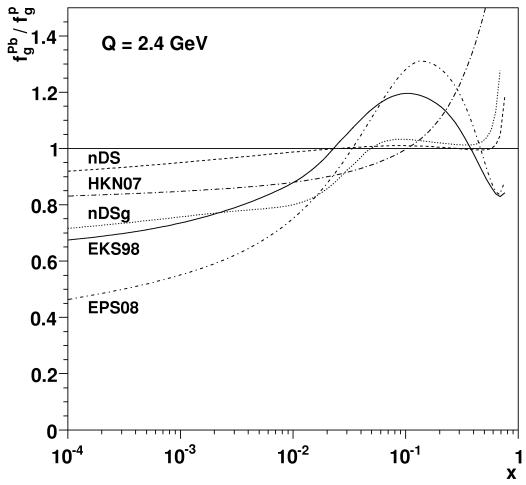

Figure 5.11: Different parametrizations of gluon nPDF modifications. The modification is given as the ratio of lead nPDF and proton PDF ${f_g}^{Pb}/{f_g}^{p}$ as a function of nucleus momentum fraction carried by parton x [75].

Since $c\bar{c}$ or $b\bar{b}$ pairs are produced dominantly via gluon fusion, their production is sensitive to the modification of the gluon nPDFs. Although nuclear modifications of quark or antiquark densities can be relatively well measured, the gluon density modifications are not measured directly. Current parametrizations of nPDFs modify nuclear gluon density variously, from no

effect to very significant shadowing for low fraction $x \simeq 10^{-4}$ of the nucleus momentum carried by gluon and strong antishadowing for $x \simeq 0.1$ as can be seen from the Figure 5.11.

Cronin effect

The Cronin effect was discovered in p+A collisions as a hardening of the p_T spectra relative to p+p collisions for p_T higher than 1-2 GeV and corresponding depletion seen at low p_T [76]. The effect was interpreted as arising from the multiple scatterings of partons from the proton off partons from the nucleus in the initial state of the collision [77]. Due to the multiple scattering partons suffer energy loss, often called initial state energy loss in the nuclear medium. In elastic collisions, partons with no initial transverse momentum transform part of their longitudinal momentum into transverse direction − they acquire a transverse momentum kick [78]. Hence, this effect leads to higher p_T of produced $Q\bar{Q}$ pairs (and then quarkonia) in A+A or p+A collisions relative to p+p collisions [79, 15].

Nuclear absorption

Nuclear absorption denotes the dissociation of pre-quarkonium states $Q\bar{Q}$ by passing-by-nucleons [72]. In p+A or A+A collisions, the pre-quarkonium $Q\bar{Q}$ pair is produced at some point of the nucleus and scatters with nucleons on its path with some absorption cross section. This causes the dependence of quarkonia production on the number of nucleons A [80]. Since collision time in high energy A+A collisions at RHIC (~ 0.1 fm/c) is smaller than the starting time of medium evolution (~ 0.5 fm/c) and smaller than quarkonia formation time (~ 0.5 fm/c) the effect of nuclear absorption can be neglected [73].

"Leakage" effect

In terms of the heavy ion collisions, the so called "leakage" effect is associated with quarkonia which are not present in the medium during its evolution for the whole time and for this reason are not subject to dissociation. This effect is dominant for higher p_T quarkonia, low p_T quarkonia stay longer in the collisional system and are more suppressed. So, in comparison with suppression caused by color screening which is dominant at lower p_T, the leakage effect increases quarkonia R_{AA} mainly at higher p_T [81, 82].

Co-mover interactions

In the final state of the evolution of the collision, as quarkonia traverse the medium they can interact with co-moving constituents of matter (hadrons) formed in the collision and dissociate. The survival rate of quarkonia moving through the produced medium can be approximately expressed as [69]

$$S_i = exp\left[-\sigma_i n \tau_0 ln\left(n/n_f\right)\right], \tag{5.6}$$

where σ_i is the dissociation cross section, n the initial density of the medium after formation time τ_0 and n_f "freeze-out" density. Since densities of hadronic matter are small (< 0.5 fm^{-3}) and cross sections for collisions (quarkonium-hadron) also small, the effect of quarkonium suppression through co-mover interactions is often neglected [80].

Feed-down Effects

In addition to J/ψ which are produced directly, there are other observed sources of J/ψ mesons. These are feed-down from higher excited states or from decays $B \rightarrow J/\psi$. About 30% of $J/\psi s$ observed in elementary collisions come from the radiative decays of χ_c, about 10% come from ψ' hadronic decays. These states are expected to melt easier than the strongly bound J/ψ. Hence, their contribution to J/ψ in the QGP of the temperature greater than their dissociation temperature will cease.

By analogy, in the case of Υ in elementary collisions, 50% of them come from direct production, 30% from $\chi_b(1P)$ states, 10% from direct Υ' states and 10% from $\chi_b(2P)$ states [83].

Accordingly, the quarkonia production measured in heavy ion collisions could be suppressed even if the system has not reached the sufficient energy density to break-up lowest energy states [55].

5.4 Selected results of quarkonia measurements

This section provides information about selected recent results of quarkonia R_{AA} and v_2 measurements at the STAR experiment and compares them with results obtained at other experiments (ALICE, PHENIX, CMS).

5.4.1 Production modification of J/ψ

In general, there are various medium effects (as described in previous section) that can modify the measured J/ψ production. Different R_{AA} measurements as a function of transverse momentum, centrality or rapidity and also v_2 measurements are (among other reasons) crucial to study the medium created in the heavy ion collisions.

J/ψ R_{AA} as a function of transverse momentum

Figure 5.12 shows J/ψ p_T spectra in Au+Au collisions at $\sqrt{s_{NN}}$ =200 GeV at STAR. Measured data are presented in four centrality ranges (0-60%, 0-20%, 20-40%, 40-60%) and compared to theoretical models. As can be seen from the figure, the measured spectra can be well described by the model which includes contribution from suppression of initial production and from $c\bar{c}$ recombination. It can also be seen that the regeneration as a production mechanism grows with the centrality. This trend is important when we look at J/ψ suppression as a function of centrality.

To quantify J/ψ suppression, nuclear modification factor R_{AA} was measured as a function of transverse momentum p_T. Result can be seen in the Figure 5.13. R_{AA} as a function of p_T is shown for centralities 0-60%, 0-20%, 20-40% and 40-60% . STAR data obtained for low p_T ($p_T < 5$ GeV/c) at $|y| < 1$ (closed black circles) are compared with high p_T results (5 GeV/$c < p_T < 10$ GeV/c) (open blue circles). The results are also compared to the PHENIX data (open black squares) in $|y|$ <0.35. Data are consistent with theoretical models (Zhao and Rapp [72], Liu et al. [73]) described in section 5.3.1 which include J/ψ suppression due to color screening and enhancement due to statistical regeneration. Model by Zhao and Rapp also includes contribution from B feed-down and formation time effects on J/ψ production [84].

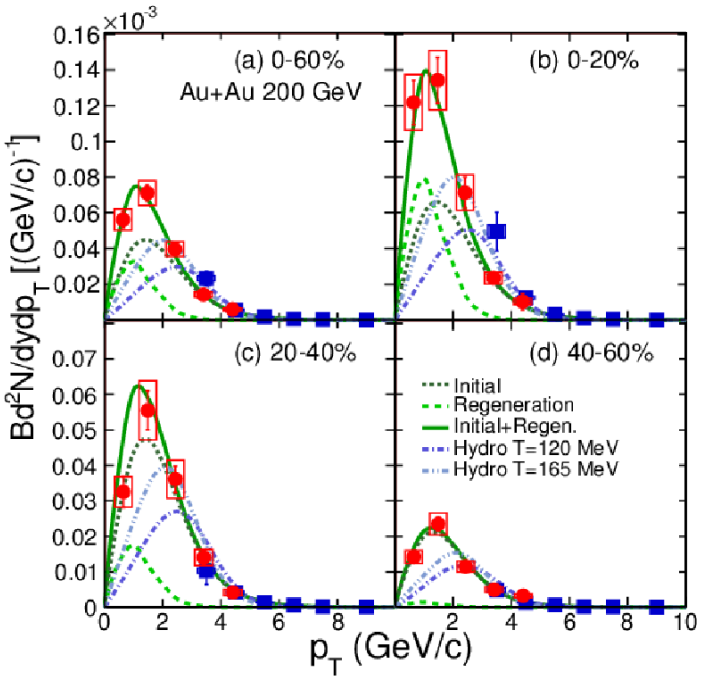

Figure 5.12: J/ψ yield as a function of p_T in Au+Au collisions at $\sqrt{s_{NN}} = 200$ GeV at STAR for centralities 0-60%, 0-20%, 20-40% and 40-60% at $|y| < 1$ for low p_T (red circles) and for high p_T (5 GeV/c < p_T < 10 GeV/c, blue squares). Compared to theoretical models [84].

Results show that the suppression of J/ψ increases towards lower p_T and towards central collisions. Even though that in the lower p_T region significant contribution of recombination on J/ψ production is expected, we observe clear suppression due to the melting. It is of interest also to look at higher p_T region where the effect of recombination is expected to vanish, as shown in Figure 5.10. As can be seen, at higher p_T the suppression vanishes for more peripheral events, however there is still some suppression present in the most central collisions. This high p_T region is hence of interest because it carries cleaner signal about the melting. It is then interesting to compare suppression between high and low p_T region separately as a function of centrality. This is shown in the left panel of Figure 5.14. As can be seen, the suppression in high p_T region is always smaller than in low p_T region. One can see that data are consistent with no suppression in peripheral collisions but they show significant suppression towards central collisions.

Right panel of Figure 5.14 shows R_{AA} as a function of centrality for high p_T regions – for $p_T > 5$ GeV/c at $\sqrt{s_{NN}} = 200$ GeV in Au+Au collisions at STAR and for 6.5 GeV/c < p_T < 30 GeV/c at $\sqrt{s_{NN}}$ =2.76 TeV in Pb+Pb collisions at CMS. The CMS data clearly show higher suppression than STAR data. This result could be explained as a consequence of much higher energy density at CMS than at STAR and, therefore, more significant melting. In this case the resulting R_{AA} should not be influenced by recombination since we look at high p_T data and, as was already mentioned, for high p_T the effect of recombination on J/ψ production is

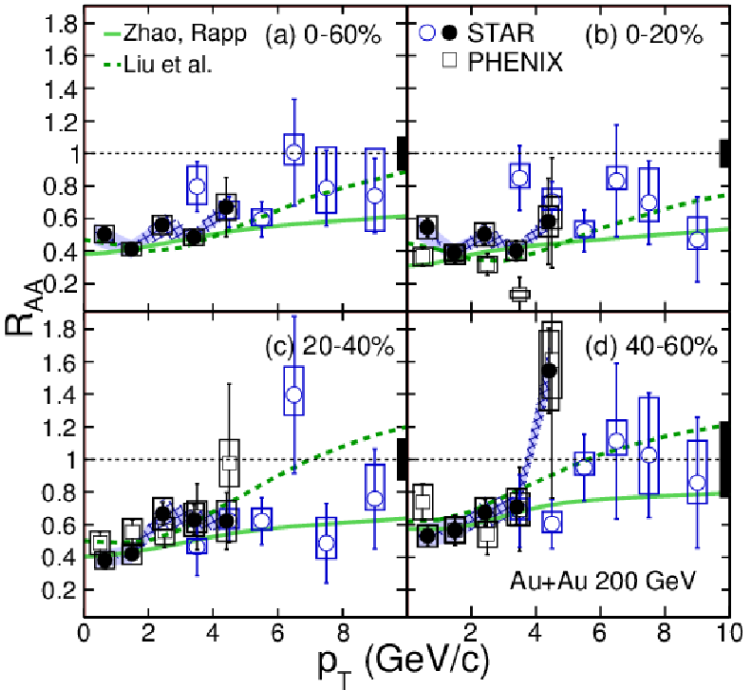

Figure 5.13: J/ψ R_{AA} as a function of p_T in Au+Au collisions at $\sqrt{s_{NN}} = 200$ GeV at STAR for centralities 0-20%, 20-40%, 40-60% and 0-60% at $|y| < 1$ for low p_T (closed black circles) and for high p_T (5 GeV/c $< p_T <$ 10 GeV/c, open blue circles). Compared to data measured by PHENIX at $|y| < 0.35$ (open black squares) and to theoretical models [84].

expected to vanish.

J/ψ R_{AA} as a function of centrality

To understand effects on J/ψ production better, R_{AA} was measured as a function of N_{part} for different energies of collision per nucleon-nucleon pair ($\sqrt{s_{NN}} = 200$ GeV, 62.4 GeV and 39 GeV) in Au+Au collisions at STAR. It could be expected that at lower energes, and therefore, lower energy densities of collisions the relationship between directly produced and regenerated J/ψ would differ from that observed at higher energies. Nevertheless, left panel of Figure 5.15 shows similar suppression for all three energies.

Right panel of Figure 5.15 shows J/ψ R_{AA} as a function of N_{part} in Au+Au collisions at $\sqrt{s_{NN}} = 200$ GeV at STAR at high p_T, low p_T and compares these data with results from SPS. The centrality dependence of STAR high and low p_T data was already described. The interesting thing about the results shown in the right panel of the Figure 5.15 is that the suppression of STAR low p_T data is very similar to suppression obtained by fixed target experiments NA38 (S+U collisions at beam energy of 200 GeV) NA50 (Pb+Pb collisions at beam energy of 158 GeV) and NA60 (In+In collisions at beam energy of 158 GeV) of SPS, although the collisional

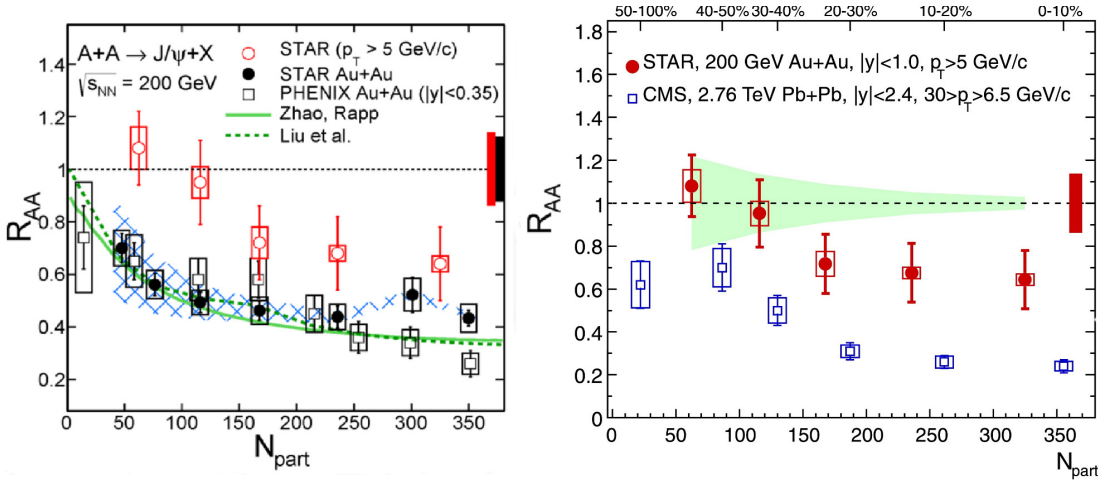

Figure 5.14: Left: J/ψ R_{AA} as a function of N_{part} in Au+Au collisions at $\sqrt{s_{NN}}$ = 200 GeV (closed black circles), for p_T >5 GeV/c (open red circles) at STAR and compared to data from PHENIX [85]. Right: J/ψ R_{AA} as a function of N_{part} in Au+Au collisions at $\sqrt{s_{NN}}$ = 200 GeV at STAR (closed red circles) for p_T >5 GeV/c and in Pb+Pb collisions at $\sqrt{s_{NN}}$ = 2.76 TeV at CMS (open blue squares) for 6.5 GeV/c < p_T < 30 GeV/c [86].

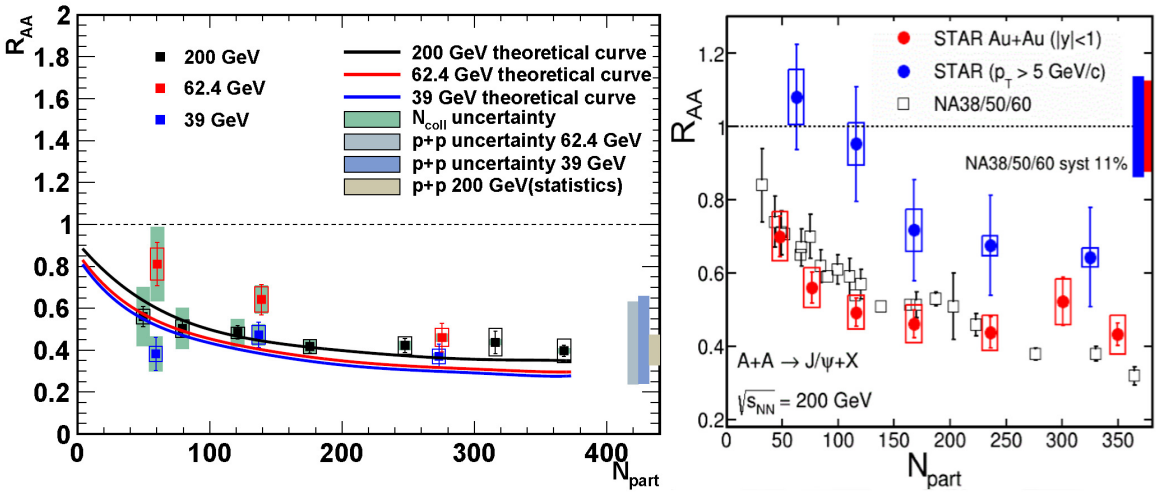

Figure 5.15: Left: Low p_T J/ψ R_{AA} as a function of N_{part} in Au+Au collisions at $\sqrt{s_{NN}}$ = 200 GeV, 62.4 GeV and 39 GeV at STAR compared to theoretical models [43]. Right: J/ψ R_{AA} as a function of N_{part} in Au+Au collisions at $\sqrt{s_{NN}}$ = 200 GeV at STAR at high p_T (blue circles), low p_T (red circles) and compared to data from SPS − NA38/50/60 (squares) [87].

systems at SPS and RHIC differ and we could expect different interplay of the melting and recombination on resulting R_{AA}. However, data indicate that possible different contributions counterbalance with each other. This comparison is even more interesting as we have available results from LHC experiments.

Since $c\bar{c}$ production cross section (see Figure 4.3) and energy density of the medium at LHC is larger than at RHIC, it was expected that J/ψ R_{AA} as a function of number of participants N_{part} could follow different trends at LHC and RHIC. Unlike at RHIC where strong suppression towards higher N_{part} was expected, at LHC the suppression of J/ψ could be more "compensated" by the enhancement through recombination.

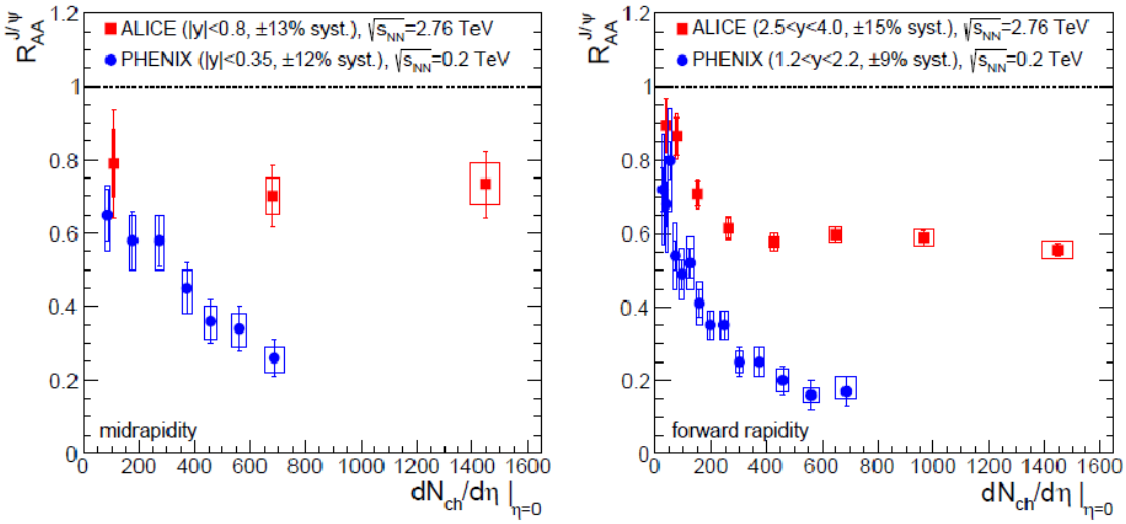

Figure 5.16: J/ψ R_{AA} as a function of $dN_{ch}/d\eta$ in Pb+Pb collisions at $\sqrt{s_{NN}} = 2.76$ TeV by ALICE compared to data measured by PHENIX in Au+Au collisions at $\sqrt{s_{NN}} = 0.2$ TeV at mid-rapidity (left panel) and at forward rapidity (right panel) [88].

Comparison of results measured at RHIC and LHC in the Figure 5.16 shows J/ψ R_{AA} as a function of number of charged particles per pseudorapidity unit $dN_{ch}/d\eta$ (which proportional to energy density and therefore, also centrality).

Left panel shows the R_{AA} at midrapidity and right panel at forward rapidity. In general, one can see a striking difference in R_{AA} between LHC and RHIC data, especially when compared with Figure 5.15 where almost no difference between SPS and RHIC data is observed. As can be seen the R_{AA} of J/ψ at LHC is much higher than at RHIC.

Let us remind that we have already discussed in the right panel of Figure 5.14 comparison between LHC and RHIC results only for high p_T region (where recombination is negligible) and the relationship between LHC and RHIC was completely opposite, i.e. the R_{AA} at CMS was much smaller than at STAR.

These comparisons of RHIC and LHC high and low p_T results support the idea of strong effect of recombination at LHC on J/ψ production in low p_T regions.

J/ψ R_{AA} as a function of rapidity

We can also see from the Figure 5.16 that R_{AA} is higher at midrapidity than at forward rapidity. The higher suppression at forward rapidity at RHIC can be clearly seen also from the Figure 5.17 which shows J/ψ R_{AA} as a function of rapidity y in Au+Au collisions at $\sqrt{s_{NN}} =$ 200 GeV at PHENIX. The y-dependence of R_{AA} is given for two centrality ranges – 0-20% (left) and 20-40% (right).

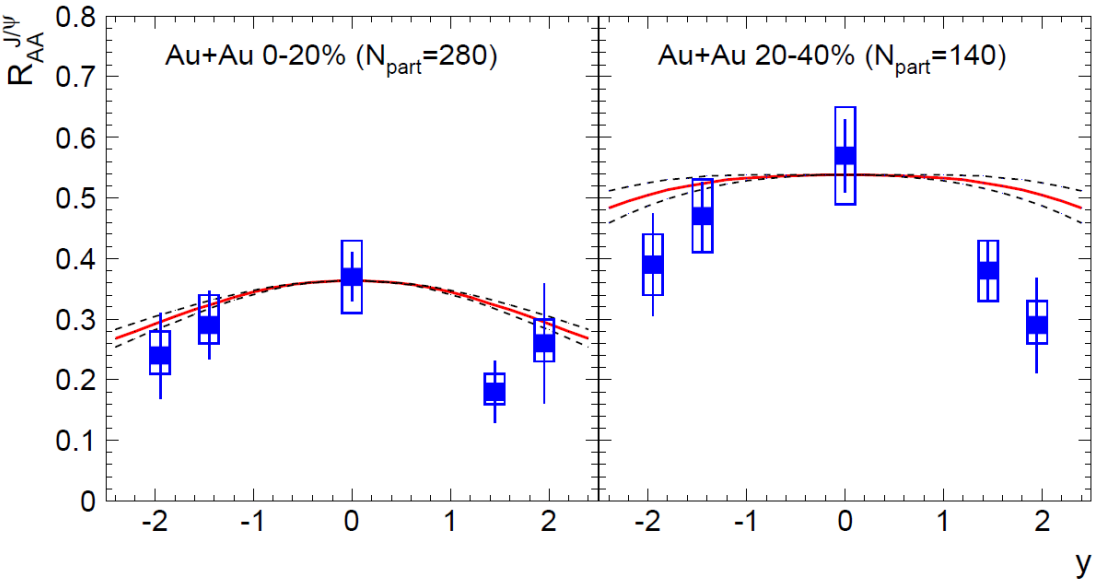

Figure 5.17: J/ψ R_{AA} as a function of rapidity y in Au+Au collisions at $\sqrt{s_{NN}} = 200$ GeV at PHENIX for centrality 0-20% (left) and 20-40% (right) [89].

It is also interesting task to study R_{AA} p_T dependence at different rapidities. Figure 5.18 shows J/ψ R_{AA} as a function of p_T in Au+Au collisions at STAR (for centrality 0-60%), at PHENIX (centrality 0-40%) and in Pb+Pb collisions at ALICE (0-40%) at midrapidity (left panel) and at forward rapidity (right panel) for 0-20% of the most central collisions.

From these figures we observe that at both experiments, LHC and RHIC, there is stronger suppression at forward rapidity than at midrapidity. If one considers only the melting effects on quarkonia in QGP one would naturally expect opposite behavior since the effects of QGP should be present at midrapidity. The increase of suppression towards forward rapidity could be explained as an effect of vanishing recombination. However, there are also possible CNM effects, as described in section 5.3.2, and they can play different role at forward rapidity and midrapidity. In order to correctly interpret the results we need to be able to disentangle these effects.

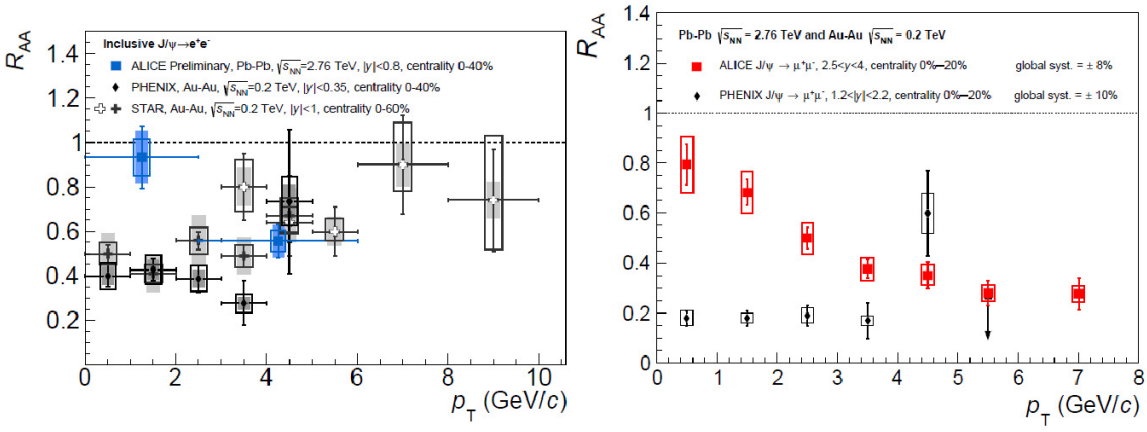

Figure 5.18: J/ψ R_{AA} as a function of p_T in Pb+Pb collisions at $\sqrt{s_{NN}} = 2.76$ TeV by ALICE compared to data measured by PHENIX in Au+Au collisions at $\sqrt{s_{NN}} = 0.2$ TeV and STAR in Au+Au collisions at $\sqrt{s_{NN}} = 0.2$ TeV at mid-rapidity (left panel) and at forward rapidity (right panel) [88].

5.4.2 Quarkonia suppression in d+Au collisions

As it was shown, "non-QGP" CNM effects may influence the production of quarkonia. Hence, these effects need to be understood for conclusive interpretation of measured data. We need to study CNM effects as a function of collision energy, centrality and rapidity. We can study these effects in collision system in which is nuclear matter present but QGP is not created. At RHIC we utilize for these studies collisions of d+Au.

Left panel of Figure 5.19 shows R_{dAu} for J/ψ measured in d+Au collisions at $\sqrt{s_{NN}} =$ 200 GeV as a function of p_T. Data from STAR and PHENIX are compared to theoretical predictions for cold nuclear matter effects. The CNM effects under consideration are nuclear shadowing due to modification of nPDFs (using EPS09 parametrization) and the nuclear absorption. As can be seen from the figure, the CNM effects are not very strong. The data show that nuclear shadowing together with nuclear absorption are needed for the description of results.

STAR has also measured the modification of Υ production in d+Au collisions. The rapidity dependence of nuclear modification factor for Υ (1S+2S+3S) in d+Au collisions at $\sqrt{s_{NN}} =$ 200 GeV is shown in the right panel of Figure 5.19.

The STAR R_{dA} results (pink stars) were supplemented by results of PHENIX (green diamonds) and compared to theoretical predictions. Shaded region denotes prediction of CEM calculations with EPS09 nPDF parametrization which includes nuclear shadowing but does not include nuclear absorption. Data were also compared to models which include initial state parton energy loss (dashed line) and combination of energy loss and shadowing (dashed-dotted line). Models are in agreement with data within uncertainties except the $y \sim 0$ region [90] supporting again the idea that nuclear shadowing is needed for description of CNM effects.

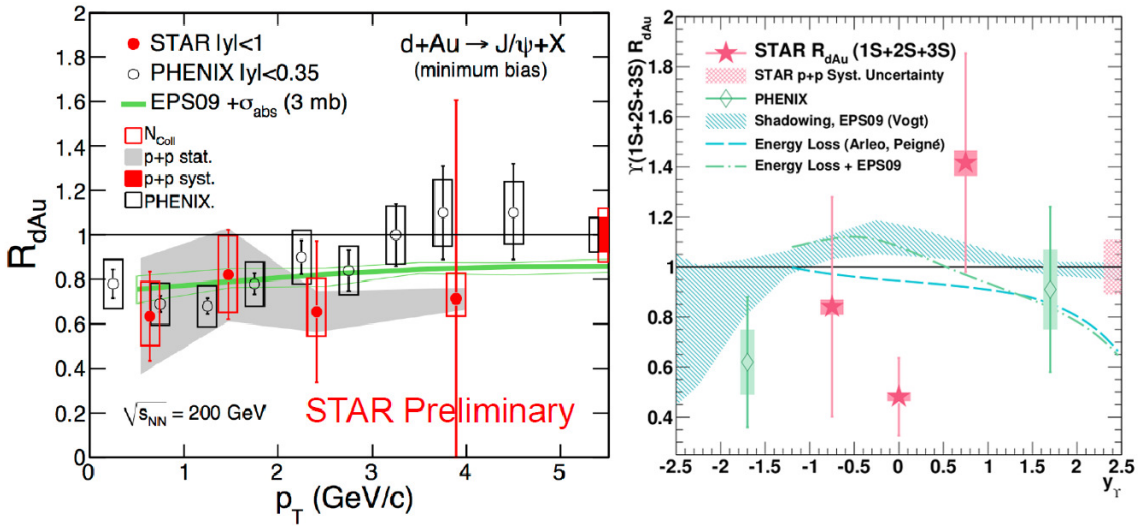

Figure 5.19: Left: J/ψ R_{dAu} as a function of p_T in d+Au collisions at $\sqrt{s_{NN}}$ = 200 GeV at STAR (closed red circles) for $|y|$ <1 and PHENIX (open white circles) for $|y| < 0.35$ and compared to EPS09 calculation nuclear for shadowing [63]. Right: R_{dAu} as a function of rapidity y for Υ(1S+2S+3S) in d+Au collisions at $\sqrt{s_{NN}}$ = 200 GeV at STAR (pink stars) and PHENIX (green diamonds) compared to models of energy loss and shadowing [90].

5.4.3 J/ψ elliptic flow

In principle, observed prompt J/ψ mesons (excluding those coming from B decays) in heavy ion collisions can have two origins − either they are produced in the initial hard scatterings − primordial J/ψ or they are produced through recombination (regeneration) from thermalized charm quarks − regenerated J/ψ.

The primordial J/ψ are heavy, strongly bound $c\bar{c}$ pairs which are not expected to gain significant v_2 in the interaction with the medium. On the other hand, regenerated J/ψ can acquire significant v_2 anisotrophy from the thermalized c and $\bar{c}$ quarks which created them.

Figure 5.20 shows the results of STAR measurements of J/ψ elliptic flow in Au+Au collisions at $\sqrt{s_{NN}}$ = 200 GeV. J/ψ elliptic flow is presented as a function of p_T for centrality 0-80% and compared with charged hadrons (dominated by pions) and ϕ mesons (upper panel) and with theoretical calculations (lower panel). To understand the interpretation of these results we need to look at the previously presented results on NPE v_2 shown in the Figure 4.6 which suggest that the charm quarks flow with the system. Therefore, the regenerated J/ψ are also expected to flow. Contrary to this, for $p_T > 2$ GeV J/ψ v_2 is consistent with zero. This result is then in disagreement with models which predict that J/ψ with $p_T > 2$ GeV are produced by recombination of thermalized $c\bar{c}$ pairs [91].

In comparison with results from the STAR experiment, Figure 5.21 shows J/ψ elliptic flow measured in Pb+Pb collisions from the ALICE experiment. As already discussed in previous section, effect of recombination at LHC is much more significant than at RHIC, therefore, it could lead to increase of J/ψ v_2. Measured v_2 is shown as a function of p_T at centrality 20-60%

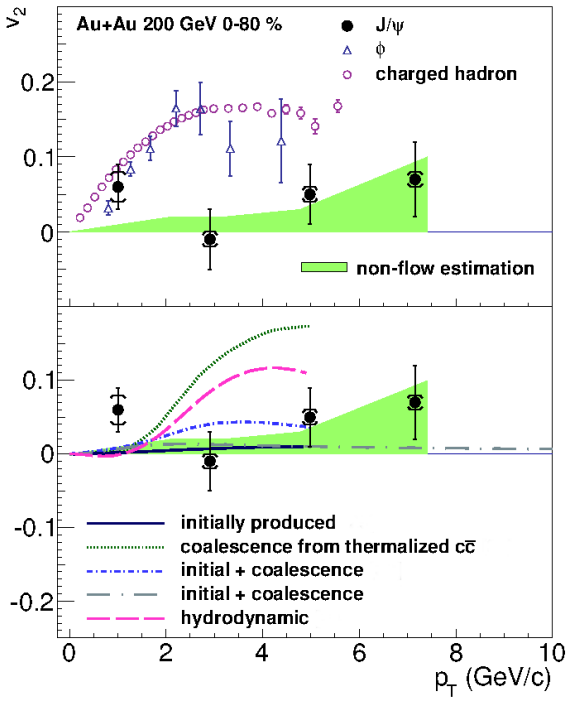

Figure 5.20: J/ψ v_2 as a function of p_T in 0-80% central events in Au+Au collisions at $\sqrt{s_{NN}}$ = 200 GeV compared to charged hadrons and ϕ mesons (upper panel) and theoretical models (lower panel) [91].

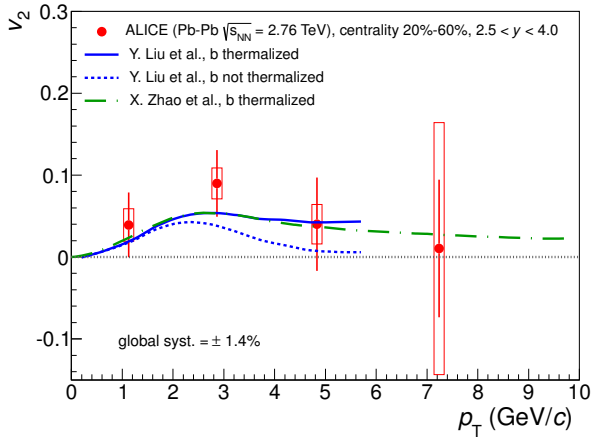

Figure 5.21: J/ψ v_2 as a function of p_T in 20-60% central events in Pb+Pb collisions at $\sqrt{s_{NN}}$ = 2.76 TeV compared to theoretical models [92].

and rapidity 2.5< y <4 and compared to theoretical calculations. A non-zero J/ψ v_2 is indeed observed in the intermediate p_T range which is in agreement with prediction that a significant fraction of observed at J/ψ LHC are produced in the QGP phase through the recombination [92].

5.4.4 Υ suppression

In the study of quark-gluon plasma, measurements of bottomonia (Υ) suppression in heavy ion collisions at RHIC and LHC have several advantages compared to charmonia (J/ψ) measurements. First, due to much smaller production cross section of $b\bar{b}$ than $c\bar{c}$ [56, 93, 94], Υ production is less affected by the statistical recombination, even at LHC energies. Secondly, charmonia can be suppressed due to hadronic co-mover interactions. On the other hand, in case of bottomonia the cross section for inelastic hadronic collisions is small and bottomonia suppression originating from such collisions is expected to be minimal [95]. Hence, the cold nuclear matter effects for Υ are expected to be smaller than for J/ψ.

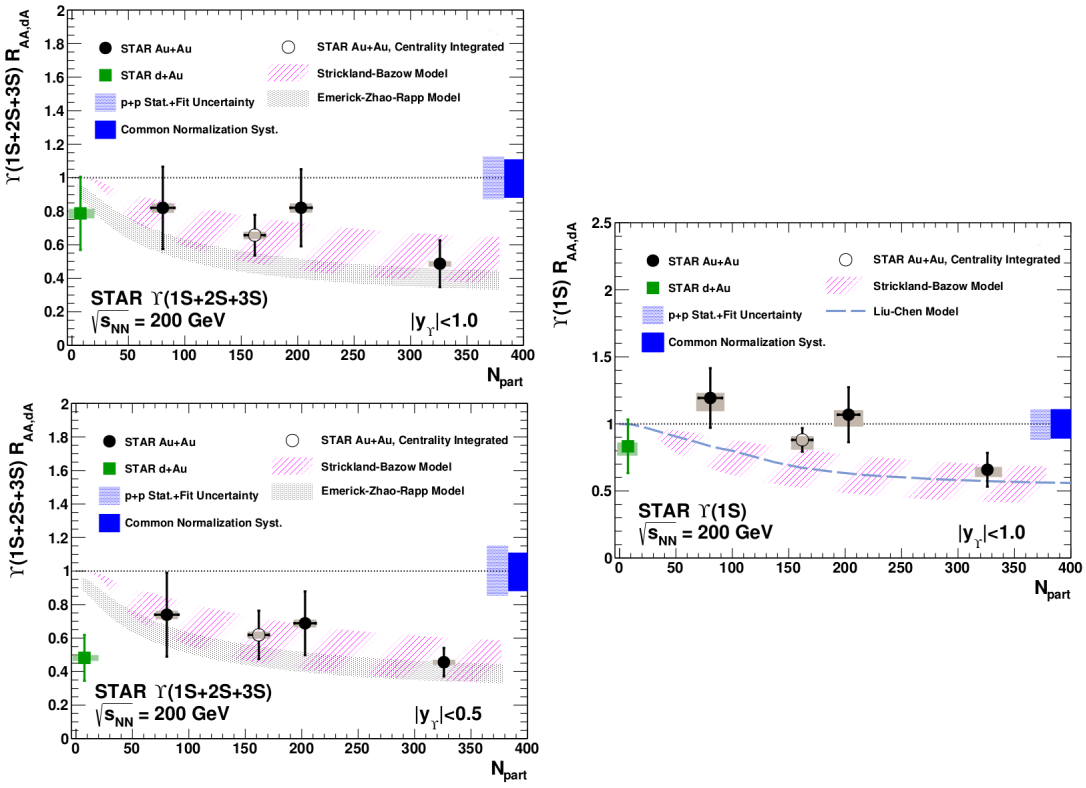

Figure 5.22: Left: R_{AA} (R_{dA}) as a function of N_{part} for Υ(1S+2S+3S) at $|y| < 1$ (up) and $|y| < 0.5$ (down),compared to models [90]. Right: R_{AA} (R_{dA}) as a function of N_{part} for Υ(1S) at $|y| < 1$, compared to models [90].

Υ(1S+2S+3S) suppression was measured in d+Au and Au+Au collisions at $\sqrt{s_{NN}}$ = 200 GeV at STAR [90]. Figure 5.22 shows nucelar modification factor R_{AA} (R_{dAu}) as a function of number of participants N_{part} for Υ(1S+2S+3S) at $|y| < 1$ and $|y| < 0.5$ and for Υ(1S) at $|y| < 1$. In general, data confirm that bottomonia Υ (1S+2S+3S) are suppressed in Au+Au collisions. Centrality dependence of results is consistent with models based on lattice QCD calculations. Therefore, suppression seen in Au+Au collisions could demonstrate the presence of quark-gluon plasma in heavy ion collisions.

In case of the most strongly bound state Υ(1S), see right panel of Figure 5.22, R_{AA} is consistent with 1 except for the most central collisions. In this region, the observed suppression could be due to melting of higher states and their lower contribution to Υ(1S) state [90].

Suppression of Υ (1S+2S+3S) production was also measured in U+U collisions at $\sqrt{s_{NN}}$ = 193 GeV. Figure 5.23 shows R_{AA} for Υ(1S+2S+3S) as a function of N_{part} for centrality ranges 0-10%,10-30% and 0-60% and compared to data presented above from Au+Au collisions and models. The U+U data show similar trend as Au+Au data accompanied by significant suppression at central collisions.

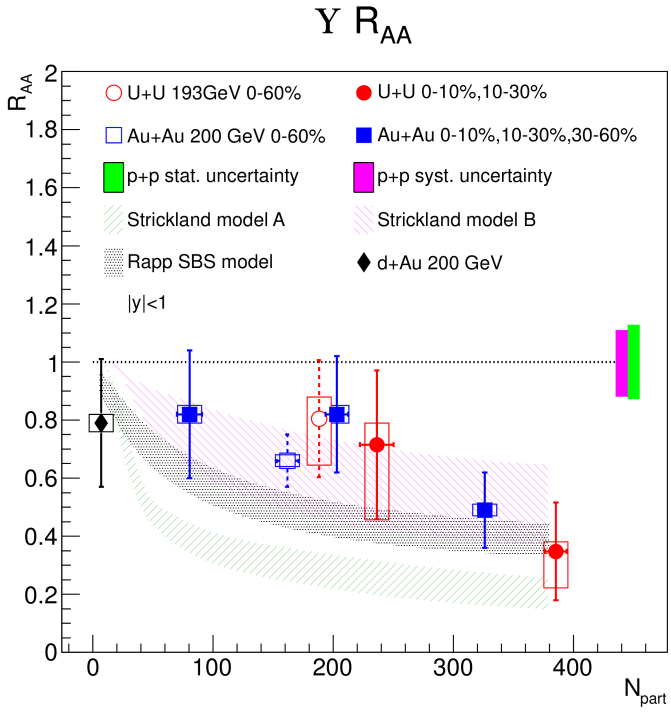

Figure 5.23: R_{AA} for Υ(1S+2S+3S) in U+U collisions at $\sqrt{s_{NN}}$ = 193 GeV as a function of N_{part} for centrality ranges 0-10%, 10-30% and 0-60%, compared with data from Au+Au collisions and models [87].

At the CMS experiment, all three Υ states can be separated and measurements of centrality dependence of their yields can be provided. Figure 5.24 shows results on R_{AA} for Υ(1S) and Υ(2S) in Pb+Pb collisions at $\sqrt{s_{NN}}$ = 2.76 TeV by the CMS experiment at the LHC. Both Υ

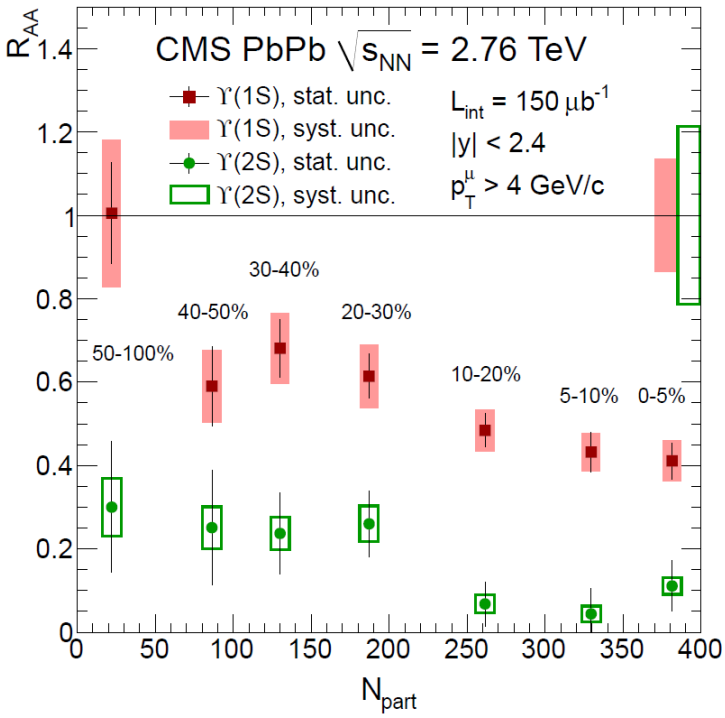

Figure 5.24: R_{AA} for Υ(1S) and Υ(2S) in Pb+Pb collisions at $\sqrt{s_{NN}} = 2.76$ TeV as a function of N_{part} [96].

states are significantly suppressed, Υ(1S) by factor of 2, Υ(2S) by factor of 8. The suppression increases towards central collisions. Measurements were performed also for Υ(3S) state (not illustrated in the Figure 5.24) which is most suppressed by factor larger than 10. These results support the hypothesis of increased sequential suppression of less strongly bound states – higher states are almost fully dissociated and regeneration component is small [96].

5.4.5 Quarkonia suppression as a function of binding energy

Sequential suppression of different quarkonium states is not only the evidence of deconfined phase of matter produced in heavy ion collisions. Moreover, it gives the information about the temperature of the matter produced in collisions, since, as has been already mentioned, different quarkonium states melt at different temperatures.

Figure 5.25 gives comparison of suppression of different quarkonium states, i.e. R_{AA} as a function of binding energy. Right panel of the figure shows STAR data and left panel CMS data. In general, quarkonia are suppressed at both experiments, furthermore, higher excited states are suppressed more than ground states and bottomonia are less suppressed than charmonia. These results are in agreement with prediction by Debye screening, since higher excited states and also charmonia compared to bottomonia have smaller binding energy and therefore, there is higher probability for them to dissociate in QGP.

The shown STAR results are by far not definitive. Further more precise analysis of measurements of sequential suppression of different quarkonium states will be performed using the MTD detector thanks to which different Υ states will be distinguishable.

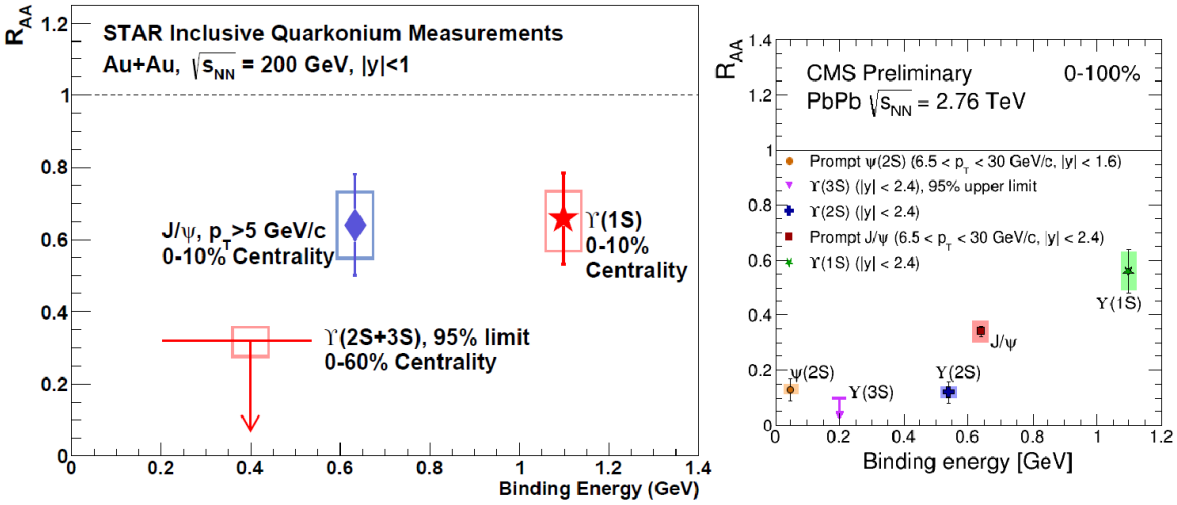

Figure 5.25: R_{AA} for for different quarkonium states as a function of binding energy at $\sqrt{s_{NN}} = 200$ GeV in Au+Au collisions at STAR (right panel) [90] and at $\sqrt{s_{NN}} = 2.76$ TeV in Pb+Pb collisions at CMS (left panel) [97].

Summary

This thesis serves as an introduction to heavy ion physics and newly discovered state of partonic matter called quark-gluon plasma (QGP). Normally, quarks and gluons, the basic building blocks of matter, are bound within hadrons. However, the theory of strong interaction, Quantum Chromodynamics (QCD), predicts that under conditions of high energy density and high temperature the nuclear matter may undergo a phase transition into quark-gluon plasma phase. It is expected that quark-gluon plasma was present in the first moments of the evolution of the universe. We think that it is possible to recreate this state of matter also in the laboratory by colliding high energy heavy ion nuclei.

In this thesis QCD and its two main characteristic − color confinement and asymptotic freedom are briefly presented as a theoretical background of QGP formation.

Also, basic kinematic and dynamic variables, geometry and space-time evolution of the nucleus-nucleus collisions are described. Since quark-gluon plasma, as possible phase of the heavy ion collision, exists only for a short time it cannot be studied directly. Several observables and probes, which could confirm the presence of quark-gluon plasma are presented.

To study the quark-gluon plasma, an experiment which could explore the medium created in heavy ion collisions is needed. A foremost experiment designed to investigate the behavior of strongly interacting matter is the STAR experiment at RHIC in Brookhaven National Laboratory. In this thesis, different subdetectors of this experiment are described in more detail. The emphasis is placed on the Muon Telescope Detector (MTD) which is newly installed subsystem at STAR experiment and is expected to significantly enhance the STAR's capabilities in study of heavy quarks in a near future.

It is the physics of heavy quarks (c and b) and namely quarkonia to which the main part of this thesis is dedicated. Due to their large mass heavy quarks are exclusively produced in early stages of the collisions. In this thesis it is explained how they due to their large masses are expected to interact differently with the surrounding medium and how they can be used as unique probes of the quark-gluon plasma phase. Basic information about heavy quark energy loss, production cross section and several recent open heavy flavor measurements are discussed.

One of the most prominent subtopics in the heavy flavor physics is the production and modification of production of quarkonia − bound states of quarks and antiquarks. Heavy quarkonia are important probe of the matter created in heavy ion collisions. The suppression of their production in heavy ion collisions has been considered as a signature of the QGP. The thesis gives an overview of the most important topics in this field. It describes models of heavy quarkonia production and also discusses different effects, not only "QGP effects" but also "cold nuclear matter effects", which modify the quarkonia production. The last part of this thesis gives an overview of measurements of the STAR experiment on the heavy quarkonia production

and compares them with selected results from experiments at colliders SPS and LHC. In general, given results show that quarkonia are suppressed in heavy ion collisions. Nevertheless, the interplay of various nuclear matter effects can end in striking results. Therefore, correct interpretation and further experimental measurements are needed.

As shown in the thesis, the STAR experiment is rich on heavy quark physics measurements. Thanks to newly installed MTD more precise data and more good results are expected to be obtained very soon.

Bibliography

[1] Wikipedia. The Standard Model of Elementary Particles. `http://en.wikipedia.org/wikiFile:Standard_Model_of_Elementary_Particles.svg`. [online 15.03.2014].

[2] Georges Aad et al. Observation of a new particle in the search for the Standard Model Higgs boson with the ATLAS detector at the LHC. *Phys.Lett.*, B716:1–29, 2012.

[3] Evidence for the spin-0 nature of the Higgs boson using ATLAS data. *Physics Letters B*, 726(1-3):120–144, 2013.

[4] Measurements of Higgs boson production and couplings in diboson final states with the ATLAS detector at the LHC . *Physics Letters B*, 726(1-3):88 – 119, 2013.

[5] E. Eichten, K. Gottfried, T. Kinoshita, K.D. Lane, and Tung-Mow Yan. Charmonium: The Model. *Phys.Rev.*, D17:3090, 1978.

[6] Robert Craig Group. *Measurement of the inclusive jet cross section using the midpoint algorithm in run 11 at the collider detector at Fermilab (CDF)*. PhD thesis, University of Florida, 2006.

[7] Siegfried Bethke. The 2009 World Average of alpha(s). *Eur.Phys.J.*, C64:689–703.

[8] J. Bartke. *Introduction to Relativistic Heavy Ion Physics*. World Scientific, Singapore, 1st edition, 2009.

[9] David J. Gross and Frank Wilczek. Ultraviolet Behavior of Non-Abelian Gauge Theories. *Phys. Rev. Lett.*, 30:1343–1346, Jun 1973.

[10] J. C. Collins and M. J. Perry. Superdense Matter: Neutrons or Asymptotically Free Quarks ? *Phys. Rev. Lett.*, 34:1353–1356, May 1975.

[11] BNL. Schematic QCD Phase Diagram. `http://www.bnl.gov/newsroom/news.php?a=21870`. [online 15.04.2014].

[12] Michal Sumbera. Results from STAR Beam Energy Scan Program. *Acta Phys.Polon.Supp.*, 6:429–436, 2013.

[13] Cheuk-Yin Wong. *Introduction to High-Energy Heavy Ion collisions*. Utopia Press, Singapore, 1st edition, 1994.

[14] H. Satz S. Sarkar and B. Sinha. *The Physics of the Quark-Gluon Plasma A: Introductory Lectures*. Springer, Berlin Heidelberg, 1st edition, 2010.

[15] Ramona Vogt. *Ultrarelativistic Heavy-Ion Collisions*. Elsevier, Amsterdam, 1st edition, 2007.

[16] Mercedes Lopez Noriega. *Pion Interferometry in AuAu Collisions at a Center of Mass Energy per Nucleon of 200 GeV*. PhD thesis, The Ohio State University, 2004.

[17] Jean-Yves Ollitrault. Anisotropy as a signature of transverse collective flow. *Phys. Rev. D*, 46:229–245, Jul 1992.

[18] Open Science Grid. Probing the Perfect Liquid with the STAR Grid. `http://www.interactions.org/sgtw/2006/1025/star_grid_more.html`. [online 30.06.2014].

[19] Charles Costello. RHIC. `http://www.charlescostello.net/#!RHIC/zoom/mainPage/image1of`. [online 20.03.2014].

[20] Wolfram Fischer. Run overview ofthe Relativistic Heavy Ion Collider. `http://www.rhichome.bnl.gov/RHIC/Runs/`. [online 13.07.2014].

[21] Brookhaven National Laboratory. RHIC Accelerators. `http://www.bnl.gov/rhic/complex.asp`. [online 20.03.2014].

[22] The PHENIX Experiment. An Introduction to PHENIX. `https://www.phenix.bnl.gov/phenix/WWW/intro/detectors/index.html`. [online 31.03.2014].

[23] Department of Physics Lund University. The PHENIX Experiment. `http://www.hep.lu.se/phenix/`. [online 31.03.2014].

[24] Maria and Alex Schmah. The Solenoidal Tracker At RHIC (STAR). `http://indico.cern.ch/event/30248/session/49/contribution/253/material/slides/0.pdf`. [online 20.03.2014].

[25] M. Anderson, J. Berkovitz, W. Betts, R. Bossingham, F. Bieser, et al. The Star time projection chamber: A Unique tool for studying high multiplicity events at RHIC. *Nucl.Instrum.Meth.*, A499:659–678, 2003.

[26] G.D. Alkhazov, A.P. Komar, and A.A. Vorobev. Ionization fluctuations and resolution of ionization chambers and semiconductor detectors. *Nuclear Instruments and Methods*, 48(1):1–12, 1967.

[27] Masayuki Wada. *Resonance Particles in Heavy-Ion Collisions*. PhD thesis, The University of Texas at Austin, 2013.

[28] H. Bichsel, D.E. Groom, and S.R. Klein. Passage of particles through matter. `http://pdg.lbl.gov/2006/reviews/passagerpp.pdf`. [online 05.04.2014].

[29] Christopher Beresford Powell. *J/ψ Production in Heavy Ion Collisions at the STAR Detector at RHIC*. PhD thesis, University of Cape Town, 2012.

[30] Jian Wu, B. Bonner, H.F. Chen, X. Dong, G. Eppley, F. Geurts, S.L. Huang, C. Li, W.J. Llope, T. Nussbaum, E. Platner, J. Roberts, L.J. Ruan, M. Shao, X.L. Wang, Z. Xu, and Z.Z. Xu. The performance of the TOFr tray in STAR. *Nuclear Instruments and Methods in Physics Research Section A: Accelerators, Spectrometers, Detectors and Associated Equipment*, 538(1-3):243–248, 2005.

[31] Kohei Kajimoto. *A Large Area Time of Flight Detector for the STAR Experiment at RHIC*. PhD thesis, The University of Texas in Austin, 2009.

[32] F. Jin. Measurement of Non-photonic Electrons in p+p Collisions at $\sqrt{s_{NN}}$ = 200GeV with reduced detector material in STAR. *J.Phys.*, G36:064051, 2009.

[33] M. Shao, O. Barannikova, X. Dong, Y. Fisyak, L. Ruan, et al. Extensive particle identification with TPC and TOF at the STAR experiment. *Nucl.Instrum.Meth.*, A558:419–429, 2006.

[34] T.M. Cormier, A.I. Pavlinov, M.V. Rykov, V.L. Rykov, and K.E. Shestermanov. STAR barrel electromagnetic calorimeter absolute calibration using 'minimum ionizing particles' from collisions at RHIC. *Nucl.Instrum.Meth.*, A483:734–746, 2002.

[35] Rosi J. Reed. Υ *production at* $\sqrt{s_{NN}}$ *=200 GeV in p+p and Au+Au collisions at STAR.* PhD thesis, University of California, Davis, 2011.

[36] K. Schweda. A Heavy-flavor tracker for STAR. *Nucl.Phys.*, A774:907–910, 2006.

[37] STAR Collaboration. SSD General Overview. `http://www.star.bnl.gov/public/ssd/STAR_technique/ssd_general_overview_doc_6.pdf`. [online 23.06.2014].

[38] L. Ruan, G. Lin, Z. Xu, K. Asselta, H.F. Chen, et al. Perspectives of a Midrapidity Dimuon Program at RHIC: A Novel and Compact Muon Telescope Detector. *J.Phys.*, G36:095001, 2009.

[39] Lijuan Ruan. Status of the Muon Telescope Detector. STAR Collaboration Meeting at FIAS.

[40] H. Chen, I. Wang, Gonzalez-Diaz D., J. Wang, X. Fan, J. Cheng, and Y. Li. Production of long-strip multi-gap resistive plate chamber module for the STAR-MTD system. *Jour. of Instr.*, 7 P10006, 2012.

[41] C. Yang, X.J. Huang, C.M. Du, B.C. Huang, Z. Ahammed, et al. Calibration and performance of the STAR Muon Telescope Detector using cosmic rays. 2014.

[42] E Cerron Zeballos, I Crotty, D Hatzifotiadou, J Lamas Valverde, S Neupane, M.C.S Williams, and A Zichichi. A new type of resistive plate chamber: The multigap RPC. *Nuclear Instruments and Methods in Physics Research Section A: Accelerators, Spectrometers, Detectors and Associated Equipment*, 374(1):132 – 135, 1996.

[43] Barbara Trzeciak. Heavy flavor production in the STAR experiment, 2014.

[44] W.J. Llope, J. Zhou, T. Nussbaum, G.W. Hoffmann, K. Asselta, et al. The STAR Vertex Position Detector. 2014.

[45] Les Bland. STAR Beam-Beam Counter Schematic. `http://www.star.bnl.gov/public/trg/`. [online 30.06.2014].

[46] F.S. Bieser, H.J. Crawford, J. Engelage, G. Eppley, L.C. Greiner, E.G. Judd, S.R. Klein, F. Meissner, R. Minor, Z. Milosevich, G. Mutchler, J.M. Nelson, J. Schambach, A.S. VanderMolen, H. Ward, and P. Yepes. The STAR trigger. *Nuclear Instruments and Methods in Physics Research Section A: Accelerators, Spectrometers, Detectors and Associated Equipment*, 499(2-3):766 – 777, 2003. The Relativistic Heavy Ion Collider Project: RHIC and its Detectors.

[47] A.A. Isayev. Heavy Flavor Probes of Quark-Gluon Plasma. 2009.

[48] Anthony D. Frawley, T. Ullrich, and R. Vogt. Heavy flavor in heavy-ion collisions at RHIC and RHIC II. *Phys.Rept.*, 462:125–175, 2008.

[49] Eric Braaten and Markus H. Thoma. Energy loss of a heavy fermion in a hot plasma. *Phys.Rev.*, D44:1298–1310, 1991.

[50] Munshi Golam Mustafa, Dipali Pal, Dinesh Kumar Srivastava, and Markus Thoma. Radiative energy loss of heavy quarks in a quark gluon plasma. *Phys.Lett.*, B428:234–240, 1998.

[51] Yuri L. Dokshitzer and D.E. Kharzeev. Heavy quark colorimetry of QCD matter. *Phys.Lett.*, B519:199–206, 2001.

[52] Nestor Armesto, Carlos A. Salgado, and Urs Achim Wiedemann. Medium induced gluon radiation off massive quarks fills the dead cone. *Phys.Rev.*, D69:114003, 2004.

[53] Raktim Abir, Carsten Greiner, Mauricio Martinez, Munshi G. Mustafa, and Jan Uphoff. Soft gluon emission off a heavy quark revisited. *Phys.Rev.*, D85:054012, 2012.

[54] Michelangelo L. Mangano. Two lectures on heavy quark production in hadronic collisions. 1997.

[55] P.P. Bhaduri, P. Hegde, H. Satz, and P. Tribedy. An introduction to the spectral analysis of the qgp. In Sourav Sarkar, Helmut Satz, and Bikash Sinha, editors, *The Physics of the Quark-Gluon Plasma*, volume 785 of *Lecture Notes in Physics*, pages 179–197. Springer Berlin Heidelberg, 2010.

[56] R. Vogt. The Total charm cross-section. *Eur.Phys.J.ST*, 155:213–222, 2008.

[57] Min Jung Kweon. Recent Results on Open Heavy Flavour Observables in Relativistic Nuclear Collisions. Quark Matter 2014.

[58] Betty Bezverkhny Abelev et al. Beauty production in p+p collisions at $\sqrt{s} = 2.76$ TeV measured via semi-electronic decays. 2014.

[59] Zhenyu Ye. Open Charm Hadron Production in p+p, Au+Au and U+U Collisions at STAR. Quark Matter 2014.

[60] Olga Rusňáková. The measurement of non-photonic electrons in STAR. 2013.

[61] L. Adamczyk et al. Elliptic flow of non-photonic electrons in Au+Au collisions at $\sqrt{s_{\rm NN}}$ = 200, 62.4 and 39 GeV. 2014.

[62] N. Brambilla, S. Eidelman, B.K. Heltsley, R. Vogt, G.T. Bodwin, et al. Heavy quarkonium: progress, puzzles, and opportunities. *Eur.Phys.J.*, C71:1534, 2011.

[63] Christopher Beresford Powell. Quarkonia production at the STAR detector. *J.Phys.Conf.Ser.*, 455:012038, 2013.

[64] Eric Braaten, Sean Fleming, and Tzu Chiang Yuan. Production of heavy quarkonium in high-energy colliders. *Ann.Rev.Nucl.Part.Sci.*, 46:197–235, 1996.

[65] Mathias Butenschoen and Bernd A. Kniehl. J/ψ production in NRQCD: A global analysis of yield and polarization. *Nucl.Phys.Proc.Suppl.*, 222-224:151–161, 2012.

[66] Z. Conesa del Valle, G. Corcella, F. Fleuret, E.G. Ferreiro, V. Kartvelishvili, et al. Quarkonium production in high energy proton-proton and proton-nucleus collisions. *Nucl.Phys.Proc.Suppl.*, 214:3–36, 2011.

[67] L. Adamczyk et al. J/ψ polarization in p+p collisions at $\sqrt{s}$ = 200 GeV in STAR. 2013.

[68] T. Matsui and H. Satz. J/ψ Suppression by Quark-Gluon Plasma Formation. *Phys.Lett.*, B178:416, 1986.

[69] Louis Kluberg and Helmut Satz. Color Deconfinement and Charmonium Production in Nuclear Collisions. 2009.

[70] A. Adare et al. Measurement of Υ(1S+2S+3S) production in p+p and Au+Au collisions at $\sqrt{s_{NN}}$ = 200 GeV. 2014.

[71] Taku Gunji. *J/ψ Production in High Energy Heavy Ion Collisions at RHIC*. PhD thesis, University of Tokyo, 2007.

[72] Xingbo Zhao and Ralf Rapp. Charmonium in medium: From correlators to experiment. *Phys. Rev. C*, 82:064905, Dec 2010.

[73] Yunpeng Liu, Zhen Qu, Nu Xu, and Pengfei Zhuang. transverse momentum distribution in high energy nuclear collisions. *Physics Letters B*, 678(1):72 – 76, 2009.

[74] K.J. Eskola, V.J. Kolhinen, and C.A. Salgado. The scale dependent nuclear effects in parton distributions for practical applications. *The European Physical Journal C - Particles and Fields*, 9(1):61–68, 1999.

[75] BNL Wiki. Nuclear modification of the parton distribution functions. https://wiki.bnl.gov/qpg/index.php/File:Gluon-RPb-scale24.png.

[76] J. W. Cronin, H. J. Frisch, M. J. Shochet, J. P. Boymond, P. A. Piroué, and R. L. Sumner. Production of hadrons at large transverse momentum at 200, 300, and 400 GeV. *Phys. Rev. D*, 11:3105–3123, Jun 1975.

[77] A. Krzywicki, J. Engels, B. Petersson, and U. Sukhatme. Does a nucleus act like a gluon filter? *Physics Letters B*, 85(4):407 – 412, 1979.

[78] Jean Paul Blaizot, Francois Gelis, and Raju Venugopalan. High-energy pA collisions in the color glass condensate approach. 1. Gluon production and the Cronin effect. *Nucl.Phys.*, A743:13–56, 2004.

[79] M.J. Leitch. Quarkonia production at RHIC. *J.Phys.*, G32:S391–S400, 2006.

[80] N. Armesto and A. Capella. A Quantitative reanalysis of J/ψ suppression in nuclear collisions. *Phys.Lett.*, B430:23–31, 1998.

[81] Xingbo Zhao and Ralf Rapp. Charmonium in medium: From correlators to experiment. *Phys. Rev. C*, 82:064905, Dec 2010.

[82] Xingbo Zhao and Ralf Rapp. Transverse momentum spectra of in heavy-ion collisions. *Physics Letters B*, 664(4-5):253 – 257, 2008.

[83] S. Digal, P. Petreczky, and H. Satz. Quarkonium feed down and sequential suppression. *Phys.Rev.*, D64:094015, 2001.

[84] L. Adamczyk et al. J/ψ production at low p_T in Au+Au and Cu+Cu collisions at $\sqrt{s_{NN}}$ = 200 GeV at STAR. 2013.

[85] Anthony Kesich. STAR Quarkonium Program and Future in p+A Studies. RHIC/AGS Annual Users Meeting, June 2014.

[86] L. Adamczyk et al. J/ψ production at high transverse momenta in p+p and Au+Au collisions at $\sqrt{s_{NN}}$ = 200 GeV. *Phys.Lett.*, B722:55–62, 2013.

[87] Wangmei Zha. Quarkonium production in p+p and A+A from STAR. Quark Matter 2014.

[88] A. Andronic. Experimental results and phenomenology of quarkonium production in relativistic nuclear collisions. Quark Matter 2014.

[89] A. Andronic, P. Braun-Munzinger, K. Redlich, and J. Stachel. Evidence for charmonium generation at the phase boundary in ultra-relativistic nuclear collisions. *Phys.Lett.*, B652:259–261, 2007.

[90] L. Adamczyk et al. Suppression of Upsilon Production in d+Au and Au+Au Collisions at $\sqrt{s_{NN}}$ = 200 GeV. *Phys.Lett.*, B735:127, 2014.

[91] L. Adamczyk et al. Measurement of J/ψ Azimuthal Anisotropy in Au+Au Collisions at $\sqrt{s_{NN}}$ = 200 GeV. *Phys.Rev.Lett.*, 111(5):052301, 2013.

[92] Ehab Abbas et al. J/ψ Elliptic Flow in $Pb-Pb$ Collisions at $\sqrt{s_{NN}}$ = 2.76 TeV. *Phys.Rev.Lett.*, 111:162301, 2013.

[93] B.I. Abelev et al. Υ cross section in $p+p$ collisions at $\sqrt{s}$ = 200 GeV. *Phys.Rev.*, D82:012004, 2010.

[94] A. Adare et al. J/ψ production versus transverse momentum and rapidity in p+p collisions at $\sqrt{s}$ = 200 GeV. *Phys.Rev.Lett.*, 98:232002, 2007.

[95] Zi-wei Lin and C.M. Ko. Upsilon absorption in hadronic matter. *Phys.Lett.*, B503:104–112, 2001.

[96] S. Chatrchyan, V. Khachatryan, A. M. Sirunyan, A. Tumasyan, W. Adam, E. Aguilo, T. Bergauer, and Dragicevic et al. Observation of Sequential Υ Suppression in PbPb Collisions. *Phys. Rev. Lett.*, 109:222301, 2012.

[97] Dong Ho Moon. Charmonia in p+p and Pb+Pb with CMS. Quark Matter 2014.